ICFO - Institut de Ciències Fotòniques
&
UPC - Universitat Politècnica de Catalunya

Plasmon-electron interactions in low dimensional materials

DOCTORAL THESIS
in partial fulfillment of the requirements
for the degree of Doctor of Philosophy
by

Sandra de Vega

Supervisor: Prof. F. Javier García de Abajo

Castelldefels, February 2020

This doctoral dissertation has been carried out in the Nanophotonics Theory Group at ICFO - The Institute of Photonic Sciences in Castelldefels, Barcelona, thanks to the funding of a predoctoral grant from the FPU programme of the Spanish Ministry of Education and Culture (Ref. FPU14/01769).

A la memoria de Daniel Arroyo.

A mis padres.

Acknowledgments

Quién me iba a haber dicho a mí, aquel julio de 2014, que me iba a embarcar en una aventura como ésta, que tanto me ha hecho aprender y crecer como persona. Cierto es que en todo camino hay altibajos, pero creedme cuando digo que ha sido una experiencia estupenda, y que si ha sido así es gracias a todas esas personas que, de una manera u otra, me han influenciado en el transcurso de estos años. Así que prometo no ser breve con los agradecimientos.

En primer lugar, querría dar las gracias a Javier, por ser quién me dio la oportunidad. Si hay algo con lo que me gustaría quedarme de haber trabajado con él, dejando a un lado todos sus conocimientos que, os aseguro, son bastantes, es con su actitud positiva frente a los problemas y con la energía que pone en el día a día.

The days would have been much less fun without having the ex- and current NPTians around: Ana, Iván, Andrea M., José, Renwen, Lijun, Joel, Álvaro, Eduardo, Valerio, Deng, Andrea K., Hani, Shahaf, Fadil, Kamram, Vahagn, and Giorgos. Always willing to chat, to have a coffee, to go for dinner, and surely, to rock it at the conferences and other places. Eduardo and Catarina, obrigada por toda a sua gentileza! Braga ftw! Joel, thanks for adopting me in Denmark! Más en especial, me gustaría destacar primero a José, que tantos buenos consejos me ha dado, con quien me he reído hasta no poder más y que te transmite su pasión por lo que hace. Ya te lo han dicho, eres un verdadero líder, y lo sabes ;) En segundo, a Álvaro, mi compi del *lunch at 2pm*, siempre dispuesto a ayudar, escuchar y que tiene mil y un detalles. ¡Espero que haya más carreras y excursiones donde lo demos todo!

Sometimes people happen to you unexpectedly and before you realize, they have become pivotal in your life. Pamina, Kavitha, did you hear that? You girls have made feel like at home by being around. Kavitha, in your own

acknowledgements you wrote that you thank me for convincing you to do crazy things... I should thank you for saying "yes, let's go for it!" And well, for being always willing to go for a walk, for those chats full of sarcasm, jokes and sparky comments, for giving me the ticket to India (literally), for being an example of resilience and perseverance. You'll do great wherever you go! Pamina, it's amazing to have someone around that transforms every single small idea into reality, no matter if it's an excursion, a workshop, or a dinner; a person that always carries on, that keeps surprising me in so many different ways, and that likes to try new things and to meet people as much as me. I am really grateful that, once in a while, you shake me out of my comfort zone, I have probably learnt how to be a bit more communicative thanks to you. Here's to us, girls!

Por supuesto, también ha habido grandes momentos con mis compis de piso: Ugaitz y Julio. Nuestra cocina totalmente equipada, nuestra mesa de tres patas y media y las piscinas cada vez que llueve pasarán a los anales de las experiencias de alquilar piso. Gracias por crear un ambiente tan agradable y animado.

He de confesar que estos años no solo han significado *doctorado* para mí sino también *rugby*. Desde el principio, las chicas del equipo y mis entrenadores han sido la no tan pequeña familia deportiva que me acogió y con la que he disfrutado al máximo de competir, de los viajes, las giras (¡vámonooos!) y las tardes (y noches) en que las horas han pasado volando simplemente charlando. Habéis hecho que muchos de mis días en los que me consumía la frustración terminasen bien y me habéis dado perspectiva fuera del ambiente académico. Ha sido enormemente gratificante ser partícipe de toda nuestra evolución hasta estar en DHC. Gracias desde mi corazón azul y amarillo. ¡Vamos CRUC!

And talking about rugby... Sarah, thanks for being my other rugby-soulmate. Probably one of the best things of having been involved in ICONS is to meet

people like you, that cares, wants to change and improve things, and is willing to take action and dedicate time to it. I have really enjoyed those thought-provoking conversations with well founded arguments.

It has also been fantastic to get to know such open-minded people as Alican and İnci. Alican, you gave me a good lesson on how to take things easier and on how a strong will can make someone create his own path. Thanks as well for all of our own philosophical investigations! İnci, I am really glad for all the kindness you have given me, it's been real fun when you have cracked some unexpected sharp jokes.

Los inicios son importantes, y me siento afortunada de haber empezado en ICFO rodeada de unos *summer fellows* tan entusiastas, sobre todo: Marcos, Auxi, María, Irene, Nico y Patricia. Marcos, un ejemplo de madurez, jovialidad y valentía diciendo "hasta aquí he llegado". Auxi, la primerísima persona que conocí del ICFO, gracias por todas las risas en alguna que otra comida. María, tu eficiencia y competencia no pasan desapercibidas. Es genial tener de vez en cuando una conversación crítica y contar con alguien que sabes que si te dice "sí" lo mantiene y ayuda hasta el final. Irene, mi compi de prácticas, gracias por todo lo que te has involucrado con los estudiantes, por todo el tiempo que le has dedicado y por las charlas entre medias, qué grato es trabajar así. Patricia, nos hemos recorrido media Europa, media Galicia y medio País Vasco, ¿para cuándo la próxima? Gracias por haber mantenido el contacto todo este tiempo y por, cuando nos reunimos de nuevo, pareciera que nos hubiésemos visto el día anterior. ¡No pierdas el espíritu de aprender y querer hacer cosas nuevas!

It has been great to share work place, dinners or other activities with many nice people related to ICFO, in one way or another: Catarina, Ana P., Roland, Lüc, Susmita, Iker, Hugo, Raúl, Gerard, Jana, Max, Carlotta, Eric, Alba, Anil, Lara, Juan Miguel, Rubaiya, Pau, Bárbara, Pili, Blanca, Rafaël, David A., David P., Vikas, Anuja, Rinu, Vindhiya, Sukeert, Samyo, Christian, Natalia, Mariona,

Ester and many others. Thanks to Lisa for all the hikes, trip ideas and good vibes. It's nice to count on cheerful people that know every single song! And also to Antoine, for all those BTT rides, nice concerts and interesting chats. Ready for Caravan 3.0!

También agradecer a David Artigas todo el apoyo con las prácticas y la burocracia de la beca, y a todas las personas que están o han estado en administración, eventos (Ester, Elena y Jordi), comunicación (Alina, Tomas, Albert, Brook), KTT (Fede, Silvia) y RRHH (Manuela, Anne, Mireia, Ingrid, Mery) que hacen posible la buena dinámica del instituto y que están dispuestos a echar una mano en lo que necesitemos. M'agradaria més, enviar-li un abraçada a Mercè, a qui era tan grat saludar i qui amb tanta complicitat ens va dibuixar un cerdicornio meravellós.

Paula EFe ;) gracias por ser tan afable y sociable. Eres una de esas personas que rápido te hace sentir incluida. Agradecer también a toda la familia de Bravas. Ha sido estupendo conocer el Ultimate y sentirse tan bien acogida desde el minuto uno. Thanks as well to all the Eindhoven people that made my internship such a positive experience. Specially to Jaime, Alberto, their respective group members and Subash.

No podría terminar estos agradecimientos sin mencionar a mi familia. Empezando por mi abuela Paca, que tiene más vitalidad que yo y un carácter fuerte con el que ha superado tantas adversidades, y por mis abuelos, Eugenio y Mariana, que tantas historias me han contado de otra época y otras costumbres. Puedo decir orgullosa que los tres habéis venido a visitarme, espero haberos tratado con la hospitalidad que os merecéis.

La verdad sea dicha, somos ciento y la madre... Y ha sido muy divertido. Me alegra saber que estáis ahí, que me llamáis y escribís, que tengo la suerte de tener multitud de anécdotas con vosotros ya sea en Madrid o en el pueblo. Gracias a mis tíos David y Agustín, a mis tías Ana y Paloma, a mis primos David, Eva y Ana, y también a Salvi, Carmen, Cristina y Álvaro.

Laura, que me has acompañado literalmente a la otra punta del mundo, que tenemos no sé cuántas batallitas juntas: sabes que cuento contigo. Es increíble lo mucho que has luchado para conseguir lo que te proponías. Sigue adelante, que todo llega.

Mamá, Papá, sabéis que sin vosotros todo esto no habría sido posible, gracias por todo el apoyo incondicional durante todos estos años, por confiar y por cuidar de mí aun en la distancia. Espero no haberos dado demasiados quebraderos de cabeza. Soy muy afortunada de teneros.

Ya por último, lo prometido es deuda. Dani esta tesis te va dedicada a ti, que durante tanto tiempo fuiste mi referente a seguir. Me enseñaste que siempre hay algo que aprender y por lo que ilusionarse, que los errores no se lamentan se intentan arreglar, que si me caigo me levanto, que hay que dar nuestro cien por cien en lo que hagamos. Sé que todo esto te habría encantado.

Abstract

Ever since the advent of modern technology, major developments have come hand in hand in Electronics, Photonics, and other areas of Physics and Engineering with miniaturization and speed of operation. A proof of this is provided by the impressive success of Moore's law,[1] which predicted that the number of transistors per affordable microprocessor would double every two years, that would not have been possible if transistors kept their initial physical dimensions. By the end of 2018, MIT and University of Colorado researchers broke a new record for the smallest 3D transistor yet[2] with a lateral size of only 2.5 nm. As of 2019, there are commercially available 5 nm transistors[3,4] which are planned to be shrunk to 3 nm by 2021. Considering these dimensions, it is then remarkably important to understand and to be able to manipulate materials at the nanoscale, where they behave in very different ways compared to macroscopic structures.

Given this context, researchers have put substantial efforts towards finding the explanation of diverse phenomena at the nanoscale, engineering new nanodevices, and proposing or predicting new mechanisms to achieve the next generation of chips and integrated circuits. As a matter of fact, the rise of the so-called low dimensional materials (graphene, transition metal dichalcogenides, cuprates, hBN, black P, carbon nanotubes, and others), *i.e.*, those whose atomic planes are bonded by weak van der Waals forces (2D) or whose atoms are arranged in chains or tubes (1D), has been influenced by the quest for new more efficient and compact designs. In this thesis we study the optical properties of some of these materials and how they are modified by the interaction with electrons that, depending on the specific case, we consider to be either dopants (added into the material), or impinging in highly-focused beams, or via tunneling from nearby conductors.

Specifically, we start with a comprehensive analysis of plasmons, the col-

lective oscillations of free electrons coupled to light, in finite highly-doped carbon nanotubes. Next, we explore how to select the proper plasmon mode excited by electron beams depending on the orientation and position of the latter and also how to improve the interaction between two quantum emitters when mediated by the main plasmonic mode in our structures. We predict record-high Purcell factors of the order of 10^8, which supports the use of carbon nanotubes as active plasmonic elements with high potential in optoelectronics and quantum optics applications.

We then continue with one dimensional systems, but now focusing on atomic chains to emulate simple solid-like structures where to inspect strong-field driven electron dynamics in solids. More specially, we tackle several still pending questions about the role of electron-electron interactions and the proper choice of material to achieve better high-harmonic generation yields. After that, we test these findings in more realistic 1D systems: carbon nanotubes. Eventually, we find that the addition of a small number of doping charges to semiconducting systems can enable intraband plasmon excitations that concentrate the impinging light and boosts the high-harmonic generation efficiency.

Next, we move to an investigation on how to use two dimensional heterostructures (stacks of 2D materials) for new compact ways of generating plasmons that do not need external light sources. More precisely, we propose tunneling electrons as plasmon triggers. We thus design a device consisting of a 1 nm-thick sandwich of graphene-hBN-graphene whose activation mechanism would be by an electron that tunnels from one graphene layer to another losing energy in the process that is invested into exciting plasmons. We predict a generation efficiency that can reach one plasmon per tunneled electron and that is robust upon distortions and variations in doping. Additionally, we complete this study by analyzing graphene-insulator-metal structures, which are unfortunately less efficient in the generation than their graphene-hBN-

graphene counterparts.

In summary, the outcomes of this thesis open new paths towards a more efficient generation of nonlinear processes in solid nanoarchitectures and optics-free manipulation at the nanoscale for future optoelectronic devices.

Resumen

Desde el advenimiento de la tecnología moderna, los mayores desarrollos científicos en Electrónica, Fotónica y otras ramas de la Física han venido de la mano con la miniaturización y la velocidad. Una prueba de esto es el gran éxito de la Ley de Moore[1] que predijo que el número de transistores por microprocesador de precio asequible se doblaría cada dos años y que que no habría sido posible si los transistores hubiesen mantenido su tamaño original. A finales de 2018 investigadores del MIT y de la Universidad de Colorado batieron un nuevo récord del transistor más pequeño hasta la fecha[2] de tan solo 2.5 nm de tamaño. En lo que a 2019 se refiere, ya hay transistores de 5 nm disponibles en el mercado[3,4] y cuyo tamaño se espera reducir a 3 nm para 2021. Considerando estas dimensiones, es de vital importancia tanto entender como poder manipular los materiales en la nanoescala, donde se compartan de una manera totalmente diferente a cómo lo hacen macroscópicamente.

Dado este contexto, los investigadores han puesto especial empeño en encontrar explicaciones a diversos fenómenos en la nanoescala, en construir y diseñar nuevos nanodispositivos y en proponer o predecir nuevos mecanismos para lograr las nuevas generaciones de chips y circuitos integrados. De hecho, el ascenso de los famosos materiales de baja dimensionalidad (grafeno, dicalcogenuros de metales de transición, cupratos, hBN, fósforo negro, nanotubos de carbono y otros), *i.e.*, aquellos cuyos planos atómicos están enlazados por fuerzas débiles de van der Waals (2D) o cuyos átomos están ordenados en cadenas o tubos (1D), ha venido influenciado por la constante búsqueda de nuevos diseños más compactos y eficientes. En esta tesis, estudiamos las propiedades ópticas de algunos de estos materiales y cómo se modifican debido a la interacción con electrones que, dependiendo del caso concreto, dopantes (añadidos al material) o que inciden en haces de electrones altamente focalizados.

Más en particular, empezamos con un análisis exhaustivo de plasmones, la oscilación colectiva de electrones acoplada a la luz, en nanotubos de carbono finitos altamente dopados. A continuación, exploramos cómo seleccionar el modo del plasmón adecuado usando haces de electrones además de cómo mejorar la interacción entre dos emisores cuánticos cuando el modo plasmónico principal hace de mediador. Predecimos un valor récord de 10^8 para el factor de Purcell que respalda el uso de nanotubos de carbono como elementos plasmónicos activos de gran potencial para aplicaciones en optoelectrónica y óptica cuántica.

Continuamos con sistemas unidimesionales pero esta vez eligiendo cadenas atómicas para emular estructuras sólidas simples donde examinar la dinámica de los electrones cuando están guiados por campos fuertes. Más concretamente, abordamos las cuestiones aún pendientes sobre el papel que juegan las interacciones electrón-electrón y la elección apropiada de material para la generación más eficiente de armónicos altos, y comprobamos nuestras conclusiones en sistemas 1D más realistas: los nanotubos de carbono. Así pues, encontramos que la adición de una pequeña cantidad de carga dopante puede producir excitación de plasmones intrabanda que concentran el campo incidente y fomentan la eficiencia de la generación de armónicos altos.

Después, pasamos a investigar cómo emplear heteroestructuras bidimensionales (pilas de materiales 2D) para desarrollar nuevas formas más compactas de generar plasmones sin tener que utilizar fuentes externas, es decir, proponemos usar electrones de efecto túnel como activadores plasmónicos. El dispositivo que planteamos es un sándwich de grafeno-hBN-grafeno cuyo mecanismo de activación sería por medio de un electrón que salta de una lámina de grafeno a la otra por efecto túnel, que en el proceso pierde energía y que ésta es invertida en excitar plasmones. En efecto, predecimos una eficiencia de generación que puede alcanzar un plasmón por electrón que salta por efecto túnel y que se mantiene a pesar de las posibles distorsiones por

rotación de las láminas o de los cambios en el dopado. Además, completamos este estudio analizando el caso para estructuras de grafeno-aislante-metal y comprobamos que, desafortunadamente, son menos eficientes que sus homólogas de grafeno-hBN-grafeno.

En resumen, los resultados de esta tesis abren la puerta hacia la generación de procesos no lineales más eficientes en nanoarquitecturas sólidas y hacia la manipulación en la nanoescala sin elementos ópticos para futuros nanodispositivos optoelectrónicos.

Contents

1 Introduction

$$e^{i\pi} + 1 = 0$$

– *Euler*

The first hints of an emerging area of Physics were envisioned by Richard Feynman in his lecture *There's Plenty of Room at the Bottom: An Invitation to Enter a New Field of Physics* at the American Physical Society meeting at Caltech in 1959.[5] In this talk, he anticipated that the development of experimental techniques at the nanoscale would revolutionize science and produce a huge impact in society. Nevertheless, it was not until 1974 when Norio Taniguchi coined the word *Nanotechnology*[6] for this new field. Ever since that date, Nanoscience grew exponentially, ignited by two great breakthroughs: the invention of the first scanning tunneling microscope in 1981[7] that provided unmatched atomic resolution, and the discovery of fullerenes in 1985[8] as platforms to build devices with applications in electronics at the nanoscale.

In parallel to the advances in Nanoscience, the emergence of the first lasers,[9–13] of the low-loss optical fibers,[14] and the fabrication of semiconductor optical devices[15–18] triggered the rebirth of two other great disciplines, the so-called Electronics and Photonics. Whereas Electronics involves the control of

charge carriers, Photonics comprises the control of photons. However, both areas are intertwined enough to often find terms such as Optoelectronics or Electro-optics that refer to the fact that photons can also control electrons and vice versa.[19] Hence, these fields are widely used to designate the generation, manipulation, detection, and emission of photons and electrons in vacuum or matter by signal processing, modulation, sensing, amplification or switching.

The efforts towards speeding up operations and reducing the critical dimension of devices pushed research in Optoelectronics down to the nanoscale, opening up a wide range of new disciplines like Nano-optoelectronics, Nanoelectronics, Molecular nanotechnology, Nanometrology, and also, the one where our research is framed in, Nanophotonics.

The focus of this thesis is on finding novel mechanisms to manipulate, use and generate plasmons, the collective oscillations of free electrons coupled to light. The *glamour of plasmons*[20] comes from their outstanding properties for light concentration and enhancement (even beating the diffraction limit), as well as, their broadband response that ranges from the THz to the visible-NIR. This makes plasmons useful for optical sensors, detectors, and modulators.[21–23]

Many of these properties are boosted when plasmons are supported by low dimensional materials, whose atoms are arranged in a plane, in a tube or lie in a line, thus we focus primarily on carbon allotropes, direct successors of the fullerenes mentioned above, because of their good performance and suitable characteristics for our purposes, as we shall see.

More specifically, we start with a comprehensive study of plasmons in finite highly-doped carbon nanotubes. The axial symmetry of these structures along with their small transversal sizes in comparison to their lengths and especially to the plasmon and light wavelengths, make them effectively one-dimensional. Henceforth, we look into the properties of these plasmons, namely how to generate them with electron beams and how they interact with quan-

tum emitters.

We then continue with 1D systems and analyze how the linear and nonlinear response of atomic chains, the *fruit flies* of material science and condensed matter, are effected by plasmons, doping, and electron interactions. After that, we proceed with more realistic systems and look into these effects in carbon nanotubes. Ultimately, we move on towards 2D symmetries and explore the possibilities that tunneling electrons offer to trigger plasmons in 2D heterostructures.

The theoretical building blocks of our calculations are succinctly introduced below to provide an overview of the formalism as well as a guide for future reference.

1.1 Electronic properties of materials

1.1.1 Free electrons

The *free-electron model*, also called Drude-Sommerfeld model,[24,25] describes the behavior of a Fermi gas: non-interacting electrons that fulfill Pauli's exclusion principle. This model relies on the following three approximations:

(i) *free electrons*: ionic cores play no role in the electron dynamics.

(ii) *independent electrons*: electron-electron interactions are neglected.

(iii) *relaxation-time*: (a) the electron collision time is independent of the positions of the electron and (b) thermal equilibrium is achieved only through these collisions.

Electron dynamics in a Fermi gas is governed by a Hamiltonian that only

contains the kinetic term

$$\mathcal{H}_0 = -\frac{\hbar^2}{2m}\sum_{l=1}^{N}\nabla_l^2. \tag{1.1}$$

For one free Fermion under periodic boundary conditions (cubic box of side L and volume $\mathcal{V} = L^3$), we can exactly solve (1.1), retrieve its eigenstates $\psi_{\mathbf{k}}(\mathbf{r}) = \mathrm{e}^{\mathrm{i}\mathbf{k}\mathbf{r}}/\sqrt{\mathcal{V}}$, and its eigenenergies

$$E_0(\mathbf{k}) = \frac{\hbar^2 k^2}{2m}, \tag{1.2}$$

where $\mathbf{r} = (x, y, z)$, $\mathbf{k} = (2\pi/L)(l_x, l_y, l_z)$, $l_{x,y,z} \in \mathbb{Z}$ and $k = |\mathbf{k}|$. The ground state ($T = 0$) for many free electrons is thus the product of all one-electron wave functions.

Nevertheless, to calculate any thermodynamic quantity, the number of electrons, or the density of electronic states, we have to sum over all possible $\mathbf{k}$, *i.e.*, $\sum_{\mathbf{k}}$. As every $\mathbf{k}$ point is associated with a volume of $(2\pi/L)^3$, for continuous functions, these sums transform into integrals as

$$\lim_{\mathcal{V}\to\infty}\frac{1}{\mathcal{V}}\sum_{\mathbf{k}} \;\to\; \int\frac{d^3\mathbf{k}}{(2\pi)^3}.$$

Now, we can readily evaluate the *density of states* $\mathcal{D}$, namely, the number of states available to be occupied per energy interval

$$\mathcal{D}(E) = \frac{2}{(2\pi)^3}\int d^3\mathbf{k}\;\delta[E - E_0(\mathbf{k})] = \frac{m}{\hbar^3\pi^2}\sqrt{2mE}, \tag{1.3}$$

where the over all constant 2 accounts for spin degeneracy.

Before determining the density of electrons, we first note that the total number of electrons N occupies a sphere of radius k_{F}, the wave vector associated with the energy of the highest occupied electron state E_{F}, as the

energy of free electrons is proportional to the square of the wave vector (1.2). Hence, defining the *density of electrons* as $n = N/\mathcal{V}$ we have

$$n = \frac{2}{(2\pi)^3} \int d^3\mathbf{k}\ \Theta(k_\mathrm{F} - k) = \frac{{k_\mathrm{F}}^3}{3\pi^2}, \tag{1.4}$$

where the occupation function is defined as $f_\mathbf{k} = f_k = \Theta(k_\mathrm{F} - k)$, and Θ is the Heaviside step function.

Conversely, from eq. (1.4) we can find expressions for the so-called Fermi wave vector k_F and Fermi energy E_F as $k_\mathrm{F} = (3\pi^2 n)^{1/3}$ and $E_\mathrm{F} = \hbar^2 {k_\mathrm{F}}^2/(2m)$, respectively.

If instead of having $T = 0$ we consider finite temperatures, electrons do not lie in the ground state anymore. Their occupation function smears out around E_F, which for $T \neq 0$ is called Fermi level or chemical potential, following a *Fermi-Dirac distribution*

$$f(E) = \frac{1}{1 + \mathrm{e}^{(E - E_\mathrm{F})/(k_B T)}}, \tag{1.5}$$

as predicted by calculating the grand canonical partition function and grand potential of the system.[25] In eq. (1.5), $k_B = 8.62 \times 10^{-5}$ eV/K is the Boltzmann constant.

The Drude-Sommerfeld model succeeds in describing many properties of conduction electrons in metals especially for alkali and noble metals, but fails to assess many other properties such as transport or the behavior at low temperature of the electrical conductivity.[24]

It is then necessary to bring out more accurate models that fix the limitations of the free-electron model. Our attempts will go as follows. First, we will introduce a periodic potential which will account for the interactions of the free electrons with the ions of a perfect crystal (our solid). Second, we will consider the case of electrons tightly bound to their atoms; and finally, we will adiabatically switch on electron-electron interactions, transforming,

in this way, our previous Fermi gas into a Fermi liquid.

1.1.2 Bloch's theorem and tightly bound electrons

Most solid materials are crystalline, *i.e.*, their atoms are arranged in regular periodic arrays called *direct lattices* (or Bravais lattices). These lattices are perfectly traced by the lattice vectors: $\mathbf{s} = \sum_i^{\dim} n_i \boldsymbol{a}_i$, where $n_i \in \mathbb{N}$, "$\dim$" is the dimensionality of the solid ($\dim = 1, 2, 3$), and the $\boldsymbol{a}_i$ are the primitive vectors that connect nearby atoms and span the lattice. Equivalently, we can also reconstruct the lattice by translating a given volume of space without overlaps, the so-called unit cell. This perfect assembling from smaller units implies that the study of the properties of the entire solid can be reduced to the much simpler study of the unit cell and the primitive vectors.

Given the periodicity of the crystal, it is then natural to define the potential given by the ions in the solid as also periodic in $\mathbf{s}$

$$U(\mathbf{r}) = U(\mathbf{r} + \mathbf{s}).$$

The insertion of this into the single-electron Hamiltonian $\mathcal{H} = -(\hbar^2/2m)\,\nabla^2 + U(\mathbf{r})$ renders Bloch functions, that is, plane-wave-like solutions for the eigenstates

$$\psi(\mathbf{r} + \mathbf{s}) = \mathrm{e}^{\mathbf{iks}}\psi(\mathbf{r}), \tag{1.6}$$

where $\mathbf{k}$ is now the crystal momentum of the *reciprocal lattice*, whose primitive vectors $\mathbf{b}_j$ ($j = 1, 2, ..., \dim$) satisfy $\mathbf{b}_j \cdot \boldsymbol{a}_i = 2\pi\delta_{ij}$, where δ_{ij} is the Kronecker delta. Analogous to the unit cell, the unit of volume in k-space before the properties repeat again is called the *first Brilluoin zone*. The relation (1.6) is known as *Bloch's theorem*, which physically means, in words of F. Bloch himself,[26] "that the wave differs from the plane wave of free electrons only by a periodic modulation".

As a more sensible scenario of the actual distribution of the electrons in a

solid, we can model electrons when they are tightly bound to their atoms and overlap weakly with their neighbors. This description is indeed complementary to the Bloch waves described above since electrons would be distributed following Wannier functions, which are simply a set of orthonormal functions constructed by linear combination of Bloch functions. Accordingly, we can find the matrix elements of the Hamiltonian of the system in this new basis as

$$\mathcal{H}_{\mathrm{TB}} = \sum_{\boldsymbol{l},\boldsymbol{\delta}} |\, \boldsymbol{l} \,\rangle\, t\, \langle\, \boldsymbol{l} + \boldsymbol{\delta} \,| + \sum_{\boldsymbol{l}} |\, \boldsymbol{l} \,\rangle\, \eta\, \langle\, \boldsymbol{l} \,|, \tag{1.7}$$

where $|\, \boldsymbol{l} \,\rangle$ is the atomic-site state vector associated to a given Wannier function, $\boldsymbol{\delta}$ is the vector pointing from $\boldsymbol{l}$ to its nearest neighbours, t is the so-called *hopping* energy that accounts for the interaction between an electron in $\boldsymbol{l}$ and another in $\boldsymbol{l} + \boldsymbol{\delta}$, and η is the on-site energy.

The Hamiltonian in eq. (1.7) is the so-called *tight-binding (TB) Hamiltonian*. Even though it provides a good description of the energy bands in d-shells of transition metals and the electronic structure of insulators,[24] no physical system is accurately described by just a TB Hamiltonian.[25] In consequence, it is essential to loosen our restrictions and introduce electron-electron interactions, which have been neglected so far.

1.1.3 Electron-electron interactions

The *Hartree approximation*[25,27] assumes that the electron-electron interaction at the position of a given electron arises from the averaged electrostatic potential generated by all the other electrons

$$U_{ee}(\mathbf{r}) = e^2 \int d\mathbf{r}'\, \frac{n(\mathbf{r}')}{|\mathbf{r} - \mathbf{r}'|}, \tag{1.8}$$

where the density of electrons is $n(\mathbf{r}) = \sum_j |\psi_j(\mathbf{r})|^2$. Hence, we can decompose the Hamiltonian of the full many body system into single-electron

Hamiltonians of the form

$$\mathcal{H} = -\frac{\hbar^2}{2m}\nabla^2 + U(\mathbf{r}) + U_{ee}(\mathbf{r}). \tag{1.9}$$

Although this approach may seem reasonable and intuitive, it actually does not satisfy Pauli's exclusion principle and represents a very drastic approximation. For this reason, we need to correct U_{ee} by adding an exchange potential, which accounts for the energy spent by electrons when they flip their position $\mathbf{r}$ and $\mathbf{r}'$ at the moment of the interaction.

The new one-electron wave functions depend now on spin σ_j, $\psi_j(\mathbf{r}, \sigma_j)$, and can be combined to form many-body electron wave functions like $\Psi(\mathbf{r}) = \Pi_j \psi_j(\mathbf{r}, \sigma_j)$. In the associated basis, $|\Psi\rangle$, the matrix elements of the total Hamiltonian, including exchange, are

$$\begin{aligned}\langle\, \Psi \,|\, \mathcal{H} \,|\, \Psi \,\rangle = \sum_{j,\sigma_j} \int d\mathbf{r}\; \psi_j^*(\mathbf{r}, \sigma_j) \frac{-\hbar^2}{2m}\nabla^2 \psi_j(\mathbf{r}, \sigma_j) + U(\mathbf{r})|\psi_j(\mathbf{r}, \sigma_j)|^2 + \\ + \frac{1}{2}\int d\mathbf{r}\, d\mathbf{r}'\; \frac{e^2}{|\mathbf{r} - \mathbf{r}'|} \sum_{j,j',\sigma_{j,j'}} [|\psi_j(\mathbf{r}, \sigma_j)|^2 |\psi_{j'}(\mathbf{r}', \sigma_{j'})|^2 - \\ - \psi_j^*(\mathbf{r}, \sigma_j)\psi_{j'}^*(\mathbf{r}', \sigma_{j'})\psi_j(\mathbf{r}', \sigma_{j'})\psi_{j'}(\mathbf{r}, \sigma_j)].\end{aligned} \tag{1.10}$$

The Hamiltonian (1.10) is said to be in the *Hartree-Fock (HF) approximation*. Certainly, the HF Hamiltonian does not include the effects of screening or correlations but it works for quantifying some measurable quantities. By solving eq. (1.10) we can estimate the ground state of electrons reliably, as well as calculate fairly precisely the dipole moment of our system. Incidentally, we can retrieve the lowest lying excited states which in turn, provide us with an estimation of ionization potentials.

Indeed, some other more accurate theories address the many-body problem: density functional theory (DFT), time-dependent density functional theory (TDDFT), or quantum Monte Carlo, but these are extremely computation-

ally demanding. For our purposes, the HF Hamiltonian will be sufficient and will act as the starting point for our theoretical models.

1.1.4 Free electrons in lower dimensions

Before entering into the optical properties of matter it is worth stepping back and examining the free electron model for lower dimensions. This will help us when dealing with 2D solids such as graphene or other van der Waals materials, with 1D structures such as carbon nanotubes or atomic chains, or even with 0D systems if we cope with a quantum dot. To calculate the different physical parameters discussed above, we employ the same description that we report in sec. 1.1.1 but applied to lower dimensions. A comparison of some of the most relevant quantities is gathered in Tab. 1.1.

Table 1.1: Electronic parameters for free electrons in different dimensions

Parameter	Symbol	3D	2D	1D
Density of states	$\mathcal{D}(E)$	$\frac{\sqrt{2m^3E}}{\hbar^3\pi^2}$	$\frac{m}{\pi\hbar^2}$	$\frac{1}{\hbar\pi}\sqrt{\frac{m}{2E}}$
Density of electrons	n	$\frac{{k_\mathrm{F}}^3}{3\pi^2}$	$\frac{{k_\mathrm{F}}^2}{2\pi}$	$\frac{k_\mathrm{F}}{\pi}$
Discrete to continuum	$\sum_{\mathbf{k}}$	$\mathcal{V}\int\frac{d^3\mathbf{k}}{(2\pi)^3}$	$\mathcal{A}\int\frac{d^2\mathbf{k}}{(2\pi)^2}$	$L\int\frac{dk}{2\pi}$

Note that in 0D there is no free motion and as a result, there does not exist such k-space and the available states exist at discrete energies E_j, *i.e.*, $\mathcal{D}(E) = 2\sum_j \delta(E - E_j)$.

The Fermi wave vectors are obtained from the expressions for n and in consequence, the Fermi energy is retrieved straight away by $E_\mathrm{F} = \hbar^2{k_\mathrm{F}}^2/2m$. Interestingly, the density of states in 2D does not depend on energy and thus,

there are always available states.

1.2 Optical properties of materials

1.2.1 Maxwell's equations. Foundations of electromagnetism

Maxwell's equations describe the interaction of matter immersed in electromagnetic (EM) fields.[25,28,29] They provide us with a classical phenomenological description that is very useful to describe light-matter interactions since complicated long-range interactions are effectively comprised within continuous functions such as refractive indeces, surface conductivities, and electron currents. Macroscopically, these equations are

$$\begin{aligned}
\nabla \cdot \mathbf{D}(\mathbf{r},t) &= 4\pi\rho(\mathbf{r},t), \\
\nabla \times \mathbf{E}(\mathbf{r},t) &= -\frac{1}{c}\partial_t \mathbf{B}(\mathbf{r},t), \\
\nabla \cdot \mathbf{B}(\mathbf{r},t) &= 0, \\
\nabla \times \mathbf{H}(\mathbf{r},t) &= \frac{4\pi}{c}\mathbf{j}(\mathbf{r},t) + \frac{1}{c}\partial_t \mathbf{D}(\mathbf{r},t).
\end{aligned} \tag{1.11}$$

Here, $\mathbf{E}$ is the electric field, $\mathbf{B}$ the magnetic field, $\mathbf{D}$ the displacement field, $\mathbf{H}$ the magnetizing field, ρ the electron charge density, and $\mathbf{j}$ the electron current density. Incidentally, the charge and current densities (sources) are related through the *continuity equation*

$$\nabla \cdot \mathbf{j}(\mathbf{r},t) + \partial_t \rho(\mathbf{r},t) = 0. \tag{1.12}$$

The fields can also be related self-consistently via the *constitutive relations*. These do not need from sources but from the permittivity ϵ and the permeability μ of the material which fully contain (in a single function, often a tensor)

its optical properties

$$\begin{aligned} \mathbf{D} &= \epsilon\mathbf{E} = \mathbf{E} + 4\pi\mathbf{P}, & \mathbf{P} &= \chi\mathbf{E}, \\ \mathbf{B} &= \mu\mathbf{H}, & \mathbf{j} &= \sigma\mathbf{E}. \end{aligned} \tag{1.13}$$

Now, we have also introduced the macroscopic polarization $\mathbf{P}$, the conductivity σ, and the electric susceptibility χ, whose physical meaning we will explain below.

At the borders, these fields further satisfy the renowned *boundary conditions*

$$\begin{aligned} \hat{\mathbf{n}} \times (\mathbf{E}_2 - \mathbf{E}_1) &= 0, & \hat{\mathbf{n}} \cdot (\mathbf{B}_2 - \mathbf{B}_1) &= 0, \\ \hat{\mathbf{n}} \cdot (\mathbf{D}_2 - \mathbf{D}_1) &= 4\pi\rho_s, & \hat{\mathbf{n}} \times (\mathbf{H}_2 - \mathbf{H}_1) &= \frac{4\pi}{c}\mathbf{j}_s, \end{aligned} \tag{1.14}$$

where $\hat{\mathbf{n}}$ is a normal unitary vector pointing from medium 1 towards medium 2, and ρ_s and $\mathbf{j}_s$ are the charge and current densities at the interface, respectively.

In general, the fields that we use to study light-matter interactions are time-harmonic (monochromatic), *i.e.*, $\mathbf{E}(\mathbf{r}, t) = \mathbf{E}(\mathbf{r})\,\mathrm{e}^{-\mathrm{i}\omega t} + c.\,c.$. For these fields, Maxwell's equations (1.11) are accordingly modified by substituting $\partial_t \to -\mathrm{i}\omega$. If we further assume that they will be indeed plane waves, $\mathbf{E}(\mathbf{r}, t) = \mathbf{E}\,\mathrm{e}^{\mathrm{i}\mathbf{k}\cdot\mathbf{r} - \mathrm{i}\omega t} + c.\,c.$, we can conveniently separate the components of a given field into two polarizations: one parallel (p) to the plane of incidence and another perpendicular (s) to it, $\mathbf{E} = \mathbf{E}^{(s)} + \mathbf{E}^{(p)}$. In this manner, we can define the *reflection* r and *transmission* t coefficients at the interface that separates a medium 1 (ϵ_1, μ_1) from another medium 2 (ϵ_2, μ_2), for a plane wave of am-

plitude $\mathbf{E}_0$ impinging from 1, and for the two different polarizations as

$$E_r^{(p)} = r_p E_0^{(p)}, \qquad E_t^{(p)} = t_p E_0^{(p)}, \tag{1.15}$$

$$E_r^{(s)} = r_s E_0^{(s)}, \qquad E_t^{(s)} = t_s E_0^{(s)}, \tag{1.16}$$

where ($\hat{\mathbf{n}} \cdot \mathbf{k}_j = k_{\perp j}, j = 1, 2$)

$$r_p = \frac{\epsilon_2 k_{\perp 1} - \epsilon_1 k_{\perp 2}}{\epsilon_2 k_{\perp 1} + \epsilon_1 k_{\perp 2}}, \qquad t_p = \frac{2\epsilon_2 k_{\perp 1}}{\epsilon_2 k_{\perp 1} + \epsilon_1 k_{\perp 2}} \sqrt{\frac{\mu_2 \epsilon_1}{\mu_1 \epsilon_2}}, \tag{1.17}$$

$$r_s = \frac{\mu_2 k_{\perp 1} - \mu_1 k_{\perp 2}}{\mu_2 k_{\perp 1} + \mu_1 k_{\perp 2}}, \qquad t_s = \frac{2\mu_2 k_{\perp 2}}{\mu_2 k_{\perp 1} + \mu_1 k_{\perp 2}}, \tag{1.18}$$

after properly applying the boundary conditions (1.14). Incidentally, p-polarized waves are often called transverse magnetic (TM) modes, whereas s-polarized are transverse electric (TE) modes.

Finally, another powerful relation that appears after slightly manipulating the source-free ($\rho = 0$ and $\mathbf{j} = 0$) Maxwell's equations in combination with the constitutive relations[30] is

$$\epsilon = 1 + 4\pi \frac{\mathrm{i}\sigma}{\omega}. \tag{1.19}$$

In the following, we will mainly focus on describing the optical properties of metals as these are the materials of interest in this thesis.

1.2.2 Drude model

The *Drude model*[25, 29, 30] accounts for transport of free electrons in metals when driven by external EM fields at low frequencies and damped by some averaged frictional force. Accordingly, the classical master equation of motion (EOM) for the electrons follows

$$m\partial_t^2 \mathbf{r} + m\gamma \partial_t \mathbf{r} = -e\mathbf{E}(\mathbf{r})\mathrm{e}^{-\mathrm{i}\omega t}, \tag{1.20}$$

where m is the effective mass of the electrons, $-e$ is the electron charge and γ is the damping coefficient, *i.e.*, the inverse of the so-called relaxation time, τ, of the electrons.

Introducing the ansatz $\mathbf{r}(t) = \mathbf{r}\mathrm{e}^{-\mathrm{i}\omega t}$ and remembering that $\mathbf{P}(\mathbf{r}) = -ne\mathbf{r} = (\epsilon - 1)\mathbf{E}(\mathbf{r})/4\pi$, where n is the electron density, we get

$$\epsilon(\omega) = 1 - \frac{\omega_p^2}{\omega^2 + \mathrm{i}\omega\gamma}. \tag{1.21}$$

The parameter $\omega_p = \sqrt{4\pi ne^2/m}$ is the *plasma frequency* of the electrons oscillating in the bulk and marks the point at which a metal switches from being reflective to transparent. Frequently, we have to introduce a constant offset due to d-band contributions and then replace the 1 in eq. (1.21) by a background permittivity, ϵ_b.

The Drude model is fairly accurate for energies in the infrared regime (below ~ 2 eV) but starts failing for higher ones. If we need to go beyond and find a permittivity more suitable for the NIR-visible regime, we need to add the influence of interband transitions into the EOM (1.20). Basically, we include a restoring term ($\alpha\mathbf{r}$) and substitute the damping coefficient, γ, by the radiative damping coefficient for bound electrons, Γ. Defining $\tilde{\omega}_b^2 = 4\pi\tilde{n}e^2/m$ as the plasma frequency of these bound electrons of density $\tilde{n}$ we find

$$\epsilon(\omega) = 1 + \frac{\tilde{\omega}_b^2}{\omega_0^2 - \omega^2 - \mathrm{i}\omega\Gamma}\ , \tag{1.22}$$

where $\omega_0 = \sqrt{\alpha/m}$ is the resonant frequency of the system in the NIR-visible part of the spectrum.

The combination of eq. (1.21) and eq. (1.22) gives a precise analytical expression for the permittivity in metals that works satisfactorily for energies below ~ 2.4 eV.

1.2.3 Surface plasmons

It is worth having a closer look at these plasma oscillations confined to interfaces, and more specifically to metal-dielectric interfaces. Under the right conditions, when light impinges upon a metal it can couple to the oscillations of conduction electrons producing a *surface plasmon* (SP) that can propagate along the surface.[20,29,31] From a mathematical perspective, SPs are solutions of the *Helmholtz equation*, which arises by properly handling the source-free ($\rho = 0$ and $\mathbf{j} = 0$) Maxwell's equations (1.11) for harmonic fields, in combination to the constitutive relations (1.13)

$$\nabla^2 \mathbf{E}(\mathbf{r}) = -\epsilon \frac{\omega^2}{c^2} \mathbf{E}(\mathbf{r}), \tag{1.23}$$

and equivalently for magnetic fields. Taking the interface to be in the plane at $z = 0$, the permittivity is distributed as $\epsilon = \epsilon_{\mathrm{m}}(\omega)$ for $z < 0$ and $\epsilon = \epsilon_{\mathrm{d}}$ for $z > 0$ as indicated in Fig. 1.1.

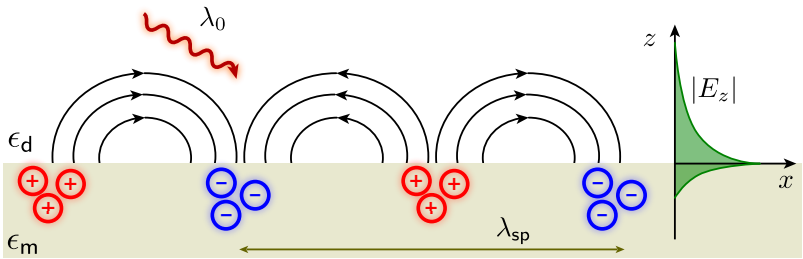

Figure 1.1: **Surface plasmon polariton.** *Metal-dielectric interface with a traveling p-polarized wave confined at $z = 0$. The permittivities of the metal and the dielectric are indicated as ϵ_{m} and ϵ_{d}, respectively. The blue and red circles with $+$ and $-$ inside represent the collective motion of the electrons whereas the semi-circular lines entering and leaving the metal correspond to the light coupled to the electron oscillation that propagates along the surface. As the E-field associated to the polariton decays exponentially from the surface, we illustrate this through the shaded green areas labeled with $|E_z|$. We denote the wavelength of the incident light as λ_0 and the wavelength of the surface plasmon as λ_{sp}.*

Without losing generality, we can assume that the propagation direction goes along the x-direction and thus, drop the spatial variation along the y-axis, that is, $\mathbf{k} = k_{\|}\hat{\mathbf{x}} + k_z\hat{\mathbf{z}}$. Therefore, there would be two possible ansatzes to solve eq. (1.23) that correspond to plane waves that are either p-polarized or s-polarized. As it is not possible to excite plasmons with s-polarized light,[31] we choose the TM mode ansatz

$$\mathbf{E}(\mathbf{r},\omega) = (E_x\hat{\mathbf{x}} + E_z\hat{\mathbf{z}})\,\mathrm{e}^{-\mathrm{i}\omega t}\,\mathrm{e}^{\mathrm{i}k_{\|}x}\,\mathrm{e}^{-s_z k_z z}, \tag{1.24}$$

$$\mathbf{H}(\mathbf{r},\omega) = H_y\hat{\mathbf{y}}\,\mathrm{e}^{-\mathrm{i}\omega t}\,\mathrm{e}^{\mathrm{i}k_{\|}x}\,\mathrm{e}^{-s_z k_z z}. \tag{1.25}$$

where $s_z = \mathrm{sign}\{z\}$. Moreover, the momentum parallel to the surface $k_{\|}$ is preserved at both sides of the interface. That is the reason why it is frequently designated as the *propagation constant* and indicated as β.

By inserting the ansatz (1.25) for the magnetic field into the Helmholtz equation (1.23) we retrieve the relation

$$k_z^2 = \beta^2 - \epsilon\frac{\omega^2}{c^2}. \tag{1.26}$$

Additionally, if we introduce the eqs. (1.24) and (1.25) into the source-free Maxwell's equations (1.11) we find the governing equations to be

$$E_x = \mathrm{i}s_z\frac{k_z}{\epsilon\omega/c}\,H_y \qquad \text{and} \qquad E_z = -\frac{\beta}{\epsilon\omega/c}\,H_y. \tag{1.27}$$

Now, applying the corresponding boundary conditions (1.14) for $\rho_s = 0$, $\mathbf{j}_s = 0$, $\hat{\mathbf{n}} = \hat{\mathbf{z}}$, 1 being the metal ($\epsilon_1 = \epsilon_{\mathrm{m}}(\omega)$) and 2 the dielectric ($\epsilon_2 = \epsilon_{\mathrm{d}}$), we find

$$E_{x2} - E_{x1} = 0 \qquad \text{and} \qquad \frac{\epsilon_1}{k_{z1}}E_{x1} + \frac{\epsilon_2}{k_{z2}}E_{x2} = 0,$$

from which it follows that

$$\frac{k_{z2}}{k_{z1}} = -\frac{\epsilon_2}{\epsilon_1}. \tag{1.28}$$

Finally, combining the eqs. (1.28) and (1.26) we obtain the *plasmon dispersion relation*

$$\beta = \frac{\omega}{c}\sqrt{\frac{\epsilon_1\epsilon_2}{\epsilon_1+\epsilon_2}}. \tag{1.29}$$

Note that we have chosen the materials to be a metal and a dielectric on purpose. In fact, for eq. (1.28) to hold with our choice of positive and real decay constants k_{z1} and k_{z2}, ϵ_1 and ϵ_2 must have opposite signs, what is conveniently satisfied if medium 2 is a dielectric: $\epsilon_2 = \epsilon_\mathrm{d} > 0$, and medium 1 is a metal: $\mathrm{Re}\{\epsilon_1\} = \mathrm{Re}\{\epsilon_\mathrm{m}\} < 0$.

Interestingly, eq. (1.28) also appears when the denominator of the reflection coefficient for p-polarized waves (1.17) (taking there $k_{\perp 1} = k_{z1}$ and equivalently for 2) is set to zero. For this reason surface plasmons are frequently studied by finding the poles of this parameter.

Once we have obtained the dispersion relation, we can characterize an SP by its *propagation length* $L_\mathrm{p} = (2\,\mathrm{Im}\{\beta\})^{-1}$, that is, how far it travels until the initial field has decreased $1/e$, and by its wavelength $\lambda_\mathrm{sp} = 2\pi/\mathrm{Re}\{\beta\}$ which is often shortened to λ_p for clarity but should not be confused with the wavelength associated to ω_p.

In Fig. 1.2 we have plotted the dispersion relation (1.29) for an SP propagating along a gold-air interface taking the Au permittivity in the Drude approximation (1.21). The first point we want to remark is that the lower branch asymptote for the loss-less limit ($\gamma \to 0$) sets the *surface plasmon frequency* to $\omega_\mathrm{sp} = \omega_p/\sqrt{\epsilon_\mathrm{d}+\epsilon_b}$. In this regime, the mode approaches an electrostatic character and is said to be a proper surface plasmon. The second is that the mismatch that we observe between the light line and the SP dispersion makes the excitation of the latter difficult without the proper momentum matching. To overcome this, researchers have developed different techniques such as shining a grating on top of the metal[33,34] or an AFM-like nanotip,[35,36] sending an electron beam,[37,38] placing a quantum dot near the surfaces,[39,40] or via electron tunneling.[41–43]

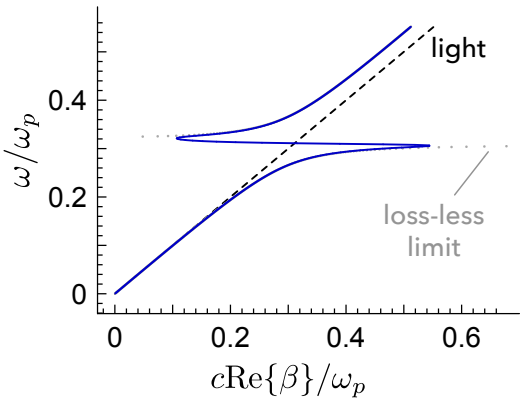

Figure 1.2: **Drude SP dispersion relation.** *Dispersion relation for SPs at a gold-air interface according to eq.* (1.29). *The Drude parameters for Au are* $\hbar\omega_p = 9.06\,eV$, $\hbar\gamma = 71\,meV$ *and* $\epsilon_b = 9.5$.[32]

1.2.4 Localized plasmons

When we nanostructure our materials, the surface plasmons that we can excite behave differently. These are called *localized plasmons* (LPs) and, in contrast to SPs, LPs do not propagate but present a dipole behavior that is confined to the nanoparticle that supports them.[20,29,31]

As it happens with SPs, mathematically, LPs are also solutions of the Helmholtz equation (1.23) when we apply the proper boundary conditions. Commonly, the size of the nanoparticle is much smaller than the wavelength of the impinging light (see Fig. 1.3) hence, the distribution of the electric field of the incident light is almost constant over the volume of this particle and thus, the problem is reduced to that of a particle in an electrostatic field.[28,31] In this electrostatic approach, $c \to \infty$ and the Helmholtz equation acquires the simpler form of the *Laplace equation*,[20,44] which for the electric potential is $\nabla^2\Phi = 0$. After solving this equation, we retrieve the electric field distribution by applying $\mathbf{E} = -\nabla\Phi$.

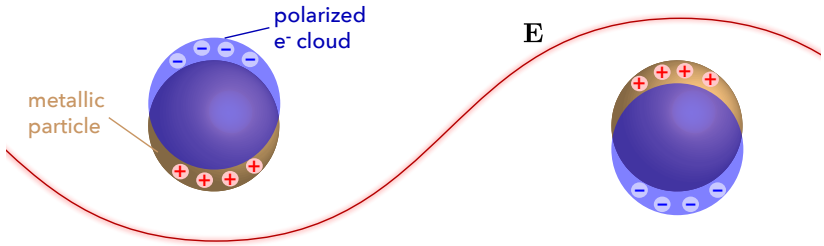

Figure 1.3: **Localized plasmon.** *Interaction of a metallic nanoparticle with resonant light. The EM plane wave (red curved line) produces a polarized electron cloud (in blue) that oscillates at the frequency of the impinging field.*

For the sake of illustration, let us consider the prototypical case of a nanosphere of radius a and permittivity ϵ_1 embedded in a medium of permittivity ϵ_2 in a uniform electrostatic field along the z-direction, $\mathbf{E}_0 = E_0\hat{\mathbf{z}}$.[28,31] Then, we solve the Laplace equation in spherical coordinates $\mathbf{r} = (r, \theta, \varphi)$ by separation of variables and find the general solution for the potential to be

$$\Phi(r,\theta) = \sum_{l=0}^{\infty} \left[A_l r^l + B_l r^{-(l+1)} \right] P_l(\cos\theta), \tag{1.30}$$

where the $P_l(\cos\theta)$ are the Legendre Polynomials of order l. The requirements that the potential has to be finite at the origin, has to approach $-E_0 z = -E_0 r\cos\theta$ for $r \to \infty$, and has to satisfy the following boundary conditions at $r = a$

$$\partial_\theta \Phi_{\text{in}} = \partial_\theta \Phi_{\text{out}} \quad \text{and} \quad \epsilon_1 \partial_r \Phi_{\text{in}} = \epsilon_2 \partial_r \Phi_{\text{out}}, \tag{1.31}$$

allow us to calculate the coefficients A_l and B_l to obtain

$$\begin{aligned} \Phi_{\text{in}} &= -\frac{3\epsilon_2}{\epsilon_1 + 2\epsilon_2} E_0 r\cos\theta, \\ \Phi_{\text{out}} &= -E_0 r\cos\theta + a^3 \frac{\epsilon_1 - \epsilon_2}{\epsilon_1 + 2\epsilon_2} E_0 \frac{\cos\theta}{r^2} = -E_0 z + \frac{\mathbf{p}\cdot\mathbf{r}}{r^3}. \end{aligned} \tag{1.32}$$

From these expressions, we can see that Φ_{out} has two well-differentiated contributions: the external, given by $E_0 r\cos\theta$, and the induced, given by $\mathbf{p}\cdot\mathbf{r}/r^3$, which as a matter of fact, corresponds to the potential produced by a dipole with dipole moment $\mathbf{p}$.

Finally, by defining the *polarizability*, *i.e.*, the parameter that quantifies the ability of an electric field to form instantaneous dipoles,[28] as $\mathbf{p} = \alpha\mathbf{E}$, we notice that the polarizability of a nanosphere is

$$\alpha = a^3 \frac{\epsilon_1 - \epsilon_2}{\epsilon_1 + 2\epsilon_2}. \tag{1.33}$$

Now, under the assumption that the particle is small with respect to the wavelength of an impinging light source, $a \ll \lambda_0$, the nanoparticle behaves as an ideal dipole and hence, we can also consider the case of impinging harmonic fields and neglect spatial retardation. The oscillating dipole then becomes $\mathbf{p}(t) = \alpha\mathbf{E}_0(\mathbf{r})\mathrm{e}^{-\mathrm{i}\omega t}$, with α still given by (1.33) which, in turn, will induce an electric field of the form

$$\mathbf{E}(\mathbf{r}) = \frac{1}{\epsilon_2}\left\{k_0^2\,(\mathbf{n}\times\mathbf{p})\times\mathbf{n}\,\frac{\mathrm{e}^{\mathrm{i}k_0 r}}{r} + [3\,\mathbf{n}\,(\mathbf{n}\cdot\mathbf{p}) - \mathbf{p}]\left(\frac{1}{r^3} - \frac{\mathrm{i}k_0}{r^2}\right)\mathrm{e}^{\mathrm{i}k_0 r}\right\}, \tag{1.34}$$

where $k_0 = \omega/c$, and $\mathbf{n}$ is a unit vector that points from the dipole position to where we measure the electric field.

If the nanosphere is metallic then $\epsilon_1 = \epsilon_{\text{m}}(\omega)$, which produces a polarizability (1.33) that will induce a large field enhancement, given by (1.34), in the surrounding of the particle by direct coupling to the external resonant light (notice also, that given the finite dimensions of the particle, there is no need of k-matching). This is true not only for metallic nanospheres but also for any other shape of a nanoparticle.[29,31] Indeed, the polarizability is also a parameter through which we can quantify how efficiently nanoparticles absorb and scatter light.

From an optics perspective, it is often more convenient to measure and

calculate the corresponding *absorption cross section* σ_{abs} (power dissipated inside the particle over the intensity of the incident field), and *scattering cross section* σ_{sct} (total radiated power over the intensity of the incident field), whose general expressions for any given nanoparticle shape or polarizability are[44]

$$\sigma_{\mathrm{sct}} = \frac{8\pi}{3}\frac{\omega^4}{c^4}\,|\alpha|^2, \tag{1.35}$$

$$\sigma_{\mathrm{abs}} = 4\pi\frac{\omega}{c}\,\mathrm{Im}\{\alpha\}. \tag{1.36}$$

The total power removed from the incident field is the sum of both cross sections and is called *extinction cross section* $\sigma_{\mathrm{ext}} = \sigma_{\mathrm{abs}} + \sigma_{\mathrm{sct}}$. For nanoparticles, the contribution of the σ_{sct} is negligible as it scales with a^6, in comparison to σ_{abs} which scales with a^3, and consequently

$$\sigma_{\mathrm{ext}} \approx \sigma_{\mathrm{abs}}. \tag{1.37}$$

As a last note, from all these calculations we see that the tunability of localized plasmons is geometrical, implying that only by changing the shape of the nanoparticle we will shift its optical response.

1.2.5 Linear response

In contrast to the classical approach that we have gone through above, the *linear response theory*[45] provides us with a quantum mechanical description of the optical response of metals as a result of an external perturbation. We use a density matrix formalism for such microscopic description as often there is a lack of information to precisely know the state of the system. Thus, we have to treat it statistically while taking into account collisional broadening.[46]

The density matrix of a system in its state (ψ_j) representation is given by

$$\rho = \sum_{jj'} \rho_{jj'} |\psi_j\rangle\langle\psi_{j'}|, \tag{1.38}$$

where the $\rho_{jj'}$ are matrix elements. Besides, note that the expectation value of a given observable $\hat{A}$ is $\langle\hat{A}\rangle = \mathrm{tr}(\rho\hat{A})$.

The EOM for the density matrix[47] is obtained by direct differentiation of eq. (1.38) in combination with the time-dependent Schrödinger's equation $\mathrm{i}\hbar\partial_t\psi(\mathbf{r},t) = \mathcal{H}\psi(\mathbf{r},t)$

$$\partial_t\rho = -\frac{\mathrm{i}}{\hbar}\left[\mathcal{H},\rho\right] - \gamma\left(\rho - \rho_0\right), \tag{1.39}$$

where we have introduced the collisional broadening via the term preceded by the phenomenological damping γ. In addition, $\mathcal{H}$ is the Hamiltonian of the system and ρ_0 is the density matrix in the equilibrium.

We can solve eq. (1.39) perturbatively[46,48] by expanding ρ into a power series of harmonics of the impinging continuous wave (CW) illumination

$$\rho = \sum_{n,s} \rho^{(ns)}\, \mathrm{e}^{-\mathrm{i}s\omega t}. \tag{1.40}$$

This depends on the harmonic order s and the perturbation order n, namely, the power of the incident electric field $(E_0)^n$. The Hamiltonian is now $\mathcal{H} = \mathcal{H}_0 - e\phi$, where $\mathcal{H}_0$ is the unperturbed part, *i.e.*, a TB-Hamiltonian (1.7), and $\phi = \phi_{\mathrm{ind}} + \phi_{\mathrm{ext}}$ is the total perturbative potential that includes the contribution of the external (ext) field applied to the system and the induced (ind) contribution arising from self-consistent induced fields. The linear response is thus given by truncating the series up to first order $\rho^{(11)} = \rho^{(1)}$ and neglecting higher orders.

As electrons follow a Fermi-Dirac distribution f_j the equilibrium density

matrix is simply $\rho^{(0)}_{jj'} = f_j \delta_{jj'}$. By inserting this in eq. (1.39), along with solutions of the unperturbed Hamiltonian in the state representation $\mathcal{H}_0|\psi_j\rangle = \hbar\varepsilon_j|\psi_j\rangle$, we can solve the EOM to first order for CW illumination [$\phi_{\text{ext}} \propto \mathrm{e}^{-\mathrm{i}\omega t}$] and find[48]

$$\rho^{(1)}_{jj'} = -\frac{e}{\hbar}(f_{j'} - f_j)\frac{\phi^{(1)}_{jj'}}{\omega - (\varepsilon_j - \varepsilon_{j'}) + \mathrm{i}\gamma}, \tag{1.41}$$

where we have taken the total potential ϕ up to first order as well since its induced part depends linearly on ρ.

Interesting relations appear when we move to the site representation by applying $\rho_{ll'} = \sum_{ll'} a_{jl} a^*_{j'l'} \rho_{jj'}$, and equivalently for $\phi_{jj'}$, where the coefficients a_{jl} are defined by $|\psi_j\rangle = \sum_l a_{jl}|l\rangle$. In this representation, the induced charge density to first order is $\rho_{\text{ind}} = -2e\rho^{(1)}_{ll'}$, in which the 2 accounts for spin. In this manner, we find a linear dependence between the induced charge and the total potential: $\rho_{\text{ind}} = \chi_0\phi$, where

$$\chi_{0,ll'} = \frac{2e^2}{\hbar}\sum_{jj'}(f_{j'} - f_j)\,\frac{a_{jl}a^*_{jl'}a^*_{j'l}a_{j'l'}}{\omega - (\varepsilon_j - \varepsilon_{j'}) + \mathrm{i}\gamma} \tag{1.42}$$

is the *non-interacting susceptibility*. Furthermore, if we separate the two contributions of the total potential and remember that $\phi_{\text{ind}} = v\rho_{\text{ind}}$ with v being the bare Coulomb interaction, we see that $\rho_{\text{ind}} = \chi_0\phi_{\text{ext}} + \chi_0\, v\, \rho_{\text{ind}}$ and thus

$$\rho_{\text{ind}} = (1 - \chi_0 v)^{-1}\,\chi_0\,\phi_{\text{ext}} = \chi\,\phi_{\text{ext}}, \tag{1.43}$$

where this new $\chi = (1-\chi_0 v)^{-1}\,\chi_0$ is under the *random phase approximation* (RPA). The power of the RPA (1.43) lies in that it relates controllable "knowns" with pivotal "unknowns". Usually, when studying optical properties of materials we can only be sure of the type of impinging light (ϕ_{ext}), and what the electronic structure of the material is (χ_0). So, just by knowing these two, we can manage to predict its optical response (ρ_{ind}).

1.2.6 Nonlinear response

Applying this perturbative approach we can also obtain the nonlinear response when truncating to higher orders in the series for the density matrix (1.40). Although the formalism is explained elsewhere,[48] we reproduce it here for completeness.

We start by expressing the EOM (1.39) into its state representation

$$\begin{aligned}\partial_t \rho_{jj'} &= -\frac{\mathrm{i}}{\hbar}\sum_{j''}\left(\mathcal{H}_{jj''}\rho_{j''j'} - \rho_{jj''}\mathcal{H}_{j''j'}\right) - \gamma\left(\rho_{jj'} - \rho^{(0)}_{jj'}\right)\\ &= -\mathrm{i}\left(\varepsilon_j - \varepsilon_{j'}\right)\rho_{jj'} + \frac{\mathrm{i}e}{\hbar}\sum_{j''}\left(\phi_{jj''}\rho_{j''j'} - \rho_{jj''}\phi_{j''j'}\right) - \gamma\left(\rho_{jj'} - \rho^{(0)}_{jj'}\right)\\ &= -\mathrm{i}\left(\varepsilon_j - \varepsilon_{j'}\right)\rho_{jj'} + \frac{\mathrm{i}e}{\hbar}\sum_{j''}\left(\phi_l - \phi_{l'}\right)a^*_{jl}a_{j'l'}\rho_{ll'} - \gamma\left(\rho_{jj'} - \rho^{(0)}_{jj'}\right),\end{aligned} \tag{1.44}$$

where we have applied the orthonormality condition for the states $\sum_j a^*_{jl}a_{jl'} = \delta_{ll'}$ and also the inverse transformation of the density matrix from the site to the state representation $\rho_{jj'} = \sum_{ll'} a^*_{jl}a_{j'l'}\rho_{ll'}$. Now, inserting (1.40) into (1.44) and canceling out the terms with the same $\mathrm{e}^{-\mathrm{i}s\omega t}$, we find

$$\rho^{(ns)}_{jj'} = -\frac{e}{\hbar}\sum_{l,l'}\frac{\left(\phi^{(ns)}_l - \phi^{(ns)}_{l'}\right)a^*_{jl}a_{j'l'}}{s\omega + \mathrm{i}\gamma - (\varepsilon_j - \varepsilon_{j'})}\rho^{(0)}_{ll'} + \eta^{(ns)}_{jj'}, \tag{1.45}$$

where

$$\eta^{(ns)}_{jj'} = -\frac{e}{\hbar}\sum_{n'=1}^{n-1}\sum_{s'=-n'}^{n'}\sum_{l,l'}\frac{\left(\phi^{(ns)}_l - \phi^{(ns)}_{l'}\right)a^*_{jl}a_{j'l'}}{s\omega + \mathrm{i}\gamma - (\varepsilon_j - \varepsilon_{j'})}\rho^{(n-n'\ s-s')}_{ll'}, \tag{1.46}$$

and

$$\phi^{(ns)}_l = \phi^{\mathrm{ext}}_l\delta_{n,1}(\delta_{s,-1} - \delta_{s,1}) - 2e\sum_{l'}v_{ll'}\rho^{(ns)}_{l'l'}, \tag{1.47}$$

which is the contribution to the harmonic s of the total potential at order n. By using the identity $\rho^{(0)}_{ll'} = \sum_{jj'} a_{jl} a^*_{j'l'} \rho^{(0)}_{jj'} = \sum_j a_{jl} a^*_{j'l'} f_j$ and changing to the site representation we find the self-consistent expression for the diagonal elements of the density matrix to be

$$\rho^{(ns)}_{ll} = -\frac{1}{2e} \sum_{l'} \chi^{(s)}_{0,ll'} \phi^{(ns)}_{l'} + \sum_{jj'} a_{jl} a^*_{j'l} \eta^{(ns)}_{jj'}, \tag{1.48}$$

where

$$\chi^{(s)}_{0,ll'} = \frac{2e^2}{\hbar} \sum_{jj'} (f_{j'} - f_j) \frac{a_{jl} a^*_{jl'} a^*_{j'l} a_{j'l'}}{s\omega - (\varepsilon_j - \varepsilon_{j'}) + \mathrm{i}\gamma}, \tag{1.49}$$

that is the non-interaction susceptibility at frequency $s\omega$. Finally, the nonlinear induced charge is calculated by $\rho^{(ns)}_{l,\mathrm{ind}} = -2e\rho^{(ns)}_{ll}$ which leads us to write the nonlinear polarizability as

$$\alpha^{(n)}_{s\omega} = -\frac{2e}{(E_0)^s} \sum_l \rho^{(ns)}_{ll} \mathbf{R}_l \cdot \hat{\mathbf{e}}, \tag{1.50}$$

where $\hat{\mathbf{e}}$ points in the direction of the incident E-field.

1.2.7 Interactions with electron beams

As discussed before, SPs are difficult to excite with external light as a result of the momentum mismatch and hence, new methods are required to generate plasmons. Electrons are in general good candidates because their dispersion relation always matches the plasmon momentum.

Let us take as an example a single free electron that interacts with a photon within the no-recoil approximation. The energy and momentum of the electron before the interaction are $(1/2)mv^2$ and $m\mathbf{v}$, respectively, whereas for the photon we have $\hbar\omega$ and $\hbar\mathbf{k}$, respectively. As energy and momentum have to be preserved, $m\mathbf{v}_f = m\mathbf{v} + \hbar\mathbf{k}$ and $(1/2)mv_f^2 = (1/2)mv^2 + \hbar\omega$. By solving this system of equations we find that $\omega = \mathbf{k} \cdot \mathbf{v} + \hbar k^2/2m$ which

for $\hbar\omega \ll 1$ MeV, is approximately $\omega \approx \mathbf{k}\cdot\mathbf{v}$. Thus, electrons have indeed less momentum than light and can interact with evanescent light fields such as SPs.

We can quantify this interaction by means of energy-loss decay rates Γ that basically account for the energy that an electron, or a beam of electrons, loses when it interacts with a system in which an induced field is triggered that acts back on the electron and somehow affects its trajectory and final energy. By measuring these energy losses we are able to map the type of phenomena that the electron beam has excited.[49] This technique is called *electron energy-loss spectroscopy* (EELS).

From a quantum mechanical perspective, the decay rate of an electron with energy $\hbar\varepsilon_i$ in the electron state $|\varphi_i\rangle = \sum_l a_{il}|l\rangle$ that undergoes a transition to a state $|\varphi_f\rangle = \sum_l a_{fl}|l\rangle$ with energy $\hbar\varepsilon_f$ when it interacts with a system (target) described through its density matrix ρ and that goes from state $|\psi_{j'}\rangle$ of energy $\hbar\omega_{j'}$ to state $|\psi_j\rangle$ with energy $\hbar\omega_j$, is given to first order by Fermi's golden rule[47,49]

$$\Gamma_{ll'} = \frac{2\pi e^4}{\hbar}\sum_{fi}\sum_{jj'} a_{fl}a^*_{fl'}a^*_{il}a_{il'}|\rho^{(1)}_{jj'}v_{ll'}|^2\delta(\varepsilon_f-\varepsilon_i+\omega_j-\omega_{j'})\,[1-f_f]\;f_i, \tag{1.51}$$

where $f_{f|i} = \{1+\exp[(\hbar\varepsilon_{f|i}-E_{\mathrm{F}f|i})/k_BT]\}^{-1}$ are the Fermi-Dirac distributions for the electrons in the target.

Following ref. 50 we find a relation between the density matrix of the target and the screened Coulomb interaction, which is often more convenient and easier to calculate

$$\mathrm{Im}\,\{W_{ll'}\} = -\frac{\pi e^2}{\hbar}\sum_{jj'}|\rho^{(1)}_{jj'}v_{ll'}|^2\,\delta(\omega_j-\omega_{j'}-\omega), \tag{1.52}$$

where ω is the transferred frequency. Hence, eq. (1.51) can be spectrally re-

solved through $\Gamma = \int_0^\infty d\omega \Gamma(\omega)$ with

$$\Gamma_{ll'}(\omega) = \frac{2e^2}{\hbar} \sum_{fi} a_{fl} a^*_{fl'} a^*_{il} a_{il'} \, \mathrm{Im}\left\{-W_{ll'}\right\} \, \delta(\varepsilon_f - \varepsilon_i + \omega) \left[1 - f_f\right] \, f_i. \tag{1.53}$$

Finally, for completeness, the function version of eq. (1.53) is

$$\begin{aligned}\Gamma(\omega) = & \frac{2e^2}{\hbar} \sum_{fi} \int d^3\mathbf{r} \int d^3\mathbf{r}' \, \varphi_f(\mathbf{r}) \varphi^*_f(\mathbf{r}') \varphi^*_i(\mathbf{r}) \varphi_i(\mathbf{r}') \times \\ & \times \mathrm{Im}\left\{-W(\mathbf{r}, \mathbf{r}', \omega)\right\} \delta(\varepsilon_f - \varepsilon_i + \omega) \left[1 - f_f(\hbar\varepsilon_f)\right] \, f_i(\hbar\varepsilon_i).\end{aligned} \tag{1.54}$$

1.3 The special case of graphene

A material that deserves its own full section in the introduction of this thesis is *graphene*, the monolayer of carbon atoms tightly packed into a honey-comb lattice.[51–55] Graphene was the first two-dimensional (2D) material that was properly isolated and characterized. These findings in 2004[56,57] brought Andre Geim and Konstantin Novosolev the Nobel Prize in Physics in 2010 and opened up the path to a full new area of research on optics and electronics of 2D materials and their corresponding applications.

1.3.1 Electronic properties of graphene

The special properties of graphene come as a result of its band structure. Its direct hexagonal lattice [see Fig. 1.4(a)] lies in the $\mathbf{R} = (x, y)$ plane and is composed of two sublattices A and B that are generated by the 2D vectors $\boldsymbol{a}_1 = (a_C/2)(3, \sqrt{3})$ and $\boldsymbol{a}_2 = (a_C/2)(3, -\sqrt{3})$, where $a_C = 1.421$ Å is the carbon-carbon atomic distance. These carbon atoms remain together in the (x, y) plane thanks to strong σ-bonds whereas in the out-of-plane (z) direction

the $2p_z$ orbitals of the carbon atoms hybridize to form π-bonds. These π-bonds make graphene sheets stack together (or to other 2D materials) via van der Waals forces in an A on top of B configuration.

The associated reciprocal lattice [see Fig. 1.4(b)] is spanned by the vectors $\boldsymbol{b}_1 = (2\pi/3a_{\mathrm{C}})(1, \sqrt{3})$ and $\boldsymbol{b}_2 = (2\pi/3a_{\mathrm{C}})(1, -\sqrt{3})$, albeit probably the reciprocal vectors with more importance regarding the electronic properties of graphene are the high-symmetry points $\mathbf{K} = (2\pi/3a_{\mathrm{C}})(1, 1/\sqrt{3})$ and $\mathbf{K}' = (2\pi/3a_{\mathrm{C}})(1, -1/\sqrt{3})$, which are also called Dirac points [see Fig. 1.4(d)] for reasons that we shall see below.

We can retrieve the band structure of graphene by applying a TB Hamiltonian (1.7) to nearest neighbors with a phenomenological hopping parameter $t = -2.8\,\mathrm{eV}$.[58] After some algebra we find[59]

$$E_{\pm}(\mathbf{k}) = \pm|t|\sqrt{3 + f(k_x, k_y)} \tag{1.55}$$
$$f(\mathbf{k}) = 2\cos(\sqrt{3}k_y a_{\mathrm{C}}) + 4\cos\left(\frac{\sqrt{3}}{2}k_y a_{\mathrm{C}}\right)\cos\left(\frac{3}{2}k_x a_{\mathrm{C}}\right),$$

where the $+$ is for the upper band (also called π^* band) whereas the $-$ is for the lower one (or π band) and $\mathbf{k} = (k_x, k_y)$ is the momentum vector. These bands are plotted in Fig. 1.4(c).

Now, if we define $\mathbf{k} = \mathbf{K} + \mathbf{Q}$ and expand up to first order the band structure around the K point, assuming $Q \ll K$, we have $E_{\pm}(Q) \approx \pm\hbar v_{\mathrm{F}} Q$, where $v_{\mathrm{F}} = 3ta_{\mathrm{C}}/2\hbar \approx c/300$ is the Fermi velocity of graphene. In consequence, the bands are conical under ~ 3 eV [see Fig. 1.4(d)] and consequently, the effective mass of these electrons is zero near the K point. This is the reason why electrons in graphene are said to be massless and must be described through the Dirac equation.

Lastly, when solving the 2D Dirac equation we find that the wave function (actually a spinor as a result of the two sublattices) associated to the momen-

tum $\mathbf{Q}$ around the K point is

$$\varphi(\mathbf{R}) = \frac{1}{\sqrt{2A}} \mathrm{e}^{\mathrm{i}\mathbf{Q}\cdot\mathbf{R}} \begin{pmatrix} \mathrm{e}^{-\mathrm{i}\phi/2} \\ \pm \mathrm{e}^{\mathrm{i}\phi/2} \end{pmatrix}, \tag{1.56}$$

where A is the area of the graphene sheet, the $+$ is for electrons, the $-$ for holes and ϕ is the azimuthal angle between $\mathbf{Q}$ and $\mathbf{K}$.

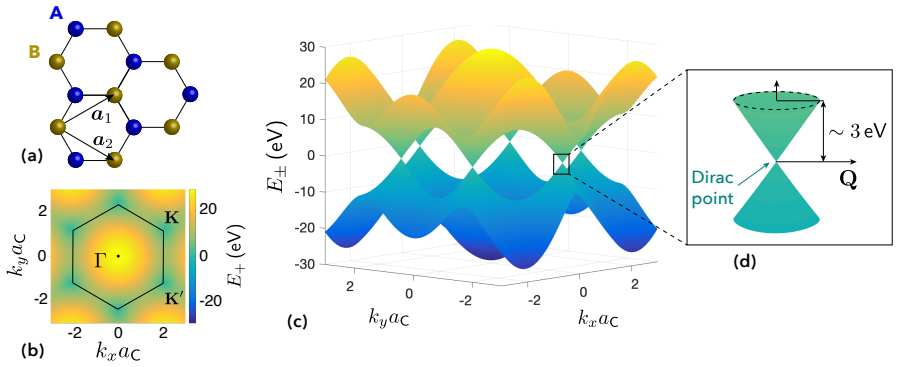

Figure 1.4: **Lattices and band structure of graphene. (a)** *Direct lattice.* **(b)** *Reciprocal lattice.* **(c)** *Band structure of graphene.* **(d)** *Conical bands close to the Dirac points.*

As reported in Tab. 1.1, electrons in the two valleys ($\mathbf{K}$ and $\mathbf{K}'$) in the reciprocal space occupy disks of area $\pi {k_\mathrm{F}}^2$ and hence, the density of electrons is $n = {k_\mathrm{F}}^2/\pi$ with $k_\mathrm{F} = E_\mathrm{F}/\hbar v_\mathrm{F}$ being the Fermi wave vector of graphene. This square root dependence of n on k_F indicates that, under small variations of additional free charge carriers, graphene can be easily turned from a zero band gap semiconductor into a conductor. A property that, as we will see below, makes plasmons in graphene be electrically tunable.

1.3.2 Plasmons in graphene

In extended graphene, we can find the plasmon dispersion of SPs in a way analogous to that of sec. 1.2.3. Let us consider the configuration shown in

Fig. 1.5(a). Here the boundary conditions become

$$E_{x2} - E_{x1} = 0,$$
$$\epsilon_2 E_{z2} - \epsilon_1 E_{z1} = 4\pi\rho_s = 4\pi(-\mathrm{i}/\omega)\nabla_{\mathbf{R}} \cdot (\sigma\mathbf{E}) = \frac{4\pi\sigma}{\omega}\, k_{\|} E_{x1}.$$

By replacing the E-fields by the corresponding governing equations (1.27) we find the plasmon dispersion relation

$$\frac{\epsilon_2}{k_{z2}} + \frac{\epsilon_1}{k_{z1}} + \frac{4\pi\mathrm{i}\sigma}{\omega} = 0. \tag{1.57}$$

This method is basically equivalent to finding the dispersion relation by calculating the poles of the effective reflection coefficient for TM modes for the configuration in Fig. 1.5(a)

$$r_p = \frac{\epsilon_2 k_{z1} - \epsilon_1 k_{z2} + \frac{4\pi\mathrm{i}\sigma}{\omega} k_{z1} k_{z2}}{\epsilon_2 k_{z1} + \epsilon_1 k_{z2} + \frac{4\pi\mathrm{i}\sigma}{\omega} k_{z1} k_{z2}}, \tag{1.58}$$

which in the electrostatic limit ($c \to \infty$ and thus, $k_{z1} = k_{z2} = k_{\|}$) and for symmetric environments ($\epsilon_1 = \epsilon_2 = \epsilon$) reduces to

$$r_p = \frac{1}{1 - \frac{\mathrm{i}\epsilon\omega}{2\pi k_{\|}\sigma}}. \tag{1.59}$$

From these equations, we see that it is indeed the conductivity of graphene what determines its optical response. Generally, we can compute this conductivity in the framework of linear response theory within the RPA via Kubo's formula,[39,53,60,61] which in the local limit (neglecting the spatial dispersion, $k_{\|} \to 0$) can be divided into two contributions, one for intraband transitions and the other for the interband ones, $\sigma = \sigma_{\mathrm{intra}} + \sigma_{\mathrm{inter}}$, that at $T = 0\,\mathrm{K}$ (or

at least for $E_{\mathrm{F}} \gg k_B T$) are[39,53]

$$\sigma_{\mathrm{intra}}(\omega) = \frac{e^2}{\pi\hbar^2}\frac{\mathrm{i}E_{\mathrm{F}}}{\omega + \mathrm{i}\gamma}, \tag{1.60}$$

$$\sigma_{\mathrm{inter}}(\omega) = \frac{e^2}{4\hbar}\left[\Theta\left(\hbar\omega - 2E_{\mathrm{F}}\right) + \frac{\mathrm{i}}{\pi}\ln\left|\frac{\hbar\omega - 2E_{\mathrm{F}}}{\hbar\omega + 2E_{\mathrm{F}}}\right|\right]. \tag{1.61}$$

For energies $\hbar\omega < 2E_{\mathrm{F}}$ the interband contribution to the conductivity (1.61) is negligible as a consequence of Pauli blocking. Hence, for terahertz and mid-infrared frequencies the intraband conductivity dominates even at room temperature. Additionally, eq. (1.60) is often called the Drude conductivity of graphene.

For the sake of comparison, in Fig. 1.5(b) we plot the plasmon dispersion relation for a graphene sheet embedded in air and doped to $E_{\mathrm{F}} = 0.5$ eV, from the poles of (1.59) for both a Drude conductivity without losses ($\gamma = 0$) and a conductivity in the RPA. The redshift of the latter with respect to the former is due to the attractive polarization associated with interband transitions.

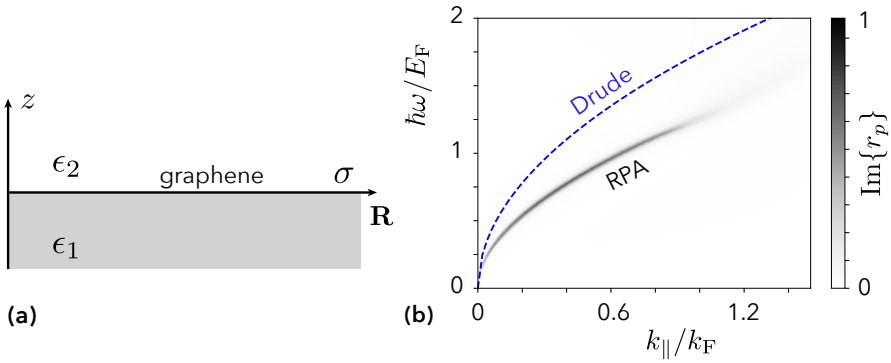

Figure 1.5: **Dispersion relation for SPs in graphene. (a)** *Configuration for a graphene sheet lying on an interface between two materials with permittivities ϵ_1 and ϵ_2.* **(b)** *Dispersion relation for SPs in extended graphene doped to $E_{\mathrm{F}} = 0.5$ eV, embedded on air in the electrostatic limit [from the poles of (1.59)] for a loss-less Drude conductivity (blue dashes) and a conductivity within the RPA (black contour).*

2

Optical properties of finite carbon nanotubes

See the rays of light dance in hurricanes

– Epica

We study the potential of highly-doped finite carbon nanotubes to serve as plasmonic elements that mediate the interaction between quantum emitters. Similar to graphene, nanotubes support intense plasmons that can be modulated by varying their level of electrical doping. These excitations exhibit large interaction with light and electron beams, as revealed upon examination of the corresponding light extinction cross-section and electron energy-loss spectra. We show that quantum emitters experience record-high Purcell factors, while they undergo strong mutual interaction mediated by their coupling to the tube plasmons. Our results show the potential of doped finite nanotubes as tunable plasmonic materials for quantum optics applications.

2.1 Introduction

Plasmons, the collective oscillations of electrons in conducting media, have generated great expectations due to their ability to manipulate optical fields on deep subwavelength scales, thus enabling exciting possibilities for future nanophotonic devices. Traditionally, plasmons have been studied in noble metal nanostructures, where their resonance frequencies and optical coupling strengths are determined by the material intrinsic properties, the morphology of the structure, and the dielectric environment.[62–64] Graphene, the atomically thin carbon layer, has emerged as a promising alternative to noble metals for nanoplasmonic applications due to its ability to support electrically tunable plasmon resonances that interact strongly with light.[51,55,65,66] The appealing properties of graphene plasmons are now inspiring research on other two-dimensional van der Waals materials,[67,68] as well as on carbon-based molecules.[69,70] Currently explored applications of plasmons, including sensing,[71–74] photodetection,[75–78] wave guiding,[79,80] photovoltaics,[81] and medicine,[82] could benefit from the identification of new types of actively tunable plasmonic materials with lower inelastic losses.

In a related context, significant advances in quantum information have been gained through the study of coupling between quantum emitters (QEs) and surface plasmons (SPs) supported by noble metals[83–86] or graphitic nanostructures.[39,87] In particular, carbon nanotubes (CNTs), which are 1D carbon structures formed upon cylindrical wrapping of a graphene sheet, could serve as conduits in plasmonic circuits,[88] while their plasmons have been predicted to undergo ultra-efficient coupling with QEs.[89–93] Although numerous studies on the appealing structural, electrical, and optical properties of CNTs indicate their suitability as components in nanophotonic devices,[88,92,94,95] the tunable, low-energy plasmons supported by these structures when they are doped are only now beginning to be explored.[55,95,96]

In this chapter, we investigate the optical response associated with the plasmons of highly-doped finite CNTs, described either by classical electrodynamic or quantum-mechanical (QM) simulations, and discuss their potential ability to mediate quantum optical interactions on the nanoscale. While plasmons in large-scale graphene nanostructures are currently limited to mid-infrared and lower frequencies, a reduction in their size to the limit represented by polycyclic aromatic hydrocarbons (PAH) can blue-shift resonances toward the visible regime.[69,70] We envision finite CNTs as an intermediate situation between large-scale graphitic structures and PAH molecules, and therefore as good candidates to extend the robustness and tunability of graphene plasmons toward the visible and near-infrared parts of the spectrum. We also demonstrate that plasmons in finite CNTs can interact strongly with a neighboring QE, while interactions between emitters can be enhanced when they are mediated by 1D plasmons.

2.2 Plasmons in doped carbon nanotubes

We first adopt a classical electromagnetic description of doped CNTs by treating them as rolled-up sheets of thickness t and diameter D, taking their surface conductivity as that of extended graphene. We describe the level of doping through the change in Fermi energy E_{F} relative to the neutrality point. Then by studying the linear optical response while moving toward the $t \to 0$ limit, we observe converged resonances for $t \sim 0.3\,\mathrm{nm}$, which is similar to the interlayer separation of graphite. For finite CNTs of length L larger than the Fermi wavelength $\lambda_{\mathrm{F}} = 2\pi\hbar v_{\mathrm{F}}/E_{\mathrm{F}}$ (*e.g.*, $\lambda_{\mathrm{F}} \sim 4\,\mathrm{nm}$ for $E_{\mathrm{F}} = 1\,\mathrm{eV}$), the conductivity can be approximated in the local limit. In particular, starting from the random-phase approximation (RPA),[50] we reach the so-called local-RPA surface conductivity, which reduces to the Drude model $\sigma(\omega) =$

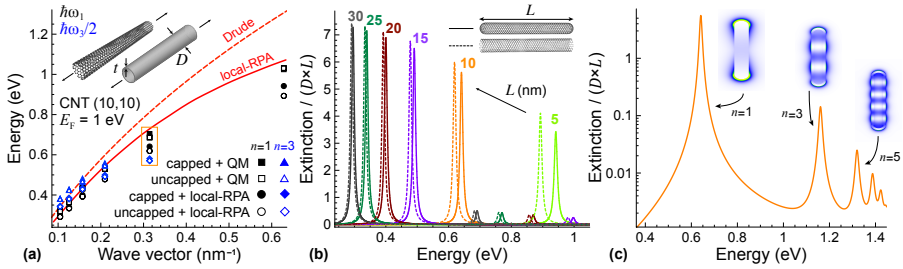

Figure 2.1: **Plasmon dispersion relation in a CNT. (a)** *Comparison of the plasmon dispersion relation for finite and infinite single-wall CNTs. We describe the tubes classically by assuming that the wall responds with the same local 2D surface conductivity σ as graphene. Two different models for σ are considered (Drude and local-RPA, see labels). The (10,10) CNTs under consideration have a small diameter ~ 1.35 nm that only allows the efficient excitation of axially symmetric modes. The plasmon dispersion for infinite tubes is obtained from eq. (2.1) (curves). We consider capped and uncapped finite tubes of length L, which display modes of different order n dominated by a wave vector $n\pi/L$ (symbols).* **(b)** *Extinction cross-section for capped (solid curves) and uncapped (dashes curves) CNTs described with the local-RPA conductivity.* **(c)** *Overview of the extinction spectrum for the $L = 10$ nm CNT, along with near-field plots for the different plasmon modes. The Fermi energy is 1 eV and the damping is 10 meV in all cases.*

$\mathrm{i}e^2 E_\mathrm{F}/\pi\hbar^2(\omega + \mathrm{i}\tau^{-1})$ for photon energies smaller than $2E_\mathrm{F}$ (*i.e.*, below the threshold for interband transitions).

For simplicity, we concentrate on (10,10) armchair nanotubes (diameter $D = 1.35$ nm) and limit our study to the axially symmetric modes (azimuthal number $m = 0$), as higher-order plasmons are too tightly confined, and therefore, we expect them to have a weak interaction with incident light and QEs. As a reference, we first simulate CNTs of infinite length, whose plasmon bands are determined by the poles of their reflection coefficient toward cylindrical waves,[93] which yield the dispersion relation

$$\frac{\omega}{\sigma(\omega)} = -4\pi\mathrm{i}k_\parallel^2 a I_0(k_\parallel a) K_0(k_\parallel a). \tag{2.1}$$

Here $a = D/2$ is the tube radius and I_0 (K_0) is the modified Bessel function of the first (second) kind. We plot in Fig. 2.1(a) the resulting $m = 0$ band, assuming either the Drude model or the local-RPA conductivity. The latter is observed to be redshifted relative to the former, presumably as a result of attractive polarization associated with virtual interband transitions.

In finite CNTs, the plasmon modes can be understood as Fabry-Perot (FP) resonances involving successive reflections at the tube edges. We investigate finite tubes by taking the incident electric field along the symmetry axis and simulating their classical electromagnetic response using the boundary-element method.[97] The resulting extinction spectra are shown in Fig. 2.1(b), as obtained by using the local-RPA conductivity as obtained by using the local-RPA for either capped (solid curves) or uncapped (broken curves) CNTs of different lengths. As expected from the FP character of the plasmon resonances, the mode frequencies are observed to decrease with increasing length. Additionally, the spectral widths are inherited from the phenomenological lifetime $\tau \approx 66$ fs (*i.e.*, $\hbar\tau^{-1} = 10$ meV) that we incorporate in the conductivity, as radiative losses are negligibly small because L is much smaller than the light

wavelength. As the external field is polarized along the tube axes, only odd-order modes are excited. This is clearly illustrated in Fig. 2.1(c), which shows an overview of the extinction spectrum of the $L = 10$ nm tube for a wide frequency range, where multiple resonances are observed, labeled by the number of nodes in their near-electric-field intensity distributions, $n = 1, 3, \ldots$ [see insets to Fig. 2.1(c)]. The reduction in the maximum cross-section associated with each of the resonances for increasing n is understood from the sign cancellations occurring in their respective induced charges. Noticing that the mode intensity appears to have a maximum at the tube edges, we can approximate the reflection of an $m = 0$ plasmon propagating along the tube as 1 (*i.e.*, neglecting losses and assuming zero phase change). Then, the plasmon parallel wave-vector $k_{\parallel}$ must satisfy the condition $k_{\parallel} = n\pi/L$ in the FP model. The resulting combinations of mode energy and $k_{\parallel}$ observed for different n's with various tube lengths are represented in Fig. 2.1(a), in good agreement with the plasmon dispersion relation of the infinite tube, thus corroborating the validity of the FP model to qualitatively understand these plasmons.

We now compare these results with those obtained from a QM simulation of the CNTs. Specifically, we use linear response theory within the RPA using electronic states described by a nearest-neighbors tight-binding model with the same parameters as in previous studies of graphene[58,59,98] (*i.e.*, a single p orbital per carbon site with a hopping energy of 2.8 eV). As shown in Fig. 2.1(a), the obtained results are similar to those of the classical description, including the frequency increase associated with larger wave vectors (*i.e.*, smaller L), as well as the blue shift in the plasmons of capped tubes compared with uncapped tubes. However, the QM model predicts slightly higher-energy plasmons, presumably as a result of quantum confinement, in agreement with previous results for graphene nanodisks.[98]

We quantify the strength of the modes by the area of the plasmon features in the extinction spectrum through the f-sum rule, $\int_0^\infty d\omega\, \sigma^{\rm ext}(\omega) =$

$2\pi^2 e^2 N_e/(m_e^* c)$.[99] Typically, in either classical or QM simulations, we observe that the first mode carries most of the spectral weight (over 80%), except for the smallest CNT considered (length $L = 5$ nm), in which the first mode takes $\sim 65\%$ of the total area.

As we work in the nonretarded regime, we construct the optical response for CNTs from the electrostatic potential. This allows us to perform an expansion in the eigen-modes of the electric field,[55] from which we find a scaling law for the polarizability by designating the diameter D as the characteristic size of a CNT:

$$\alpha(\omega) = D^3 \sum_j \frac{A_j}{\frac{1}{\eta} - \frac{1}{\eta_j}} \,. \tag{2.2}$$

In the above expression, $\eta = \mathrm{i}\sigma(\omega)/\omega D$, while A_j and η_j are size- and material-independent fitting parameters which follow the sum rules $\sum_j A_j = A/D^2$ and $-\sum_j \eta_j A_j = \alpha_0/D^3$, where $A = LD$ is the cross-sectional area of the tube and α_0 is the polarizability of a perfect-conductor cylinder with the same shape as the CNT (*i.e.*, length L and diameter D). Through the optical theorem $\sigma^{\mathrm{ext}}(\omega) = 4\pi(\omega/c)\mathrm{Im}\{\alpha(\omega)\}$, we find an expression to fit the resonances shown in Fig. 2.1(b), from which we obtain values for A_j and η_j as a function of both thickness and length (see Fig. 2.2).

2.3 Interaction with focused electron beams

We now shift our attention to the interaction of CNT plasmons with energetic electrons as a means to investigate their spatial and spectral characteristics. Indeed, many of the properties of plasmons have been revealed by electron-microscope spectroscopies,[49] which are better suited than optics-based methods to probe these deep-subwavelength excitations. In particular, electron energy-loss spectroscopy (EELS) appears to be an ideal technique to

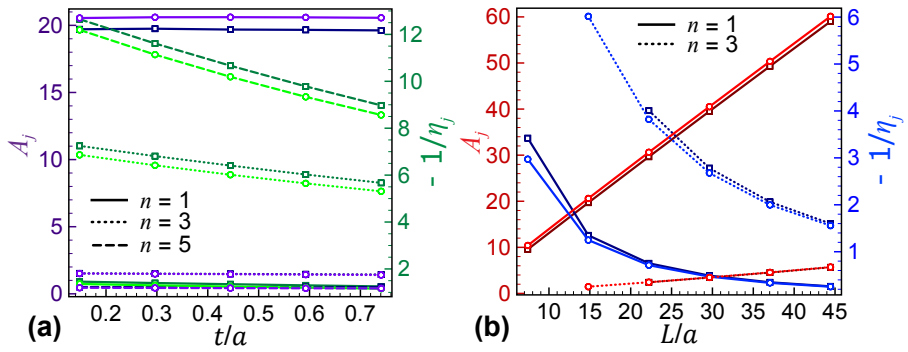

Figure 2.2: **Scaling law parameters**. **(a)** *CNT-thickness dependence of the scaling law parameters* (2.2). *Dark (light) colors with squares (circles) correspond to capped (uncapped) CNTs.* **(b)** *CNT-length dependence.*

study the strongly confined plasmons of CNTs. We thus present in Fig. 2.3 results for 10 keV electrons passing near a CNT along the two trajectories shown in the insets. We find that different plasmon modes are excited with different strength, also depending on the orientation of the trajectory. For example, high-order modes (*i.e.*, above the energy range shown in Fig. 2.3) are more easily excited in the trajectory that runs parallel to the tube, while the perpendicular trajectory is more efficient at exciting the lowest-order ~ 0.65 eV mode. In particular, the dipolar plasmon has its field concentrated near the tube ends, thus favoring the interaction with the perpendicular trajectory under consideration.

Our choice of a 1 nm beam-CNT separation is not critical, as we find the EELS probability for excitation of the dipolar plasmon to decay exponentially with a characteristic distance $\sim L/2\pi$ (see Fig. 2.4). This result can be understood as follows: from the above FP model, the plasmon wave vector must be $\sim \pi/L$ along the tube; as the plasmon evolves in the quasistatic limit, its wave vector along the perpendicular direction must be $\sim \mathrm{i}\pi/L$; consequently, we find a dependence $\propto \exp(-2\pi x/L)$ of the electric-field intensity associated

with the plasmon on the distance to the tube x, which is directly inherited by the EELS probability. In general, plasmons of order n should decay with a characteristic transversal distance $\sim L/2\pi n$.

Remarkably, the peak probability reaches high values, comparable to or larger than those typically encountered in EELS studies of larger metal nanoparticles. We find that the number of plasmons excited per electron (*i.e.*, the integrated peak area, which should be roughly independent of τ) can reach 0.1%, although this number scales as $\sim 1/v^2$ with electron velocity v for small objects (*cf.* $v/c = 0.19$ for the 10 keV electrons here considered and $v/c = 0.55$ for 100 keV).

2.4 Interaction with quantum emitters

Light can be confined to extremely small regions of space through the excitation of localized surface plasmons, thus presenting an opportunity to achieve strong coupling between a QE and optical fields. Here we assess the strength of a QE coupling to the local electromagnetic fields of CNT plasmons through quantitative analysis of the enhancement in its radiative decay rate. In what follows, we represent a QE as a two-level system characterized by its transition dipole moment $\mathbf{d}$. If a single QE is placed in close proximity to a CNT, it induces a field $\mathbf{E}^{\text{ind}}$ from the CNT that acts back on the emitter, thereby modifying its decay rate according to[29]

$$\Gamma_{11}(\omega) = \Gamma_0(\omega) + \frac{2}{\hbar}\text{Im}\{\mathbf{d}^* \cdot \mathbf{E}^{\text{ind}}\} \,, \tag{2.3}$$

where $\Gamma_0(\omega) = 4\omega^3|\mathbf{d}|^2/3\hbar c^3$ is the decay rate in free space. If we now consider two such QEs that are placed at opposite ends of the CNT (see inset to Fig. 2.5), we can quantify their interaction mediated by the CNT by studying the radiative decay rate enhancement of the first QE (*e.g.*, the QE at position

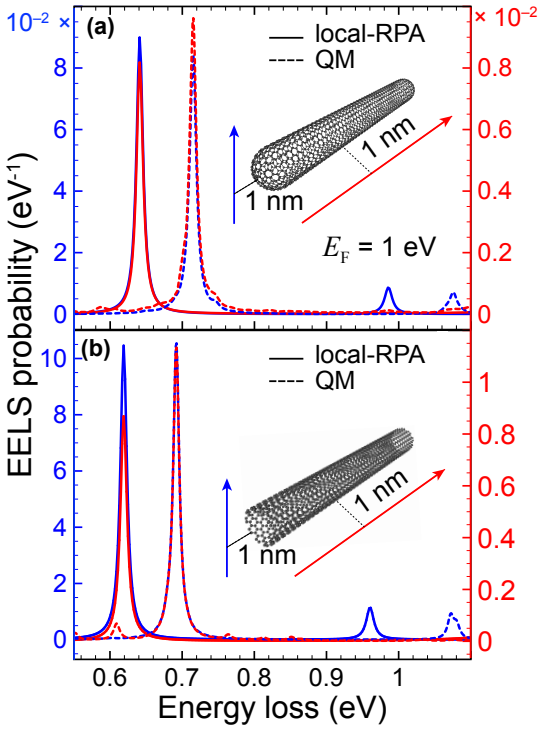

Figure 2.3: **Plasmon excitation with electron beams. (a)** *Electron energy-loss probability for a 10 keV electron passing near a $L = 10$ nm capped (10,10) CNT along two different trajectories (see inset). Classical local-RPA calculations (solid curves) are compared with quantum RPA simulations (broken curves).* **(b)** *Same as (a) for an uncapped tube.*

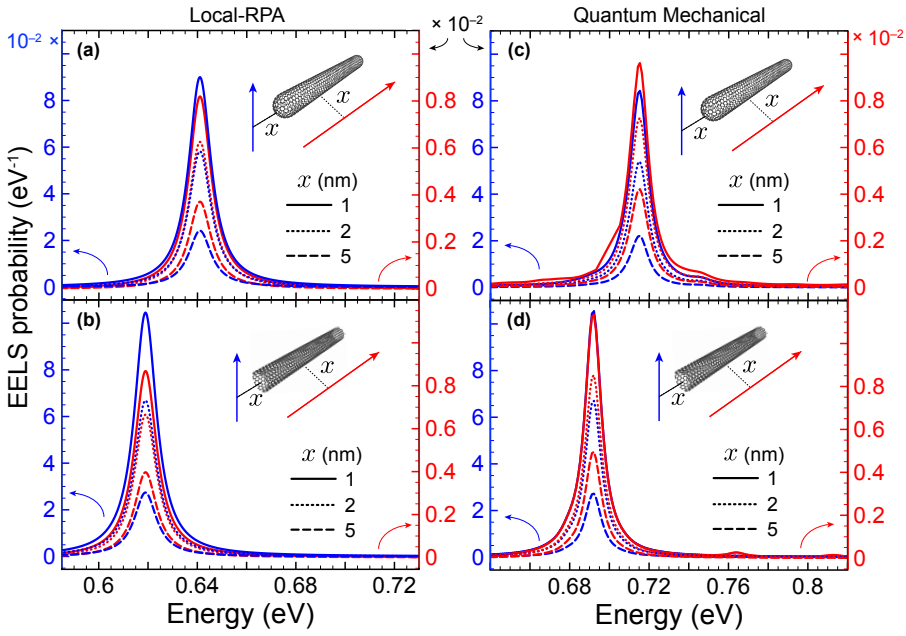

Figure 2.4: **Dependence of the EELS probability on electron-beam-CNT distance.** *We show classical local-RPA (left panels) and quantum-mechanical (right panels, tight binding plus RPA) calculations of the EELS probability under the same conditions as in Fig. 2.3 with different electron-beam-CNT separations for capped (upper panels) and uncapped (lower panels) CNTs.*

1) due to the induced electric field $\mathbf{E}_{12}$ produced on it by the second QE (*e.g.*, the QE at position 2) as[100]

$$\Gamma_{12}(\omega) = \frac{2}{\hbar}\mathrm{Im}\{\mathbf{d}_1^* \cdot \mathbf{E}_{12}\} \ . \tag{2.4}$$

We remark that under the conditions considered here our results indicate that the natural decay rate Γ_0 is much smaller than the enhanced decay rate (see below). Then, assuming for simplicity that the QEs are identical, the symmetry of the CNT and its plasmon modes allows us to approximate $\Gamma_{11} \simeq \Gamma_{12}$ when the QEs are placed on opposite ends of the carbon structure.

In Fig. 2.5(a) we show Γ_{ij}/Γ_0 ($i, j = 1, 2$) for two QEs, each located at a distance of one nanometer from either ends of a 10 nm-long (10,10) CNT (red curves correspond to uncapped CNTs and black curves to capped CNTs). Remarkably, we observe an enhancement of the order of $\sim 10^8$, which is several orders of magnitude higher than predicted for graphene disks.[101] This strong interaction is a consequence of the fact that the emitter decays with close to unity probability into the CNT plasmon (instead of into other inelastic decay channels such as electron-hole pairs), even when placed at such a short distance from the tube, as previously shown for extended CNTs.[93] Additionally, these results do not depend critically on the exact positioning of the QEs: we expect their interaction to roughly scale with the product of the plasmon field amplitudes at the position of the emitters; this amplitude decays exponentially over a distance of several nanometers (see the above discussion on the distance dependence of the EELS probability). This intuition is corroborated by Fig. 2.6.

Now, invoking the Jaynes-Cummings model,[102] such high Purcell factors should enable quantum entanglement between the emitters,[103,104] as well as the implementation of logical gates,[85] thus providing further motivation for the application of doped CNTs in nanoscale quantum devices.

Additionally, the real part of the interaction between the QE and the in-

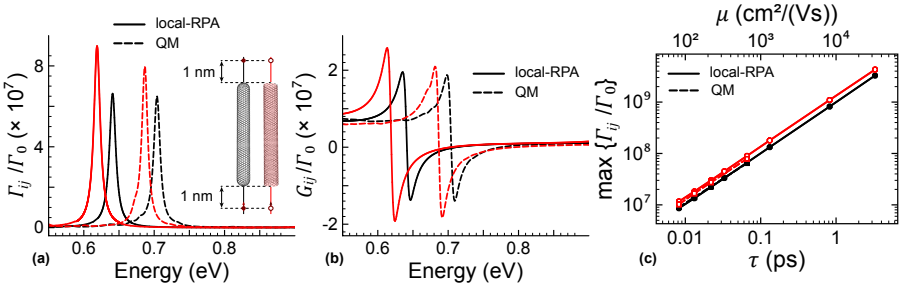

Figure 2.5: **Interaction with quantum emitters. (a,b)** *Emission-energy dependence of the imaginary (a) and real (b) parts of the QE interactions, normalized to the free-space emission rate Γ_0. We consider identical, axially polarized QEs placed 1 nm away from the surface of a 10-nm-long (10,10) CNT with either capped (black) and uncapped (red) ends. The Purcell factor Γ_{jj}/Γ_0 cannot be separated from the interemitter interaction Γ_{12}/Γ_0 on the scale of the plot. We compare classical local-RPA (solid curves) and quantum RPA (broken curves) calculations for a Fermi energy of 1 eV and a damping of 10 meV.* **(b)** *Dependence of the interemitter interaction on the plasmon relaxation time τ. Solid black (open red) symbols account for maxima of the Purcell factor given by a capped (uncapped) CNT. Classical local-RPA (quantum-mechanical) calculations correspond to the circles (squares). The equivalent mobility $\mu = \tau e v_{\mathrm{F}}^2/E_{\mathrm{F}}$ within the Drude model is shown in the upper horizontal scale.*

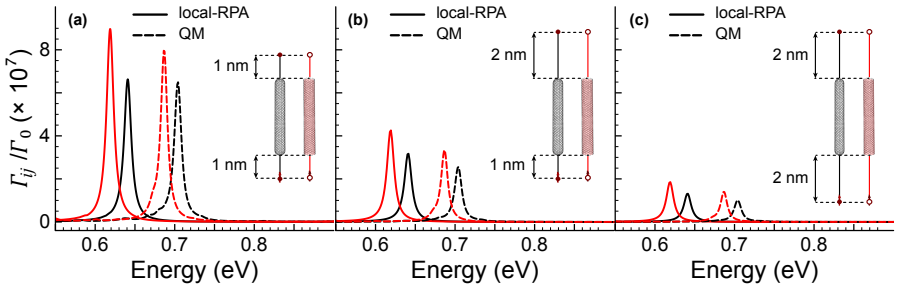

Figure 2.6: **Distance dependence of the interaction with QEs.** *We compare the coupling coefficients shown in Fig. 2.5(a), and reproduced in panel (a) of this figure for convenience, with those obtained by moving the QEs away from the tube ends, either in asymmetric (b) or symmetric (c) configurations.*

duced field of the CNT yields the energy splitting of the QE states [Fig. 2.5(b)], which is quantified by

$$G_{ij}(\omega) = \frac{1}{\hbar}\mathrm{Re}\{\mathbf{d}_i^* \cdot \mathbf{E}_{ij}\} \ , \tag{2.5}$$

where $i, j = 1, 2$ indicate the QE positions. This interaction is a few times lower in magnitude than Γ_{ij}, therefore indicating that one could reach a regime in which the decay rate of fast emitters (GHz) is made close to their optical frequency (PHz), with a small fractional correction in emission frequency.

Figure 2.5(c) shows the dependence of the Purcell factor on the electron mobility, which enters both the classical and QM models through the phenomenological relaxation rate τ. Even for extremely low plasmon lifetimes τ of the order of ~ 10 fs, doped CNTs are predicted to enable Purcell factors $\sim 10^7$, while we observe a linear dependence of such factors on τ. These results are very similar within both classical and quantum-mechanical models, thus corroborating once more the validity of the former to cope with structures that contain only several thousand atoms.

2.5 Conclusion

We have demonstrated that highly-doped finite CNTs exhibit intense plasmon resonances that can mediate the interaction between quantum emitters placed in their proximity. In particular, CNT plasmons are found to produce optical extinction cross-sections exceeding the CNT projected areas, with Purcell factors for proximal quantum emitters reaching $\sim 10^8$, enabling strong interaction between emitters located at opposite ends of a CNT. These plasmons lie in the near-infrared part of the spectrum for realistic tube dimensions, thus holding potential for their use in technological applications within that frequency range. We introduce a classical electromagnetic description of the CNT optical response that predicts plasmon energies and coupling strengths in good agreement with those obtained from an atomistic model (tight-binding description of the electronic states combined with RPA linear response) both in the case of capped and uncapped CNTs. Our results indicate a strong potential for highly-doped CNTs as robust, actively tunable plasmonic elements that are well-suited for nanophotonic and quantum-optics applications.

3

Strong-field-driven dynamics and high harmonic generation in 1D systems

`hello, world`
– *Brian Kernighan*

The observation of high-order harmonic generation (HHG) from bulk crystals is stimulating substantial efforts to understand the involved mechanisms and their analogue to the intuitive three-step recollision model of gas phase HHG. On the technological side, efficient solid-state HHG is anticipated to enable compact attosecond and ultraviolet light sources that could unveil electron dynamics in chemical reactions and provide sharper tomographic imaging of molecular orbitals. In this chapter we explore the roles of electronic band structure and Coulomb interactions in solid-state HHG by studying the optical response of linear atomic chains and carbon nanotubes to intense ultrashort pulses. Specifically, we simulate electron dynamics by solving the single-particle density matrix equation of motion in the presence of intense ultrafast optical fields, incorporating tight-binding electronic states and a self-consistent electron-electron interaction. While linear atomic chains constitute an idealized system, our realistic 1D model readily provides insight on

the temporal evolution of electronic states in reciprocal space, both in the absence or presence of electron interactions, which we demonstrate to play an important role in the HHG yield. This model further predicts that doped semiconductors generate high harmonics more efficiently than their metallic counterparts. To complement this idealized system we also show results for HHG in more realistic quasi-1D structures such as carbon nanotubes, the behavior of which is found to be in good qualitative agreement with the atomic chains. Our findings apply directly to extreme nonlinear optical phenomena in atoms on surfaces, carbon-based structures, linear arrays of dopant atoms in semiconductors, and linear molecules, such as polycyclic aromatic hydrocarbon chains, and can be straightforwardly extended to optimize existing platforms for HHG or identify new solid-state alternatives.

3.1 Introduction

High-harmonic generation (HHG) is perhaps the most striking example of a nonlinear optical process and its ability to spectrally and temporally disperse intense laser light.[105,106] Initial reports of HHG from atomic gases[107] revealed a light emission intensity plateau extending over many integer multiples of the fundamental exciting laser frequency and characterized by an abrupt drop at a specific cutoff energy. Concise theoretical explanations of the underlying physics were developed shortly thereafter, culminating in the celebrated three-step model of an atom interacting with a single cycle of an intense impinging optical field: tunnel ionization triggered by the driving electric field liberates an electron from the atom that gains additional kinetic energy as it is driven away from and back towards the parent nucleus, ultimately emitting, upon recollision (through coherent interactions of the electron wave function with itself), light at high harmonic orders of the fundamental frequency.[108–110]

This extreme nonlinear optical phenomenon is a source of coherent high-frequency electromagnetic radiation, which can be processed to produce attosecond optical pulses, thus garnering significant attention as the means to develop micron-scale XUV-light sources[111] (*i.e.*, the equivalent of table-top synchrotrons) and perform quantum logic operations at optical clock rates,[112] while enabling visualization of electronic band structures,[113,114] monitoring electron-hole recollisions in real time,[115] resolving subfemtosecond processes governing chemical reactions,[116] and recording electron dynamics in molecular orbitals.[117,118]

Despite the numerous fascinating advances in science and technology that have resulted from atomic HHG, the expense and delicacy of the associated experimental set-ups renders their use hardly practical outside of specialized laboratory facilities. In contrast, recent observations of HHG from solids[119–121] are establishing new paths for attosecond science and strong-field physics, potentially leading towards XUV and attosecond light sources in compact solid-state devices. While the three-step recollision model[122] offers an intuitive understanding of HHG from atoms in the gas phase, the picture is less clear for solid-state HHG. Early theoretical proposals considered a three-step-like model in which an electron undergoes Bloch oscillations within an electronic band (either valence or conduction after interband tunneling) as a consequence of the change in direction of acceleration after half an optical cycle of the driving electric field;[123–125] subsequently the excited electron scatters within its band (*i.e.*, intraband HHG) or recombines with the parent hole or ion (*i.e.*, interband HHG), and finally, it recollides with the first- and second-nearest holes or ions. However, this simplified description does not explain the role of electron-electron correlations, and furthermore, available experiments and numerical simulations often do not elucidate the specific origin of generated harmonics (*e.g.*, from interband or intraband charge-carrier motion); the generation of even-order harmonics, the existence of atto-chirps, the formation

of a well-defined high-energy cutoff, and numerous aspects of the electronic band structure still remain underexplored in the context of solid-state HHG.[126–129]

Further insight into the aforementioned open questions in HHG from condensed-matter systems can be gathered by analyzing one of the simplest models in solid-state physics: the Su-Schrieffer-Heeger (SSH) chain,[130–132] consisting of a dimerized linear chain of atoms described in the tight-binding approximation, with alternating hopping energies assigned to each of the two neighboring atoms on side of any given atom [Fig. 3.1(a)]. As we discuss below, the SSH model is a convenient system to explore electronic band structure effects in the optical response of materials, as appropriate choices of hopping energies reveal either metallic, insulating, or topologically insulating behavior. To explore the effect of topology on HHG, recent works[133,134] have employed the SSH tight-binding model and its analogue in more rigorous time-dependent density functional theory (TDDFT) simulations of atomic chains, predicting improved harmonic yields associated with the topolotical insulator (TI) phases for sub-band-gap photon energies that are robust under distortions, continuous phase transitions, and choice of on-site potentials.[135] In a related study,[136] the transition from atomic-like systems to solid-state bulk materials was analyzed in the context of HHG, emphasizing the evolution in cutoff energy as the chain length increases, and concluding that a chain of six atoms constitutes the optimal length for this transition to occur as a consequence of changes in the state density.

Seeking to optimize HHG yields in condensed-matter systems, we explore the synergy between electronic band structure and optical resonances in finite SSH chains, which constitute a convenient, computationally inexpensive model that has already been demonstrated to qualitatively describe HHG predicted in the more rigorous TDDFT simulations of related 1D systems.[133,134] We augment the SSH tight-binding Hamiltonian with a term accounting for electron-electron interactions, incorporating a single-electron density matrix

description of the optical response and introducing the effect of inelastic charge-carrier scattering through a phenomenological damping rate; this prescription allows us to systematically explore the dependence of HHG yield on the spectral characteristics of the impinging optical pulse and identify frequencies at which HHG is enhanced by optical resonances associated with the electronic band gap or collective electron motion (*i.e.*, plasmons) in SSH chains. We further explore the effect of electrical doping on HHG by populating the electronic bands with additional charge carriers; the added charges can Pauli-block specific electronic transitions and introduce collective resonances, thus facilitating explorations of both. In order to verify the qualitative predictions based on the SSH model in a more realistic condensed-matter platform, we investigate HHG in finite carbon nanotubes (CNTs) of various chiralities that produce similar electronic band features and also display different electronic behavior (metallic, insulating, and topologically insulating). Our findings elucidate the roles of these features intrinsic to different solid-state systems, providing a road map for the identification and engineering of next-generation solid-state nonlinear optical devices, with a view to producing XUV light and/or attosecond pulses.

3.2 Electron dynamics

In our SSH model, spin-degenerate electrons occupy the orbitals $|l\rangle$ located at atomic sites $x_l = la$ uniformly spaced with the lattice constant a. Single-electron states $|\varphi_j\rangle$ with associated energy eigenvalues $\hbar\varepsilon_j$ satisfying $\hbar\varepsilon_j |\varphi_j\rangle = H_0 |\varphi_j\rangle$ are then obtained by expanding in the site basis according to $|\varphi_j\rangle = \sum_l a_{jl} |l\rangle$, where a_{jl} are real-valued expansion coefficients. Following the formalism introduced elsewhere to simulate the optical response of graphene nanoislands,[48,98] the electron dynamics is described by the single-

particle density matrix $\rho = \sum_{ll'} \rho_{ll'} \left|l\right\rangle \left\langle l'\right|$ constructed from time-dependent matrix elements $\rho_{ll'}$ and governed by the equation of motion

$$\dot{\rho} = -\frac{\mathrm{i}}{\hbar}\left[H_0 - e\phi, \rho\right] - \frac{\gamma}{2}\left(\rho - \rho^0\right), \tag{3.1}$$

where ρ^0 denotes the equilibrium density matrix to which the system relaxes at a phenomenological rate $\hbar\gamma = 50\,\mathrm{meV}$ (*i.e.*, a relaxation time $\tau = \gamma^{-1} \sim 13.2\,\mathrm{fs}$) and $\phi = \phi^{\mathrm{ext}} + \phi^{\mathrm{ind}}$ is the electrostatic potential, which includes contributions from both the impinging light electric field, $\phi_l^{\mathrm{ext}} = -x_l E(t)$, and the electron-electron (e-e) interaction, $\phi_l^{\mathrm{ind}} = \sum_{l'} v_{ll'} \rho_{l'}^{\mathrm{ind}}$; the latter quantity renders the equation of motion self-consistent through its dependence on the induced charge $\rho_l^{\mathrm{ind}} = -2e\left(\rho_{ll} - \rho_{ll}^0\right)$ (the factor of 2 accounts for spin degeneracy) mediated by the spatial dependence of the Coulomb interaction $v_{ll'}$ between atoms l and l', for which we choose parameters associated with carbon 2p orbitals.[98] In Fig. 3.1(b) we plot the employed Coulomb interaction compared to that of a point-like charge. The equilibrium density matrix is constructed in the state representation according to $\rho_{jj'}^0 = \delta_{jj'} f_j$, where f_j is the occupation factor of state $\left|\varphi_j\right\rangle$ according to the Fermi-Dirac statistics (we assume zero temperature), and transformed to site representation through $\rho_{ll'} = \sum_{jj'} a_{jl} a_{j'l'} \rho_{jj'}$.

Incidentally, linear response theory [obtained by replacing the $[\phi, \rho]$ term by $[\phi, \rho^0]$ in eq. (3.1)] yields a solution to eq. (3.1) for a monochromatic external electric field $E^{\mathrm{ext}} \mathrm{e}^{-\mathrm{i}\omega t} + \mathrm{c.c.}$ of frequency ω in the form of the harmonic density matrix component $\rho^{(1)}\,\mathrm{e}^{-\mathrm{i}\omega t}$; the induced charge density $\rho^{\mathrm{ind}} = -2e\rho_{ll'}^{(1)}$ (with a factor of 2 for spin degeneracy) is then self-consistently computed in the so-called random-phase approximation[45,137] (RPA) as $\rho^{\mathrm{ind}} = \chi^{(0)}\phi$, where

$$\chi_{ll'}^{(0)} = \frac{2e}{\hbar} \sum_{jj'} \left(f_{j'} - f_j\right) \frac{a_{jl} a_{j'l} a_{jl'} a_{j'l'}}{\omega + \mathrm{i}\gamma/2 - \left(\varepsilon_j - \varepsilon_{j'}\right)} \tag{3.2}$$

is the non-interacting RPA susceptibility. The poles of $\chi^{(0)}$ are related to individual electron-hole (e-h) pair excitations, so that omission of the induced charge by taking $\phi \to \phi^{\mathrm{ext}}$ yields a response comprised of Lorentzian peaks at the energies $\hbar(\varepsilon_j - \varepsilon_{j'})$; including the self-consistent potential, we isolate the induced charge as $\rho^{\mathrm{ind}} = \chi\phi^{\mathrm{ext}}$, where the response function $\chi = \chi^{(0)}\left[1 - \chi^{(0)}v\right]^{-1}$ introduces new poles associated with collective charge carrier excitations through the Coulomb interaction. For simplicity, we neglect exchange interaction and spin effects.

Going beyond linear response, we solve the equation of motion through either of two complementary approaches that allow us to investigate the nonlinear optical response in different regimes. In the first method we resort to direct numerical integration of eq. (3.1) in the time domain (TD) to obtain the induced dipole moment

$$p(t) = -2e\sum_l \rho_l^{\mathrm{ind}} x_l \tag{3.3}$$

produced by various types of external fields $E(t)$ [*e.g.*, continuous wave (CW) illumination or ultrashort pulses], from which Fourier transformation of $p(t)$ reveals its spectral decomposition and characterizes the optical response. The TD approach does not impose any limit on the strength or type of impinging field, thus enabling the study of the intensity-dependent optical response, including simultaneously the effects of saturable absorption and high-order harmonic generation. As we are primarily interested in the latter phenomenon, we quantify the radiation emitted from the SSH chain by the dipole acceleration, $\ddot{p}(\omega) = |\omega^2 p(\omega)|^2$.[133,134,136,138]

In the second approach, we assume monochromatic illumination (as in the RPA) and perturbatively expand the density matrix entering eq. (3.1) according

to

$$\rho = \sum_{n=0}^{\infty} \sum_{s=-n}^{n} \rho^{ns} \mathrm{e}^{\mathrm{i}s\omega t},$$

where $n = 1, 2, \ldots$ denotes the perturbation order and s the harmonic index, such that ρ^{ns} is defined only when $|s| \leq n$. We then obtain the polarizabilities $\alpha_{s\omega}^{(n)}$ as

$$\alpha_{s\omega}^{(n)} = -\frac{2e}{(E_0)^n} \sum_{l} \rho_{ll}^{ns}\, x_l, \tag{3.4}$$

where ρ^{ns} is computed following the prescription in ref. 48 that constitutes an extension of the linear RPA to higher perturbation orders. We employ this method to calculate the nonlinear polarizabilities $\alpha_{\omega}^{(3)}$ (*i.e.*, the leading nonlinear contribution to the response at the fundamental frequency, which is associated with the Kerr nonlinearity and two-photon absorption).

3.3 Su-Schrieffer-Heeger model

Originally introduced to describe p_z electrons in CH monomer chains (polyacetylene), the Su-Schrieffer-Heeger (SSH) model describes a 1D dimerized chain of N atoms through a tight-binding (TB) Hamiltonian,[130] and constitutes a simple yet powerful tool to explore non-trivial topological electronic band structure. We consider an SSH chain that contains $N/2$ unit cells with two sites per cell occupied by one atom from either sublattice A or B [Fig. 3.1(a)]. Also, we denote the intracell and intercell hoppings as t_1 and t_2, respectively.

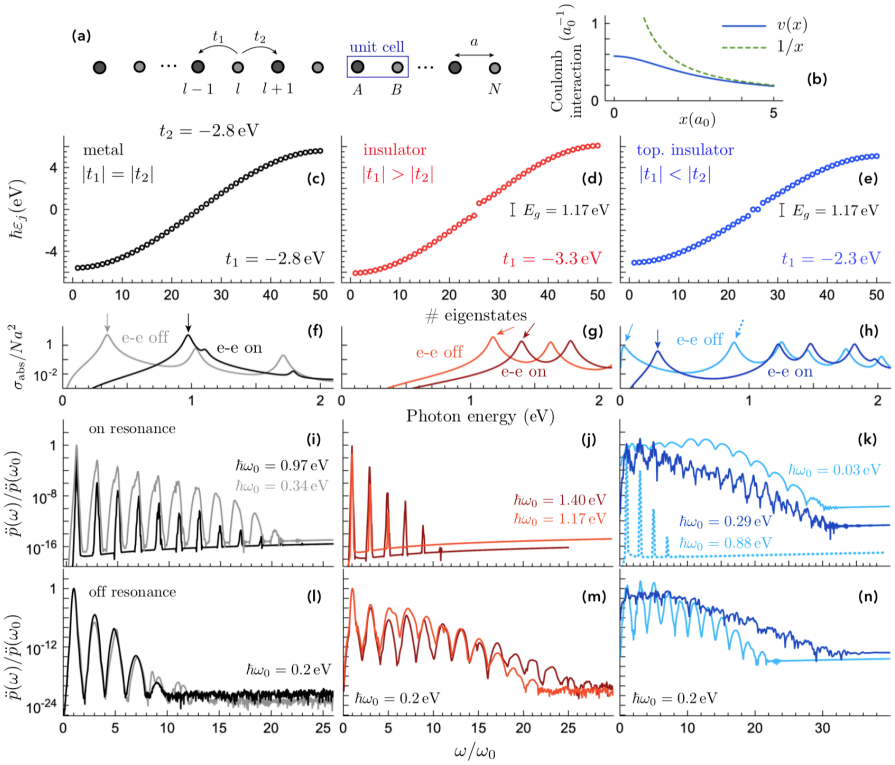

Figure 3.1: **Characterizing the linear and nonlinear optical response of SSH chains. (a)** *Schematic representation of the SSH chain comprised of atoms A and B in the unit cell, with intracell (intercell) hopping t_1 (t_2), and uniform interatomic spacing a.* **(b)** *Coulomb interaction of the SSH chain $v(x)$ compared to $1/x$.* **(c-e)** *Band structure of SSH chains containing $N = 50$ atoms, fixing the intercell hopping to $t_2 = -2.8$ eV and varying the intracell hopping t_1; depending on the choice of t_1 the system is (c) metallic ($t_1 = t_2 = -2.8$ eV, black curves), (d) insulating ($t_1 = -3.3$ eV, red curves), and (e) a topological insulator (TI) ($t_1 = -2.3$ eV, blue curves).* **(f-h)** *Normalized absorption cross section with electron-electron interactions switched on (e-e on) and off (e-e off) for the metal (f), the insulator (g), and the TI (h).* **(i-k)** *Harmonic generation, quantified through the dipole acceleration $\ddot{p}(\omega) = |\omega^2 p(\omega)|^2$ (where $p(\omega)$ denotes the ω component of the induced dipole), produced by pulses of 10^{13} W/m^2 peak intensity, 100 fs FWHM duration, and carrier frequency ω_0, with the latter quantities in each panel indicated by the color-coded legends and arrows in (f-h).* **(l-n)** *Same as (i-k) but for a fixed pulse carrier energy of 0.2 eV, away from the resonances appearing in (f-h).*

The TB Hamiltonian describing the chain is[139]

$$H_0 = t_1 \sum_{l=1}^{N/2} \left(|l, B\rangle \langle l, A| + \text{h.c.} \right) + t_2 \sum_{l=1}^{N/2-1} \left(|l+1, A\rangle \langle l, B| + \text{h.c.} \right), \tag{3.5}$$

which, expressed in a purely spatial representation, takes the form of a tridiagonal $N \times N$ matrix containing zeros along the diagonal and hoppings just above and below:

$$H_0 = \begin{pmatrix} 0 & t_1 & 0 & 0 & \dots & 0 & 0 \\ t_1 & 0 & t_2 & 0 & \dots & 0 & 0 \\ 0 & t_2 & 0 & t_1 & \dots & 0 & 0 \\ 0 & 0 & t_1 & 0 & \dots & 0 & 0 \\ \vdots & \vdots & \vdots & \ddots & \vdots & \vdots & \\ 0 & 0 & 0 & 0 & \dots & 0 & t_1 \\ 0 & 0 & 0 & 0 & \dots & t_1 & 0 \end{pmatrix}. \tag{3.6}$$

The choice of hopping parameters determines the phase of the chain:[139] the band structure becomes metallic when $|t_1| = |t_2|$, insulating if $|t_1| > |t_2|$, and a TI (*i.e.*, insulating in the bulk and with a edge states in the gap) when $|t_1| < |t_2|$.[139] Throughout this study we consider a chain with $N = 50$ atoms located at the sites $x_l = la$ and having fixed intercell hopping $t_2 = t_0$, choosing values $a = 0.1421$ nm and $t_0 = -2.8$ eV inspired by graphene. From the metallic chain ($t_1 = t_2 = t_0$), we perturb $t_1 = t_0 + 0.5$ eV to enter an insulating phase, whereas $t_1 = t_0 - 0.5$ eV yields the band structure of a TI. Diagonalization of H_0 reveals single-electron states characterized by the coefficients a_{jl} (*i.e.*, the amount of wavefunction $|j\rangle$ within the orbital at x_l) and energies $\hbar\varepsilon_j$; we plot the electronic energies $\hbar\varepsilon_j$ obtained for each of the three phases in Fig. 3.1(c-

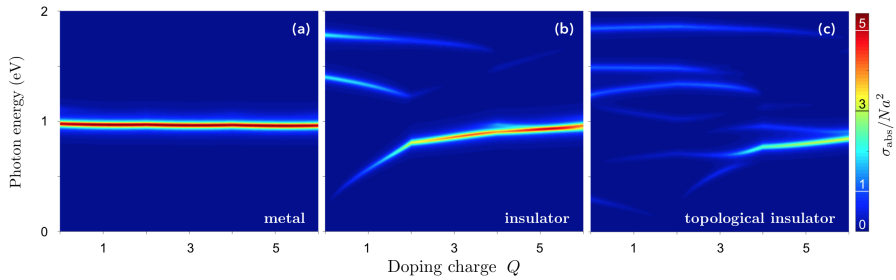

Figure 3.2: **Effect of doping in the linear response of SSH chains.** *Normalized absorption cross section as a function of frequency (vertical axis) and additional charge carriers Q (horizontal axis) for the (a) metallic, (b) insulating, and (c) topologically insulating chains considered in Fig. 3.1.*

e). With the chosen parameters, a band gap of energy $E_g = 1.17$ eV emerges when $|t_1| \neq |t_2|$, with two quasi-degenerate states appearing in the middle of the band gap when $|t_1| < |t_2|$ [Fig. 3.1(d)], corresponding to the edge states of the chain and giving the insulator its topological character.

3.4 Self-consistent interactions in the optical response of SSH chains

Optical resonances, and plasmons in particular, are widely exploited in nano-optics to intensify local electromagnetic fields for a variety of applications, some of which involve the enhancement of nonlinear optical processes.[140,141] Here, we explore the ability of optical resonances in the three phases of the SSH model to drive HHG. In Fig. 3.1(f-h) we identify through the linear absorption cross-section the available optical resonances in the metallic, insulating, and TI phases, both in situations when the self-consistent electron-electron (e-e) interaction is omitted and included. Neglecting e-e interactions, peaks in

the absorption spectrum are associated with the energies of individual single-electron transitions (see discussion in sec. 3.1), with amplitudes determined by their transition dipole moments. In contrast, if we include e-e interactions, the dominant transitions undergo large spectral blueshifts in all three phases. In Figs. 3.1(f-h) we show the absorption cross section of the SSH chains, which we calculate through the optical theorem $\sigma_{\rm abs} = 4\pi(\omega/c){\rm Im}\{\alpha^{(1)}_{\omega}\}$. We normalize the cross section to roughly the geometrical in-plane projection of the chain, Na^2. Incidentally, the edge states of the TI [Fig. 3.1(h)] give rise to a low-energy resonance that does not appear for the insulator.

Given their importance in the linear response, it is expected that self- consistent e-e interactions also play a leading role in the nonlinear response. Figs. 3.1(i-n) show normalized high harmonic spectra (quantified via dipole accelerations) produced by Gaussian pulses of 10^{13} W/m^2 peak intensity and 100 fs full-width-at-half-maximum (FWHM) duration with central frequencies ω_0 (i) targeting the dominant resonances in the linear spectra [Figs. 3.1(i-k); see color-coded arrows indicating the energy of $\hbar\omega_0$] and (ii) off-resonance, with a frequency arbitrarily fixed to 0.2 eV (*i.e.*, away from optical resonances) in all cases [Figs. 3.1(l-n)]. Resonant excitation of the metallic chain yields lower HHG when e-e interactions are included, presumably because charge screening in the metal damps the electron motion, while this effect is less important in the gapped systems. The number of observable harmonics is typically larger for lower-energy excitation and associated with more efficient interband generation, where the maximum cutoff energy in the non-interacting case is indicated by the largest available single-electron transition energy. Incidentally, the height of the first harmonic can vary widely from on-resonant to off-resonant conditions (*e.g.*, by a factor up to 10^4 in metallic chains).

In addition, note that e-e interactions lead to collective optical resonances of higher strength compared with single-electron transitions, thus allowing us to reach HHG with significantly reduced intensity compared with previous

studies that neglect those interactions.[125,142]

Plasmons are associated with the motion of free electrons, and thus do not emerge in pristine semiconducting materials. However, in the 50-atom SSH chains that we consider here, the addition of only a few electron charges is sufficient to dramatically change the optical response; this phenomenon is explored in Fig. 3.2, where we study the linear response in the RPA as a function of the doping charge Q in all three SSH phases. Note that the charge is added in such a way that the free electrons equally populate available degenerate states. In contrast to the almost negligible electrical tuning for the metallic chain [Fig. 3.2(a)], the insulating chains present overall a blueshift with increasing charge carrier density in the low-energy spectral features, which tend to coalesce into a prominent peak associated with intense optical absorption and a concentration of electromagnetic energy within the material.

In particular, at $Q = 2$ in Fig. 3.2(b) we observe a sharp feature that corresponds to the filling of the lowest unoccupied molecular orbital (LUMO); that is, the insulator gets free carriers in the conduction band and starts behaving as a metal (we note that a $Q = 2$ doping corresponds to a Fermi level of ~ 0.81 eV, which is larger than the energy of the LUMO, $E_{\mathrm{LUMO}} = E_g/2 = 0.59$ eV). For this reason, for $Q > 2$ the main resonant feature begins to stabilize and by $Q = 5$ ($E_{\mathrm{F}} \sim 1.11$ eV, where E_{F} here corresponds to the highest-filled state) it has coalesced in a prominent dipolar plasmon mode of frequency similar to that of the metallic chain because of the similar value of the density of states at the Fermi level in both cases. In contrast, for the TI chain [Fig. 3.1(j)] we observe that quasi-degenerate edge states in the middle of the band gap produce a slight redshift of the main resonance and damp the strength of the absorption cross section, particularly at the LUMO energy ($Q = 2$ or $E_{\mathrm{F}} \sim 0.63$ eV). At $Q = 4$ the main resonance starts growing and by $Q = 5$ the response is dominated by the plasmon.

3.5 Intensity-dependent absorption

The realization of HHG in solid-state systems necessitates optical pulses with peak intensities that cannot be sustained for long duration, lest the material be destroyed in the process. However, the interaction of extended pulses or CW fields with matter is appealing for technological applications relying on saturable absorption, an extreme nonlinear optical phenomenon that arises in all photonic materials and, like HHG, cannot be described in a perturbative framework.

The enhanced light-matter interaction provided by optical resonances produces a more measurable absorption signal that facilitates detection of changes in the dielectric environment or the impinging light intensity; the latter effect is intensified by the concentration of electromagnetic energy in the material, which in turn can enhance its nonlinear optical response. Following this approach for HHG, we explore the nonlinear response associated with optical resonances of SSH chains by considering their interaction with intense impinging CW light, characterizing the optical response by the induced dipole moment at the fundamental frequency. Specifically, we extract the effective polarizability α_ω by computing the induced dipole $p(t)$ in response to a monochromatic field $E(t) = E_0 \mathrm{e}^{-\mathrm{i}\omega t} + \mathrm{c.c.}$ of intensity $I^{\mathrm{ext}} = (c/2\pi)|E_0|^2$. We then Fourier transform $p(t)$ over a single optical cycle to obtain

$$\alpha = \frac{\omega}{2\pi E_0} \int_{t_{\mathrm{CW}}-2\pi/\omega}^{t_{\mathrm{CW}}} p(t) \mathrm{e}^{-\mathrm{i}\omega t} dt, \tag{3.7}$$

where $t_{\mathrm{CW}} \gg \tau$ corresponds to a time at which the system has entered a steady state regime.

In Fig. 3.3 we study the dependence on pulse intensity of the main resonances in the absorption spectra (upper rows) of the different SSH chains in relation to their corresponding Kerr polarizabilities $\alpha_\omega^{(3)}$, that is, with pertur-

bation order $n = 3$ and harmonic index $s = 1$ (lower rows), for three different dopings: undoped [Figs. 3.3(a-f)], LUMO doping (*i.e.*, with two additional electrons, $Q = 2$) [Figs. 3.3(g-l)], and plasmonic-regime doping (*i.e.*, with five additional electrons, $Q = 5$).

Independent of doping, the absorption cross section of metallic chains remains relatively unchanged by increasing the optical intensity, an observation compatible with their consistently smaller nonlinear polarizabilities. In contrast, the effective polarizabilities of the insulating phases offer a larger nonlinear response, where in particular Figs. 3.3(c), (h), and (n) present strong saturation and also shifting of the peak energy, which eventually should transition towards a bistable regime. This behavior is corroborated by the large corresponding Kerr polarizabilities [Figs. 3.3(f), (k) and (q), respectively], with the real part determining the peak shift strength and direction (*e.g.*, red- vs blue-shift), while the imaginary part governs its saturation. Within the range of parameters considered here, we conclude that the TI is the most nonlinear material without doping, while the population of its edge states and subsequent Pauli blocking through doping renders its nonlinearity comparable to that of the insulator.

3.6 High-harmonic generation in SSH chains

We further study the optical response of SSH chains to strong ultrashort laser pulses. In Figs. 3.4 and 3.5 we plot the induced dipole acceleration $\ddot{p}$ normalized to the maximum dipole acceleration $\ddot{p}_{\max}$ for each input frequency ω_{in} considering Gaussian pulses of 100 fs FWHM duration and peak intensity $I = 10^{13}$ W/m^2, with the horizontal pulse carrier frequency given on the horizontal axes and the frequency component of $\ddot{p}$ indicated on the vertical axes; each contour plot of $\ddot{p}$ is supplemented by the associated linear optical re-

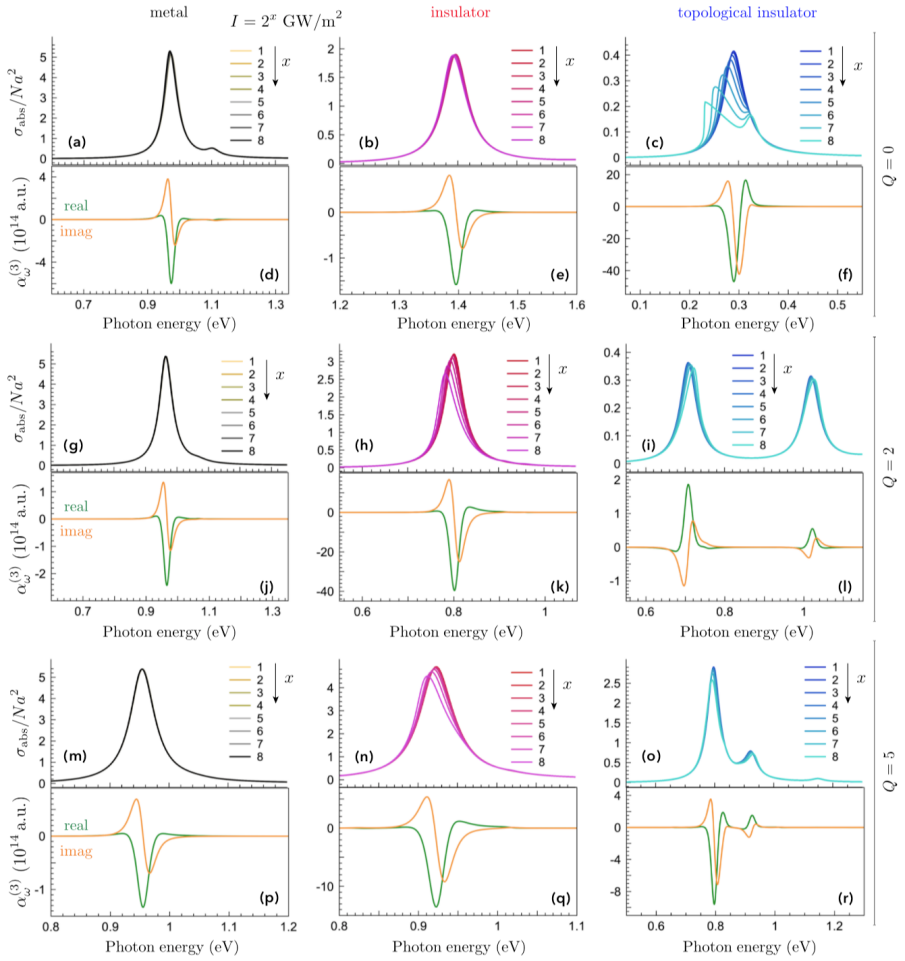

Figure 3.3: **Intensity-dependent nonlinear absorption in SSH chains. (a-c)** *Normalized absorption cross-section $\sigma_{\rm abs}/Na^2$ simulated in the time domain for monochromatic CW illumination of increasing intensity near the optical resonances of undoped (a) metallic, (b) insulating, and (c) topologically insulating SSH chains.* **(d-f)** *Perturbative solutions of the third-order polarizabilities associated with the optical Kerr nonlinearity $\alpha_\omega^{(3)}$, presented in atomic units for the corresponding SSH chains in (a-c), with real and imaginary parts indicated by green and orange curves, respectively.* **(g-l)** *Same as (a-f) but for SSH chains doped with 2 additional electrons ($Q = 2$).* **(m-r)** *Same as (g-l) but for SSH chains doped with 5 additional electrons ($Q = 5$).*

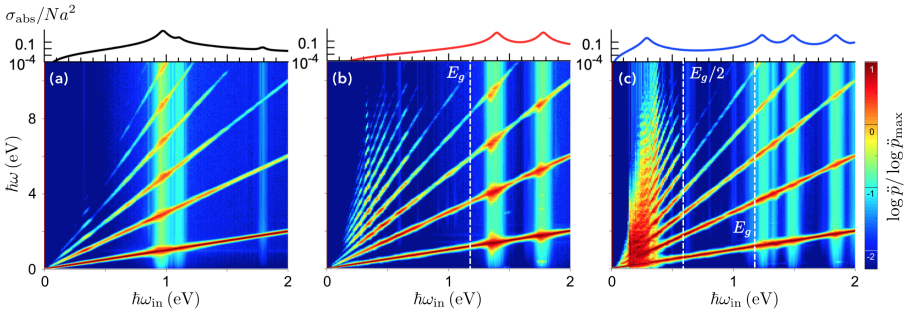

Figure 3.4: **High harmonic generation in undoped SSH chains. (a-c)** *Induced dipole acceleration $\ddot{p}$ in undoped SSH chains as a function of the output frequency ω, as generated by a Gaussian pulse of peak intensity 10^{13} W/m^2, 100 fs FWHM duration, and central frequency $\omega_{\rm in}$ for the (a) metal, (b) insulator, and (c) topological insulator 50-atom SSH chains. The inset above each panel shows the respective linear response of the chain, while the vertical dashed lines mark the band gap energy E_g and its half-value $E_g/2$.*

sponse of the system under consideration (upper panels). In the insulating phases we use white vertical dashed lines to indicate the electronic band gap energy $E_{\rm g}$ and $E_{\rm g}/2$, with the latter quantity indicating the edge-state-to-LUMO transition energy for the TI.

In Fig. 3.4 we consider undoped SSH chains, which present prominent features along the $\omega = s\omega_{\rm in}$ curves, where s is an odd integer (*i.e.*, harmonic generation for $s > 1$). In all cases we observe that strong HHG is produced where the optical resonances intersect with the impinging light frequency, particularly in the low-energy feature observed in the absorption spectrum of the TI [see Fig. 3.4(c)] lying below its band gap and associated with its topologically protected states, for which more high-order harmonics can couple to interband transitions.

In Fig. 3.5 we study HHG in LUMO-doped [Fig. 3.5(a-d)] and plasmonic-regime-doped [Fig. 3.2(e-h)] chains. As in the case of monochromatic excitation, we once again observe that the metal nonlinear response remains rela-

tively unaffected by doping, while the insulator and the TI present higher HHG yields. In panels (d) and (h) of Fig. 3.5 we compare $\ddot{p}$ at the dominant optical resonance of each SSH [a frequency denoted ω_0, see arrows in the upper panels of Figs. 3.5(a-c) and (e-g)]. For $Q = 2$ [Fig. 3.5(d)] the insulator presents the best harmonic yield, producing sizable peaks up to $\sim 25\omega_0$, with harmonics exhibiting a slight blueshift associated with the pulse self-interaction involving the out-of-equilibrium electrons that it excites.[143] In contrast, at $Q = 5$ doping the insulator and TI produce very similar HHG yields that extend up to $\sim 21\omega_0$, with the harmonics produced by the insulator slightly redshifted for $\omega > 9\omega_0$.

3.7 Beyond the SSH model: High harmonic generation in carbon nanotubes

To validate the predictive capabilities of the SSH model, we turn now to a more realistic 1D system in which to study HHG. Carbon nanotubes (CNTs) constitute a material platform that can behave as a metal, insulator, or TI, depending on chirality, and furthermore, like graphene, their electronic properties can be reasonably well-described by a tight-binding Hamiltonian. CNTs themselves hold great potential for diverse applications[144] because of their excellent mechanical, electronic, and optical properties, exemplified through the recent demonstration of a functioning CNT-based transistor.[145] In the field of nanooptics, recent experimental studies have explored the low-energy plasmons supported by CNTs when they are electrically doped,[88,146,147] similar to the collective excitations in highly doped graphene,[148] motivating their application for nanophotonic devices. From a theoretical perspective, plasmons in CNTs have been extensively studied using both *ab initio* methods[149–151] and also semi-classical approaches[93,94,152] based on the RPA[137] to calculate their

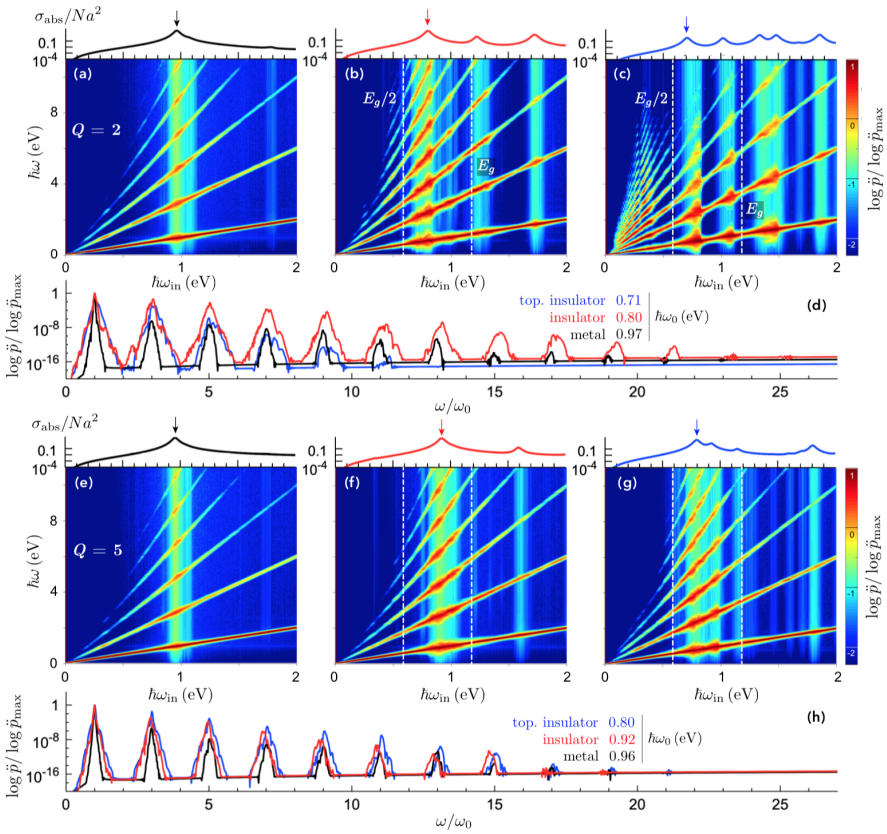

Figure 3.5: **High harmonic generation in doped SSH chains.** *Same as Fig. 3.4 when the chain is doped with either 2 (a-c) or 5 (e-g) electrons. Panels (d) and (h) show the normalized induced dipole at the resonances pointed by the arrows in the linear response for the metal (black), the insulator (red), and the topological insulator (blue) in (a-c) and (e-g), respectively.*

optical conductivities. Incidentally, it has been experimentally proven that electrons in CNTs behave as Luttinger liquids,[153,154] which have special relevance at low temperatures and are qualitatively corroborated by our methods.

CNTs are constructed by wrapping a graphene layer into a cylindrical surface; a carbon atom at the origin is then identified with one at the graphene lattice position $n\boldsymbol{a}_1 + m\boldsymbol{a}_2$, where $\boldsymbol{a}_1$ and $\boldsymbol{a}_2$ are the conventional graphene lattice vectors, while the pair of integers (n, m) determine the chirality of the tube. The resulting CNT diameter (in nm) is[155] $d \approx 78.3\times10^{-3}\sqrt{n^2+m^2+nm}$. We can additionally classify CNTs depending on their topology, which incidentally is determined by n and m: when $n = m$ the CNT is metallic, if $n = m+1$ we have an insulator, and otherwise the CNT is a TI.[156,157] To explore 1D-like structures more similar to SSH chains, we choose extremely thin CNTs experimentally reported with different chiralities.[158–160] Also, to facilitate the comparison with our 50-atom SSH chains, we take them to be roughly 7 nm long. In particular, we consider CNTs with chiralities (3,3), (4,3), and (5,1), which have diameters of 0.41 nm, 0.48 nm, and 0.44 nm, and correspond to a metal, an insulator, and a topological insulator, respectively. In Fig. 3.6 we show the band structures of these three CNTs calculated through a tight-binding model with a phenomenological nearest-neighbors hopping of 2.8 eV,[58,155] revealing $E_\mathrm{g} = 1.80$ eV for the TI and $E_\mathrm{g} = 1.68$ eV for the insulator.

Strong-field driven electron dynamics in CNTs is simulated once again by inserting a tight-binding Hamiltonian into the equation of motion (3.1), adopting a phenomenological damping rate of $\gamma = 50$ meV, and applying 100 fs FWHM laser pulses of intensity $I = 10^{13}$ W/m^2 to excite high harmonics in these structures. In Fig. 3.7 we compare the HHG yields of undoped [Fig. 3.7(a-c)] and doped ($E_\mathrm{F} = 1$ eV) CNTs [Fig. 3.7(d-g)], again supplementing contour plots of $\ddot{p}$ with linear absorption spectra (upper panels). For undoped CNTs we observe weaker HHG for both the insulator and the TI, only exciting up to

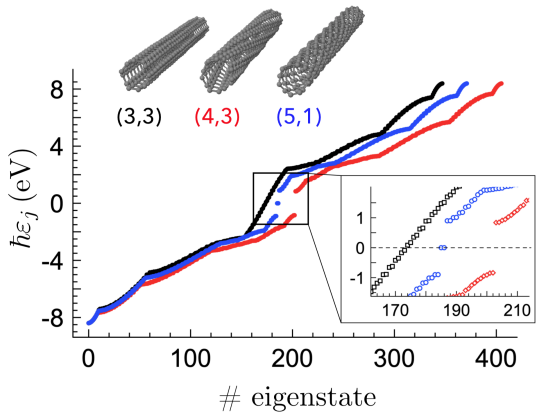

Figure 3.6: **Band structure of CNTs.** *Single-electron energies for CNTs with chiralities (3,3), (4,3), and (5,1), corresponding to a metal (black squares), insulator (red diamonds), and topological insulator (blue circles), respectively. The inset shows the region near zero energy (indicated by the dashed horizontal line) in more detail.*

the 7$^{\text{th}}$ order, in contrast to the metallic tube, exhibiting a distinctly higher HHG yield, particularly when the impinging light energy coincides with the dominant optical resonance near 0.9 eV.

The HHG yield is strongly enhanced by doping the CNTs to a Fermi energy $E_{\text{F}} = 1$ eV [Fig. 3.7(d-g)], which introduces localized plasmon resonances. By inspecting the high harmonics generated at resonant frequencies when excited at optical resonances [Fig. 3.7(g)] we see that both the insulator and the TI have higher yields, that their harmonics are quite strongly redshifted beyond the 7$^{\text{th}}$ order, and that their cutoff is at the 21$^{\text{st}}$ harmonic; this behavior was qualitative predicted by the simpler SSH model.

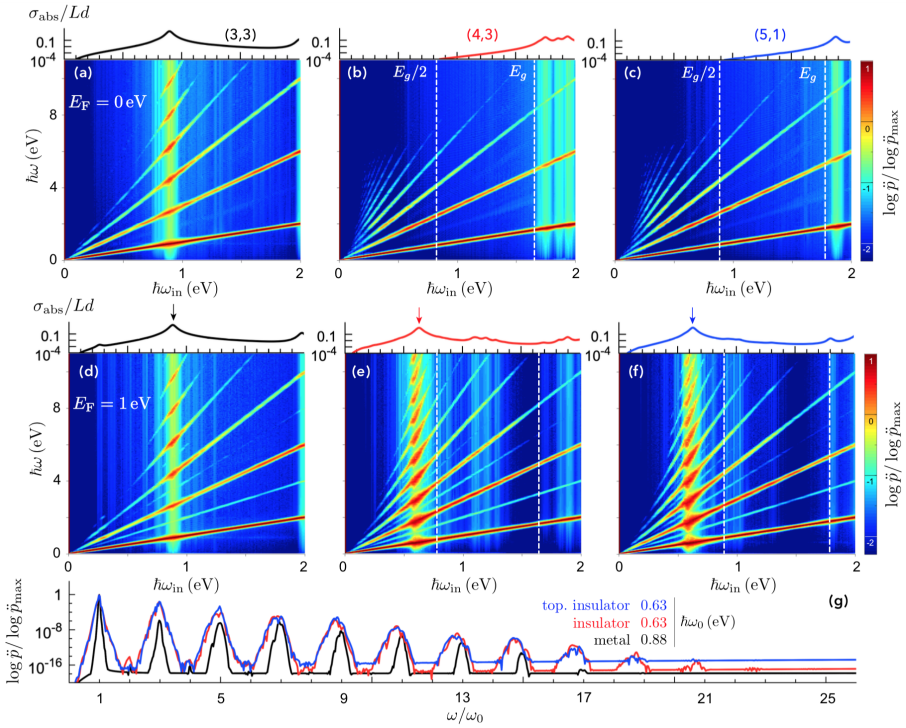

Figure 3.7: **High harmonic generation in CNTs.** **(a-c)** *Dipole acceleration $\ddot{p}$ as a function of the output frequency ω generated by a Gaussian pulse of peak intensity $I = 10^{13}$ W/m^2, 100 fs FWHM duration, and central frequency ω_{in}. The insets above each panel indicate the associated linear response for the (a) metallic, (b) insulating, and (c) topological insulating undoped CNTs. We have marked with white vertical dotted lines both the energy of the band gap E_g and half the energy of the band gap $E_g/2$.* **(d-f)** *Same as (a-c) but for 1 eV-doped CNTs. The arrows indicate the resonant input frequency ω_0 of the Gaussian pulse at which there is a boost in HHG.* **(g)** *Normalized dipole acceleration at the resonances pointed by arrows in the linear response on top of panels (d-f).*

3.8 Conclusions

Despite the impressive pace at which the field of solid-state HHG is developing in both experiment and theory, the ideal material platform in which to realize this extreme nonlinear optical process has yet to be identified. Optical resonances supported by materials with intrinsically different types of electronic structure constitute an underexplored possibility to enhance the electric fields driving HHG, which we address here through the use of an intuitive model that contains much of the relevant physics. More precisely, our conclusions based on the model SSH 1D chain are corroborated in their more realistic carbon-based analogues. In metals or doped semiconductors, where free electrons are present, self-consistent electron interactions become extremely important in both the linear and nonlinear response, and not only when dealing with optical resonances. While HHG appears to be most efficient in semiconductors for harmonics generated below the band gap, the addition of a small amount of doping charge can produce an intraband plasmon excitation that falls in this regime, concentrating the impinging electromagnetic fields and boosting the HHG efficiency; this finding suggests the exploration of highly doped semiconducting materials as a promising platform for solid-state HHG. Our results pave the way for further investigation on the effects of electron-electron interactions in solid-state HHG, elucidating the involved microscopic mechanism and the relation between electronic band structure and the HHG yield, thus supporting its application towards, nonlinear plasmonics, topological optoelectronics, and all-optical time-resolved probing of topological phases.

4

Plasmon generation through electron tunneling

WT: *This is either madness... or brilliance.*
JS: *It's remarkable how often those two traits coincide.*
— Pirates of the Caribbean

The generation of highly confined plasmons through far-field optical illumination appears to be impractical for technological applications due to their large energy-momentum mismatch with external light. Electrical generation of plasmons offers a possible solution to this problem, although its performance depends on a careful choice of material and geometrical parameters. Here we theoretically investigate graphene-based structures and show in particular the very different performances between (i) two layers of graphene separated by a dielectric and (ii) metal/insulator/graphene sandwiches as generators of propagating plasmons assisted by inelastic electron tunneling. For double-layer graphene, we predict plasmon generation rates of $\sim 10^{12} - 10^{14}$/s over an area of the squared plasmon wavelength for realistic values of the spacing and bias voltage, while the yield (plasmons per tunneled electron) has unity order. Furthermore, we study the dependence on the relative tilt an-

gle between the two sheets and show that the plasmon generation efficiency for 4° twist angle drops to ∼20% from its maximum for perfect stacking. For metal/insulator/graphene sandwiches, the inelastic tunneling efficiency drops by several orders of magnitude relative to double-layer graphene, regardless of doping level, metal/graphene separation, choice of metal, and direction of tunneling (metal to or from graphene), a result that we attribute to the small fraction of the surface-projected metal Brillouin zone covered by the graphene Dirac cone. Our results reveal a reasonable tolerance to graphene lattice misalignment and a poor performance of structures involving metals and thus supporting electrical excitation of graphene plasmons in tunneling devices as a viable mechanism for the development of optics-free ultrathin plasmonic devices.

4.1 Introduction

Plasmons offer the means to concentrate optical fields down to nanometer-sized regions and enhance the intensity of externally incident light by several orders of magnitude.[161,162] These properties have been extensively investigated to develop applications in areas as diverse as optical sensing,[73,163–165] medical diagnosis and treatment,[166–168] nonlinear optics,[169,170] catalysis,[171–174] and photovoltaics.[81,175] In this context, plasmons in high-quality graphene offer the advantages of being electrically,[35,36,148,176–178] magnetically,[179,180] and optically[55,181] tunable, while exhibiting short wavelengths and long lifetimes.[182] Graphene plasmons are highly customizable through lateral patterning, stacking of 2D-crystal atomic layers, and coupling to the dielectric environment,[183] enabling applications such as light modulation,[177,184] control of thermal emission,[185–188] spectral photometry,[189,190] and optical sensing.[74,191–193] While these phenomena and applications have been mainly explored at mid-infrared and

lower frequencies, prospects for their extension to the visible and near-infrared spectral regions look promising.[55] Actually, there is no fundamental reason that limits the existence of graphene plasmons at such high frequencies, although in practice they require large doping (*e.g.*, an attainable $E_{\rm F} \sim 1\,$eV Fermi energy[194]) and small lateral size $< 10\,$nm. Although the latter is challenging using top-down lithography, exciting possibilities are opened by bottom-up approaches to the synthesis of nanographenes with only a few nanometers in lateral size,[195,196] while recent experiments on self-assembled graphene nanodisks already reveal plasmons close to the near-infrared.[197] In fact, plasmon-like resonances have been measured in small aromatic hydrocarbons,[69,70] which can be considered as molecular versions of graphene.

The strong confinement of graphene plasmons is clearly indicated by the ratio of plasmon-to-light wavelengths for a self-standing carbon monolayer,[55] $\lambda_{\rm p}/\lambda = 2\alpha(E_{\rm F}/\hbar\omega) \ll 1$, where $\alpha \approx 1/137$ is the fine structure constant and ω is the light frequency. This relation implies that graphene plasmons can be described in the quasistatic limit. Unfortunately, it also means that their in/out-coupling to propagating light is weak. Let us emphasize that far-field coupling in homogeneous graphene is forbidden because plasmons are evanescent surface waves with energy and momentum outside the light cone; however, we refer here to the limited ability of graphene nanostructures to produce in/out plasmon coupling, which is neatly illustrated by their optical extinction and elastic-scattering cross-sections. Indeed, a simple extension of previous analytical theory[55] based on the Drude conductivity indicates that the radiative decay rate of a low-order plasmon in a graphene structure (*e.g.*, a disk) is $\kappa_{\rm r} \sim cAE_{\rm F}/\lambda^3 E_{\rm p}$, which for a plasmon energy $E_{\rm p}$ comparable with the Fermi energy $E_{\rm F}$, a graphene area $A \sim \lambda_{\rm p}^2 \sim 10^{-4}\lambda^2$, and a characteristic photon wavelength of $2\,\mu$m, leads to $\kappa_{\rm r} \sim 0.1/$ns. This is orders of magnitude smaller than the total plasmon decay rate κ. Now, even for an unrealistically optimistic value $\kappa = 1/$ps, the on-resonance plasmon-

driven extinction ($\sigma^{\rm ext} = (3\lambda^2/2\pi)\kappa_{\rm r}/\kappa \sim 10^{-4}\lambda^2$) and elastic-scattering ($\sigma^{\rm scat} = (\kappa_{\rm r}/\kappa)\sigma^{\rm ext} \sim 10^{-8}\lambda^2$) cross-sections are small, thus rendering plasmon coupling to propagating light as a mere retardation correction. In order to circumvent this limitation, many experimental studies in this field have relied on near-field nanoscopy,[198] which is based on the use of sharp tips to enhance this coupling.[35,36,181] However, more compact devices for the generation and detection of graphene plasmons are needed in order to enable the design and development of applications in integrated architectures.

A promising approach consists in exploiting inelastic electron transitions to excite and detect plasmons. Understandably, focused beams in electron microscopes have been the probe of choice to excite and map plasmons with nanometer spatial resolution *via* the recorded electron energy-loss and cathodoluminescence signals.[49] Electron tunneling has been considered for a long time as a mechanism for the excitation of plasmons,[199–207] while electron injection by tunneling from conducting tips into metallic structures has been also demonstrated to produce efficient plasmon excitation.[43,208–211] More dedicated designs have incorporated emitting devices in which the generated light directly couples to the plasmon near-field.[212,213] A recent theoretical study has shown that plasmons can boost tunneling across an insulator separating two graphene layers,[214] with potential use as a plasmon-gain device,[215] while a similar structure has been experimentally used for the electrical generation of THz radiation.[216] Additionally, evidence of radiative gap-plasmon decay has been experimentally obtained associated with hot electron tunneling under external illumination.[217]

In a related context, efforts to realize electrical detection of plasmons have relied on near-field coupling to structures consisting of organic diodes,[218] superconductors,[219] nanowire semiconductors,[220,221] Schottky barriers,[222–224] and 2D semiconductors.[225] Thermoelectric detection has been recently demonstrated in graphene,[190] while a nanoscale detector has been proposed based

on changes produced in the conductivity of graphene nanojunctions.[189] These technologies should benefit from advances in the design, nanofabrication, and theoretical modeling of transistors made from 2D material sandwiches.[226–228]

In this chapter, we theoretically investigate a simple structure in which two closely spaced graphene sheets serve both as gates to produce electron tunneling and as plasmon-supporting elements. We predict a generation efficiency that approaches one plasmon per tunneled electron. Considering attainable doping conditions and bias voltages applied to the graphene layers, we find a generation rate of $\sim 10^{12} - 10^{14}$ plasmons per second over an area of a squared plasmon wavelength for a 1 nm inter-graphene spacing filled with hexagonal boron nitride (hBN). This type of structure provides a key element for future optics-free integrated devices and could also be operated in reversed mode to detect plasmons by decay into tunneled electrons.

Also, we present a comprehensive study of the plasmon-emission efficiency associated with inelastic tunneling between two graphene layers in addition to comparing the results with the emission in metal/insulator/graphene (MIG) configurations. For double layer graphene (DLG), we assess the dependence of the emission efficiency on the relative graphene twisting angle and find a substantial reduction in the efficiency when the K points in the two layers are misaligned by more than a few degrees. For MIG configurations, we find plasmon generation rates way below those of DLG.

4.2 Methods. The spectrally resolved inelastic tunneling current

The large plasmon confinement and small thickness compared with the light wavelength in the structures under consideration allow us to work within the quasistatic limit. We thus calculate the probability for an electron to inelasti-

cally tunnel between initial and final states ψ_i and ψ_f, while transferring an amount of energy $\hbar\omega$ to the materials (*e.g.*, a plasmon), by using the frequency-resolved screened interaction $W(\mathbf{r},\mathbf{r}',\omega)$, which describes the potential created at $\mathbf{r}$ by a point charge placed at $\mathbf{r}'$ and oscillating with frequency ω. More precisely, the probability can be written as[42,49,229]

$$\Gamma(\omega) = 4\frac{2e^2}{\hbar}\sum_{i,f}\int d^3\mathbf{r}\int d^3\mathbf{r}'\,\psi_i^\dagger(\mathbf{r})\cdot\psi_f(\mathbf{r})\psi_f^\dagger(\mathbf{r}')\cdot\psi_i(\mathbf{r}')\times \\ \times\,\mathrm{Im}\{-W(\mathbf{r},\mathbf{r}',\omega)\}\delta(\varepsilon_f-\varepsilon_i+\omega)\;f_i(\hbar\varepsilon_i)\;[1-f_f(\hbar\varepsilon_f)], \quad (4.1)$$

where the leading factor of 4 accounts for spin and valley degeneracies in graphene (the transition probability must be independent of these degeneracies). This factor is the same for DLG and MIG structures, as they involve at least one graphene layer. Electrons undergo transitions from initial occupied states to final empty states of energies $\hbar\varepsilon_i$ and $\hbar\varepsilon_f$, respectively. The occupation of these levels follows the Fermi-Dirac distributions $f_{i|f}(\hbar\varepsilon_{i|f}) = 1/\{1+\exp[(\hbar\varepsilon_{i|f}-E_{\mathrm{F}i|f})/k_{\mathrm{B}}T]\}$, where $E_{\mathrm{F}i}$ and $E_{\mathrm{F}f}$ are the corresponding Fermi energies in the emitting and receiving materials, referenced to a common origin of energies. We work here in the $T=0$ limit, for which these distributions become step functions $f_i(\hbar\varepsilon_i)=\Theta(E_{\mathrm{F}i}-\hbar\varepsilon_i)$ and $1-f_f(\hbar\varepsilon_f)=\Theta(\hbar\varepsilon_f-E_{\mathrm{F}f})$ and the chemical potentials reduce to the corresponding Fermi energies. For initial or final states in graphene, we recast the sum over electron states as $\sum_{i|f}\to(2\pi)^{-2}A\int d^2\mathbf{Q}_{i|f}$, while for metals it becomes $\sum_{i|f}\to(2\pi)^{-3}V\int d^3\mathbf{k}_{i|f}$, where A and V are the corresponding normalization area and volume, respectively. In the evaluation of eq. (4.1), we separate the electron wave functions into parallel and perpendicular components as $\psi(\mathbf{r})=\varphi^{\parallel}(\mathbf{R})\varphi^{\perp}(z)$, where $\mathbf{r}=(\mathbf{R},z)$ and $\mathbf{R}=(x,y)$ are in-plane coordinates. Finally, we present some results below for the loss probability normalized per unit of film surface area $J(\omega)=\Gamma(\omega)/A$ (*i.e.*, the spectrally resolved inelastic tunneling current).

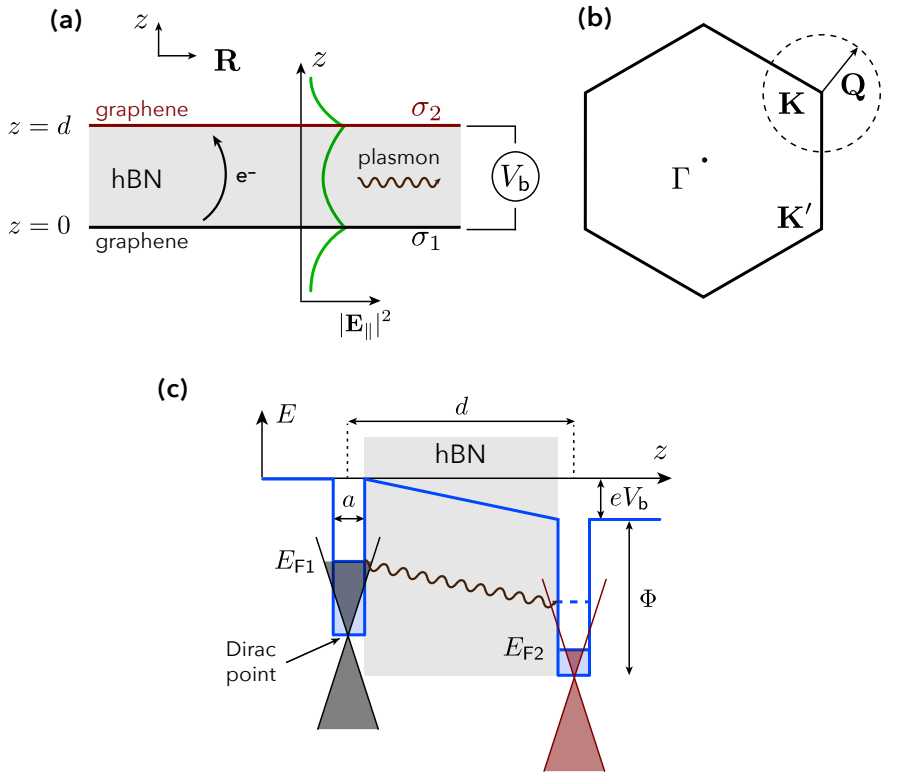

Figure 4.1: **Electron tunneling in double-layer graphene**. **(a)** *We consider a graphene-hBN-graphene sandwich structure consisting of two crystallographically-aligned monolayer graphene sheets separated by an hBN film of thickness d. Electron tunneling takes place upon application of a bias voltage V_b. The graphene layers are described through their wave-vector- and frequency-dependent conductivities $\sigma_1(k_\parallel, \omega)$ and $\sigma_2(k_\parallel, \omega)$. The electric-field intensity associated with the symmetric optical plasmon sustained by this structure is plotted schematically.* **(b)** *High symmetry points in the graphene reciprocal lattice.* **(c)** *We show the electronic bands of the graphene layers and their relative energy positions due to the bias. The Fermi energies $E_{\mathrm{F}1}$ and $E_{\mathrm{F}2}$ and the work function Φ are indicated. The electron wave functions have a dependence along the film normal direction modeled through two quantum wells (blue profile), while Dirac fermions describe their dependence on parallel directions (red cones and parallel electron wave vector Q). Electron tunneling (wiggly arrow) is limited by parallel momentum conservation.*

4.3 Plasmon generation in double layer graphene tunneling structures

The structure under consideration [Fig. 4.1(a)] consists of two perfectly stacked graphene layers separated by a hBN film of thickness $d \simeq 1$ nm (about three atomic layers of hBN), which is maintained throughout this work unless indicated. The graphene sheets are placed at different Fermi energies $E_{\mathrm{F}1}$ and $E_{\mathrm{F}2}$ with conductivities σ_1 (bottom) and σ_2 (top), respectively. Upon application of a bias voltage V_{b} between the two carbon layers, electrons can tunnel from one to the other, assisted by the excitation of a propagating plasmon (inelastic tunneling). We schematically depict the profile of a symmetric plasmon superimposed on the scheme (*i.e.*, an excitation to which the tunneling electrons couple with high efficiency, see below).

Elastic tunneling (*i.e.*, direct tunneling of electrons from one layer to the other) is forbidden due to the vertical displacement of their respective Dirac cones associated with the bias, which introduces a mismatch of parallel wave vectors for all electron energies [see Fig. 4.1(c)]. In contrast, the creation of a plasmon (wiggly arrow) can break this mismatch and enable inelastic tunneling of the electron. Nonetheless, this process involves only a specific energy in the graphene electron bands for each inelastic frequency ω, which is controlled through the applied bias voltage and the Fermi energies of the two carbon layers. The theoretical investigation of plasmon excitation during electron tunneling has been pioneered in the context of junctions between semiconductors using the self-energy.[202] A recent theoretical study[214] discusses in great detail plasmon generation associated with electron tunneling using a second-quantization formalism. We follow instead a more direct approach based upon methods borrowed from the analysis of electron energy-loss spectroscopy.[49]

As briefly discussed above, the elements involved in the theoretical de-

scription of inelastic electron tunneling are *(i)* the conduction electron wave functions; *(ii)* the screened Coulomb potential W that mediates the interaction between those electrons; and *(iii)* the evaluation of the transition probability through a well-established linear-response formalism.[49] We present a self-contained derivation below, under the assumption of crystallographically aligned graphene sheets (*i.e.*, their Dirac cones are on top of each other in 2D momentum space) and also considering electrons tunneling between conduction bands. Remember electrons are assumed to have their wave functions factorized as the product of components parallel (Dirac fermions[58]) and perpendicular to the surface, $\psi_{i|f}(\mathbf{r}) = \varphi^{\parallel}_{i|f}(\mathbf{R})\varphi^{\perp}{}_{i|f}(z)$. The latter accounts for the transversal confinement to the graphene layers, which we describe through a simple potential-well model [blue profile in Fig. 4.1(c)], with parameters fitted to match the work function and electron spill out of p_z orbitals in the material (see Appendix 4.A). Actually, spill out is a crucial element because it determines the overlap of electronic wave functions between the two graphene layers.

For simplicity, we neglect the repulsive electron potential in the hBN region, which should produce a correction to this overlap. The inelastic tunneling current density is then expressed as an integral over parallel electron wave vectors [see eq. (4.4)], which involves the Fermi-Dirac occupation distributions of the graphene bands in the two layers (we assume a temperature of 0 K). The screened Coulomb interaction enters this integral and incorporates the optical responses of the graphene layers (*i.e.*, the corresponding conductivities) and the hBN film (see Appendix 4.C). We use the random-phase approximation[59,61,230] (RPA) to describe the frequency- and wave-vector- dependence of the graphene conductivities, thus incorporating nonlocal effects that are important because both interlayer dielectric coupling and electron tunneling involve large values of the transferred parallel momentum for the short separations under consideration. The conductivities depend on the Fermi en-

ergies of the graphene layers, as well as on the electron lifetime, which we set to a conservative value $\tau = 66$ fs. We remark that our results for the integral of the tunneling current over the plasmon widths ($\sim \tau^{-1}$) is rather independent of the choice of τ (*i.e.*, this property is inherited from the negligible dependence of the frequency integral of the screened interaction $\mathrm{Im}\{W\}$ over the plasmon width).

Now, we break down each of the aforementioned elements that we need to evaluate eq. (4.1):

- *Screened interaction.* We use an analytical expression for the screened interaction describing the graphene/hBN/graphene sandwich given in Appendix 4.C for an asymmetric environment. This expression incorporates the anisotropy of hBN through its parametrized dielectric function[231] for in- and out-of-plane directions, which accounts for optical phonons in this material.

- *Parallel electron wave functions.* We can express the electron wave functions as spinors with two components, each of them associated with one of the two carbon atoms in the unit cell.[58] Consequently, we use a Dirac-fermion description of the in-plane graphene electron wave functions as

$$\varphi^{\parallel}_{i|f}(\mathbf{R}) = \frac{1}{\sqrt{2A}}\, \mathrm{e}^{\mathrm{i}\mathbf{Q}_{i|f}\cdot\mathbf{R}} \begin{pmatrix} \mathrm{e}^{\mathrm{i}\phi_{i|f}/2} \\ \mathrm{e}^{-\mathrm{i}\phi_{i|f}/2} \end{pmatrix} \mathrm{e}^{\mathrm{i}\mathbf{K}\cdot\mathbf{R}}, \tag{4.2}$$

  where $\phi_{i|f}$ is the azimuthal angle of $\mathbf{Q}_{i|f}$ and $\mathbf{K}$ is the wave vector at the K point relative to the Γ point. The first Brillouin zone of the graphene reciprocal lattice is schematically plotted in Fig. 4.1(b). We disregard inter-valley scattering, so each of the two inequivalent K points in the first Brillouin zone produces an identical contribution.

- *Perpendicular electron wave functions.* We describe the evolution of

the electron along z through a one-dimensional wave function trapped in the graphene layers by potential wells, which are vertically offset due to $V_{\rm b}$. Full details of this wave function are given for graphene in Appendix 4.A and are common to all conduction electrons, so we can write ${\varphi^{\perp}}_i(z) = \varphi^{\perp}(z)$ for initial states in layer 1, centered at $z = 0$, and ${\varphi^{\perp}}_f(z) = \varphi^{\perp}(z-d)$ for final states in layer 2, centered at $z = d$. The explicit expressions for metals are offered in Appendix 4.B by treating the surface in the one-electron step-potential approximation.

Additionally, because of translational invariance, the integrand inside $\int d^3\mathbf{r}$ should be independent of $\mathbf{R}$, so we can replace $\int d^2\mathbf{R} \to A$. Now, we express the screened interaction as

$$W(\mathbf{r},\mathbf{r}',\omega) = (2\pi)^{-2} \int d^2\mathbf{k}_{\parallel} \exp[\mathrm{i}\mathbf{k}_{\parallel}\cdot(\mathbf{R}-\mathbf{R}')]\, W(k_{\parallel},z,z',\omega)$$

(see Appendix 4.C), which allows us to carry out the integral over $\mathbf{R}'$ analytically to yield a δ-function for conservation of parallel momentum $\delta(\mathbf{Q}_f - \mathbf{Q}_i + \mathbf{k}_{\parallel})$. This, in turn, can be used to perform the integral over $\mathbf{Q}_f$. Putting these elements together, eq. (4.1) for tunneling between electron-doped conduction bands becomes

$$\begin{aligned}\Gamma(\omega) = \frac{e^2 A}{8\pi^4\hbar} \int d^2\mathbf{k}_{\parallel} \int d^2\mathbf{Q}_i \left| (\mathrm{e}^{-\mathrm{i}\phi_f/2} \quad \mathrm{e}^{\mathrm{i}\phi_f/2}) \cdot \begin{pmatrix} \mathrm{e}^{\mathrm{i}\phi_i/2} \\ \mathrm{e}^{-\mathrm{i}\phi_i/2} \end{pmatrix} \right|^2 \qquad (4.3)\\ \times\ f_1(\hbar v_{\rm F} Q_i)\,[1 - f_2(\hbar v_{\rm F}|\mathbf{Q}_i - \mathbf{k}_{\parallel}|)]\\ \times \int dz \int dz'\ \varphi^{\perp}(z)\varphi^{\perp}(z-d)\varphi^{\perp}(z')\varphi^{\perp}(z'-d)\ \mathrm{Im}\left\{-W(k_{\parallel},z,z',\omega)\right\}\\ \times\ \delta(v_{\rm F}(|\mathbf{Q}_i - \mathbf{k}_{\parallel}| - Q_i) + (E_{\rm F1} - E_{\rm F2})/\hbar - eV_{\rm b}/\hbar + \omega).\end{aligned}$$

Notice that the Fermi-Dirac distributions are referred to the Dirac point of their respective graphene layers. However, the electron energy in layer 2 is

shifted by the bias energy $E_{\rm F1}-E_{\rm F2}-eV_{\rm b}$ relative to layer 1 (last term inside the δ function). We also note that the spinor product yields $|1+\exp[{\rm i}(\phi_i-\phi_f)]|^2=2\left[1+\mathbf{Q}_i\cdot(\mathbf{Q}_i-\mathbf{k}_\parallel)Q_i^{-1}|\mathbf{Q}_i-\mathbf{k}_\parallel|^{-1}\right]$, where we have expressed the angle between $\mathbf{Q}_i$ and $\mathbf{Q}_f=\mathbf{Q}_i-\mathbf{k}_\parallel$ in terms of the inner product of these two vectors. Then, inserting the latter expression into eq. (4.3), and noticing that the result is independent of the direction of $\mathbf{k}_\parallel$ once the $\mathbf{Q}_i$ integral has been carried out, we can make the substitution $\int d\phi_{\mathbf{k}_\parallel}\to 2\pi$ for the azimuthal integral to readily obtain the transition rate Γ which can be separated as $\Gamma=\int_0^\infty d\omega\int_0^\infty dk_\parallel\,\Gamma(k_\parallel,\omega)$. We next divide it by the sandwich area A to obtain the spectrally resolved inelastic tunneling current $J=\Gamma/A$, that is

$$\begin{aligned}J(k_\parallel,\omega)=&\frac{e^2k_\parallel}{2\pi^3\hbar}\int d^2\mathbf{Q}_i\,\left(1+\frac{\mathbf{Q}_i\cdot(\mathbf{Q}_i-\mathbf{k}_\parallel)}{Q_i\,|\mathbf{Q}_i-\mathbf{k}_\parallel|}\right)\\&\times f_1(\hbar v_{\rm F}Q_i)\,[1-f_2(\hbar v_{\rm F}|\mathbf{Q}_i-\mathbf{k}_\parallel|)]\\&\times\int dz\int dz'\,\varphi^\perp(z)\varphi^\perp(z-d)\varphi^\perp(z')\varphi^\perp(z'-d)\,{\rm Im}\left\{-W(k_\parallel,z,z',\omega)\right\}\\&\times\,\delta(v_{\rm F}(|\mathbf{Q}_i-\mathbf{k}_\parallel|-Q_i)+(E_{\rm F1}-E_{\rm F2})/\hbar-eV_{\rm b}/\hbar+\omega),\end{aligned}\tag{4.4}$$

where $v_{\rm F}\approx 10^6$ m/s is the graphene Fermi velocity. Moreover, the δ-function imposes energy conservation and limits the spectral range for which $J(k_\parallel,\omega)$ is nonzero to $(eV_{\rm b}-E_{\rm F1}+E_{\rm F2})/\hbar-v_{\rm F}k_\parallel<\omega<(eV_{\rm b}-E_{\rm F1}+E_{\rm F2})/\hbar+v_{\rm F}k_\parallel$. eq. (4.4) is the expression that we use in our numerical simulations of the spectrally resolved tunneling current, in which the azimuthal ϕ_i integral is carried out analytically by using the relation $\delta[F(\phi_i)]=\sum_j\delta(\phi_i-q_j)/|F'(q_j)|$ for the δ-function (notice that the poles of $F(\phi_i)$ are of first order).

4.3.1 Mapping the inelastic tunneling probability with plasmons

The optical response of the sandwich structure in Fig. 4.1(a) is dominated by graphene plasmons and optical phonons of hBN. The interaction between

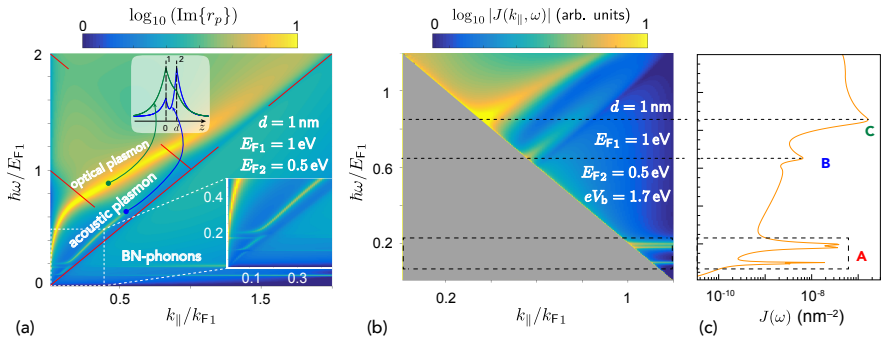

Figure 4.2: **Energy- and momentum-resolved electron tunneling**. **(a)** *Optical dispersion diagram of a graphene-hBN-graphene structure [Fig. 4.1(a)], plotted through the imaginary part of the Fresnel reflection coefficient for p-polarization and incidence on layer 1 as a function of optical energy ω and parallel wave-vector $k_\parallel$. The upper inset shows the electric intensity profiles associated with acoustic and optical plasmons at the energies plotted in (c). The energy and wave-vector axes are normalized to the Fermi energy and wave vector of layer 1, $E_{\mathrm{F}1}$ and $k_{\mathrm{F}1} = E_{\mathrm{F}1}/\hbar v_{\mathrm{F}}$, respectively.* **(b)** *Contribution of different points in the dispersion diagram to inelastic electron tunneling $J(k_\parallel, \omega)$ [eq. (4.4)].* **(c)** *Frequency-dependent momentum-integrated tunneling probability per unit area (horizontal scale) as a function of inelastically transferred energy $\hbar\omega$ (vertical scale). We consider a graphene spacing $d = 1$ nm, Fermi energies $E_{\mathrm{F}1} = 1$ eV and $E_{\mathrm{F}2} = 0.5$ eV, and a bias $eV_{\mathrm{b}} = 1.2$ eV in all cases. The graphene conductivity is modeled in the RPA.*

plasmons in the two neighboring layers produces a characteristic hybridization scheme, leading to two plasmon branches: optical and acoustic. Acoustic plasmons have lower energy, and their out-of-plane electric-field profile looks symmetric. In contrast, optical plasmons possess higher energy and antisymmetric field profiles, so they are generally easier to excite and manipulate and therefore are more suitable for photonic applications.

The frequency- and wave-vector-dependence of these excitations is illustrated in the dispersion diagram of Fig. 4.2(a), which shows the imaginary part of the Fresnel coefficient for p-polarization and incidence from layer 1 [see eq. (4.17)] with a representative choice of interlayer distance $d = 1$ nm and graphene Fermi energies $E_{\mathrm{F}1} = 1$ eV and $E_{\mathrm{F}2} = 0.5$ eV. Given the small thickness of the structure, the s-polarization coefficient (not shown) takes negligible values, further confirming the quasistatic behavior of the system. We consider asymmetric doping of the graphene layers, which consequently display two different plasmon bands. Similar to the hybridization observed for the surface plasmons on either side of a thin metal film,[232] these bands interact and repel each other, thus pushing the upper (optical) plasmon toward higher energies and the lower (acoustic) one further down. Interestingly, nonlocality has a strong influence on the the optical response of this system: the shift produced by hybridization is limited by repulsion from the region of intraband electron-hole-pair transitions [area below the diagonal of the main plot in Fig. 4.2(a)]. As a result of this, the acoustic plasmon stays slightly above this region and exhibits nearly linear dispersion.

The gap regions free from both intra- and interband transitions [triangles defined by the downward straight lines and the main diagonal in Fig. 4.2(a)] are different for the two graphene layers because $E_{\mathrm{F}1} \neq E_{\mathrm{F}2}$. In the smaller gap region (1 eV maximum energy), the optical and acoustic plasmons are both well defined, with their lifetimes roughly equal to the assumed intrinsic value of τ (see above). The acoustic plasmon then fades away when its

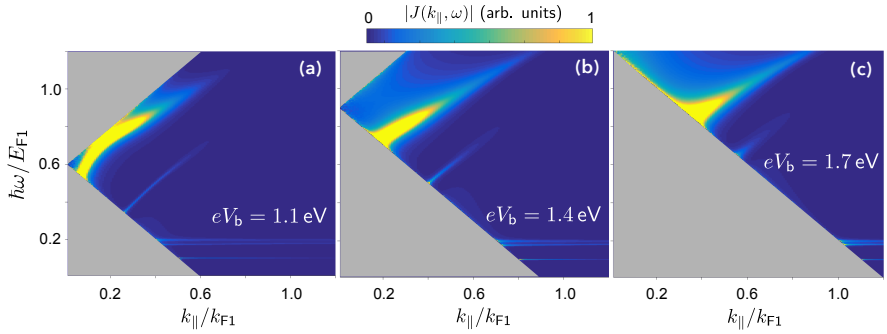

Figure 4.3: **Dispersion diagram of tunneling current components**. *Contribution of different points in the dispersion diagram to the inelastic electron tunneling $J(k_\parallel,\omega)$ [eq. (4.4)], plotted in linear scale for different bias voltages V_b (see labels) under the same conditions as in Fig. 4.2 ($d = 1$ nm, $E_{F1} = 1$ eV, and $E_{F2} = 0.5$ eV). Panel (c) is a replot of Fig. 4.2(b) in linear scale.*

energy increases and it enters the region of interband transitions of the low-doping layer (Landau damping). A similar behavior is observed for the optical plasmons, although the described interband absorption effect is significantly weaker. Examination of the field intensity profiles associated with both plasmons explains this different behavior [Fig. 4.2(a), upper inset]: the acoustic plasmon has larger weight on the low-doping layer (2, at $z = d$), while the optical plasmon receives substantial contributions from both layers; therefore, the effect of interband Landau damping produced by layer 1 (at $z = 0$) acts more strongly on the acoustic plasmon. Additionally, optical plasmons have larger Drude weights than acoustic plasmons (*i.e.*, they are comparatively more weighted on layer 1, which has higher doping electron density), and this contributes to reduce the relative effect produced by coupling to the interband transitions of layer 2.

We find that $J(k_\parallel,\omega)$ [eq. (4.4)] exhibits features that follow the hybrid modes of the system [*cf.* Fig. 4.2(a) and 4.2(b)]. The relative strengths of the

different excitations obviously depend on the applied bias voltage. Additionally, the plot of $J(k_{\|},\omega)$ is dominated by the condition imposed by energy and momentum conservation, which renders a zero contribution outside the region $(-E_{\rm F1}+E_{\rm F2})/\hbar+eV_{\rm b}/\hbar+v_{\rm F}k_{\|}<\omega<(-E_{\rm F1}+E_{\rm F2})/\hbar+eV_{\rm b}/\hbar-v_{\rm F}k_{\|}$. This is more clearly illustrated in Fig. 4.3, where we show $|J(k_{\|},\omega)|$ for different bias voltages, plotted now in linear scale. The momentum-integrated spectral decomposition of the tunneling current $J(\omega)=\int_0^\infty dk_{\|}\,J(k_{\|},\omega)$ [Fig. 4.2(c)] is thus peaked at frequencies $\hbar\omega\approx -E_{\rm F1}+E_{\rm F2}+eV_{\rm b}-\hbar v_{\rm F}k_{\|}$ for values of $k_{\|}$ determined by the dispersion relations of the hBN phonon and the graphene plasmons.

4.3.2 Dependence on bias voltage

The above analysis indicates that the peak frequency of the excited plasmons can be controlled through the applied voltage. This is corroborated by Fig. 4.4(a), in which the peak intensities are in excellent agreement with the combination of threshold and mode dispersion relations, as we argue above. Importantly, the bias also affects the magnitude of the tunneling current [Fig. 4.4(a)].

We are interested in producing a substantial tunneling current, but ultimately, we need that a sizable fraction of the tunneled electrons really generate plasmons. With a suitable choice of the bias voltage, the tunneling current is dominated by the production of either acoustic or optical plasmons [see Fig. 4.4(d)]. As expected, for small voltages, below the thresholds for generation of both acoustic and optical plasmons, phonons dominate the inelastic current, while for large voltages the plasmon contribution becomes small compared with other channels of inelastic tunneling associated with interband electron transitions. Therefore, there is an optimum voltage range in which the generation yield (plasmons per electron) has unity order; tunneling in that range is actually dominated by the excitation of optical plasmons (see region near

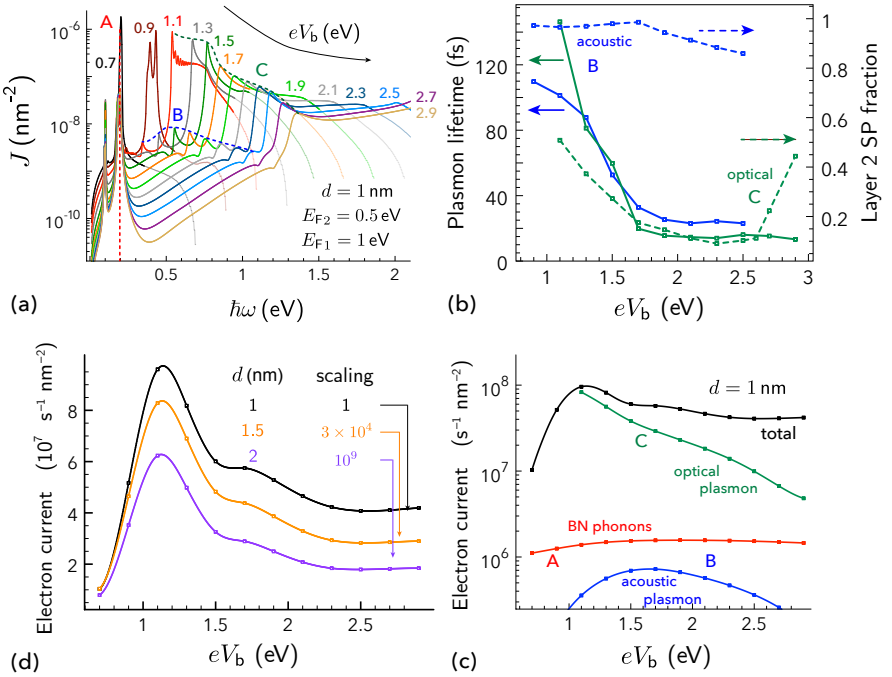

Figure 4.4: **Probability of plasmon-generation by electron tunneling**. **(a)** *Spectrally resolved inelastic tunneling probability for different bias voltages.* **(b)** *Plasmon lifetimes (solid curves, left scale, assuming an intrinsic RPA input lifetime of 66 fs) and fractions of the plasmon weight in layer 2 (dashed curves, right scale, showing the fraction of squared plasmon-induced charge density in that layer).* **(c)** *Contribution of the hBN main optical phonon (A), the acoustic graphene plasmon (B), and the optical graphene plasmon (C) to the total tunneling current density (black curve), corresponding to the spectral features labeled in (a), plotted per square nanometer.* **(d)** *Bias voltage dependence of the total inelastic tunneling current density for various graphene spacings (see labels), multiplied by the indicated factors for the sake of clarity. We consider Fermi energies of 1 eV and 0.5 eV for the graphene layers 1 and 2 in all cases, while the graphene spacing and bias voltage are indicated by axis labels and text insets.*

$eV_\mathrm{b} \sim E_\mathrm{F1} = 1$ eV in Fig. 4.4(d).

Additionally, we are interested in producing long-lived plasmons. Under the conditions of Fig. 4.4, the lifetimes are boosted when the plasmons enter the gap region of the low-doping graphene layer 2 [Fig. 4.4(c)], where they reach values of the order of the assumed intrinsic lifetime τ, which depends on material quality and is ultimately limited by acoustic phonons.[182]

In order to place the calculated tunneling current densities in context, it is pertinent to consider the current produced over an area of a squared plasmon wavelength. This quantity reaches values of $\sim 10^{12} - 10^{14}$/s for a realistic graphene spacing of 1 nm, corresponding to roughly three hBN atomic layers. In this respect, the maximum applied voltage before breakdown takes place is an important factor to consider, as well as the threshold voltage for plasmon generation, which depends on the Fermi energies of the two graphene layers. It is important to stress that the generation efficiency reaches one plasmon per tunneled electron, which should enable the generation of single and few plasmons when combined with quantum electron transport setups.[233]

4.3.3 Dependence on doping level

Once we have seen the suitability of our device for plasmon generation we want to test how robust it is with respect to changes on the doping level of the two graphene layers.

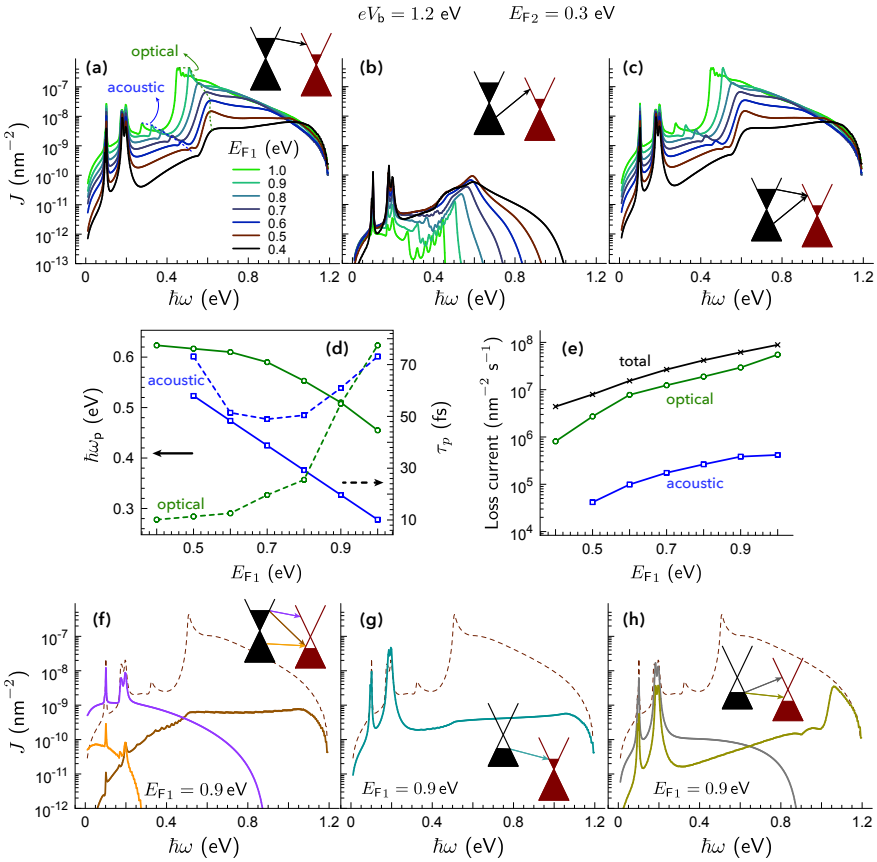

Figure 4.5: Continued on the next page.

Figure 4.5: **Plasmon generation in double-layer graphene: dependence on doping level.** *Asymmetrically doped double-layer graphene (DLG; upper layer at Fermi energy $E_{\mathrm{F2}} = 0.3$ eV, fixed in this figure, and lower layer at varying E_{F1}) with an intercalated hBN film ($d = 1$ nm thickness, corresponding to about 3 atomic layer) and gated with a bias voltage $V_{\mathrm{b}} = 1.2$ eV.* **(a-c)** *Spectrally resolved inelastic tunneling current for different values of E_{F1} when both graphene sheets have electron doping (see insets). We show the separate contributions of (a) conduction-to-conduction and (b) valence-to-conduction transitions, as well as (c) the sum of these two. Optical and acoustic plasmons are marked with labels in (a), while lower-energy, sharp features are associated with the excitation of hBN optical phonons.* **(d)** *Fermi energy dependence for the energies (left axis, solid curves) and lifetimes (right axis, dashed curves) of the optical (green curves) and acoustic (blue curves) plasmon modes in the DLG structure.* **(e)** *Dependence of the total inelastic tunneling current (black curve) on E_{F1}, along with the partial contributions of the optical (green curve) and acoustic (blue curve) plasmons.* **(f-h)** *Spectrally resolved inelastic tunneling current for $E_{\mathrm{F1}} = 0.9$ eV with different types of doping: (f) electron-hole, (g) hole-electron, and (h) hole-hole. Possible transitions between the valence and conduction bands of the two graphene sheets are indicated by arrows in the insets. The contribution of conduction-to-conduction tunneling under electron-electron doping is shown for reference [dashed curves, taken from (a)].*

As tunneling requires $V_{\rm b} \neq 0$ and $E_{\rm F1} \neq E_{\rm F2}$. We take again $E_{\rm F1} > E_{\rm F2}$, and hence, favor tunneling from layer 1 (bottom) to layer 2 (top). We explore the effect of varying the doping-level difference between the two graphene layers by calculating the spectrally resolved inelastic tunneling current as shown in Fig. 4.5(a), where we fix $E_{\rm F2} = 0.3\,$eV and $eV_{\rm b} = 1.2\,$eV. Energy splitting due to phonons in the hBN film can be observed at low-energy transfers (below 0.3 eV), losing strength as the Fermi energy difference $\Delta E_{\rm F} = E_{\rm F1} - E_{\rm F2}$ decreases.

Acoustic plasmons become apparent for $\Delta E_{\rm F} > 0.2\,$eV. These resonances have an average plasmon lifetime of ∼50-70 fs [Fig. 4.5(d), blue-dashed curve] and undergo a redshift with increasing $\Delta E_{\rm F}$ [Fig. 4.5(d), blue-solid curve] and undergo a redshift with increasing $\Delta E_{\rm F}$ [Fig. 4.5(d), blue solid curve]. In contrast, optical plasmons become more pronounced when $E_{\rm F1} > 2E_{\rm F2}$; they experience a milder redshift with increasing $\Delta E_{\rm F}$ [Fig. 4.5(d) green-solid curve], and their lifetime rapidly increases from ∼10 fs to ∼80 fs [Fig. 4.5(d) green-dashed curve].

We quantify the fraction of the total inelastic current invested into exciting plasmons by comparing the area under the whole spectrum in Fig. 4.5(e) for different values of $E_{\rm F1}$ [Fig. 4.5(e), black curve] to the area under either the optical (green curve) or acoustic (blue curve) plasmon regions. The average generation efficiency for the selected values of $V_{\rm b}$ and $E_{\rm F2}$ lies in the ∼20%−60% range for optical plasmons and $< 1\%$ for acoustic modes.

4.3.4 Dependence on the twist angle

In practical devices, the alignment of the two graphene layers can be a challenge, so we examine the effect of a finite twist angle between their respective lattices. Rotations in real space result in rotations around the Γ point in momentum space. In Fig. 4.6(a) we depict two reciprocal lattices corresponding to the bottom (1, black) and top (2, red) layers for a finite rotation angle θ.

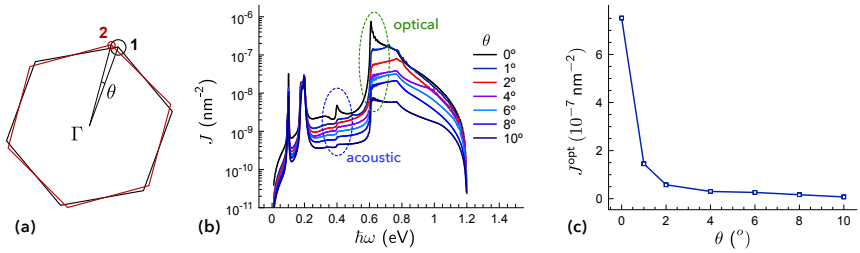

Figure 4.6: **Plasmon generation in double-layer graphene: dependence on tilt angle. (a)** *First Brillouin zones of two graphene layers tilted by an angle* θ (5° *in this plot), along with their respective Fermi surfaces (circular cross sections of their respective Dirac cones; we plot only one per layer) for Fermi energies of* $E_{\mathrm{F}1} = 1$ *eV and* $E_{\mathrm{F}2} = 0.5$ *eV.* **(b)** *Spectrally resolved inelastic tunneling current for different tilt angles and the following choice of parameters:* $eV_{\mathrm{b}} = 1.2$ *eV,* $E_{\mathrm{F}1} = 1$ *eV,* $E_{\mathrm{F}2} = 0.5$ *eV, and* $d = 1$ *nm [see Fig. 4.5(a)]. Optical and acoustic plasmons are marked with labels, while lower-energy, sharp features are associated with the excitation of hBN optical phonons.* **(c)** *Decay of the partial contribution of optical-plasmon excitation to the inelastic current at* $\hbar\omega \approx 0.61$ *eV as a function of tilt angle.*

The circles surrounding their respective K points represent the projections of their Fermi surfaces on 2D momentum space for Fermi energies $E_{\mathrm{F}1} = 1$ eV and $E_{\mathrm{F}2} = 0.5$ eV. Inelastic tunneling requires the two circles to be either overlapping or closer to each other than the plasmon momentum, which is small compared with the Fermi momenta ($k_{\mathrm{F}} = E_{\mathrm{F}}/\hbar v_{\mathrm{F}}$, *i.e.*, the radii of the plotted circles), leading to a cutoff angle $\sim 10^\circ$.

We introduce the twist angle θ in our formalism through the electron wave function of the final states, so that we maintain the initial states as in eq. (4.2) with $\mathbf{K} = \mathbf{K}_i$, but write the final wave function as

$$\varphi_f^{\parallel}(\mathbf{R}) = \frac{1}{\sqrt{2A}}\, \mathrm{e}^{\mathrm{i}\mathbf{Q}_f\cdot\mathbf{R}} \begin{pmatrix} \mathrm{e}^{\mathrm{i}(\phi_f-\theta)/2} \\ \mathrm{e}^{-\mathrm{i}(\phi_f-\theta)/2} \end{pmatrix} \mathrm{e}^{\mathrm{i}\mathbf{K}_f\cdot\mathbf{R}}. \tag{4.5}$$

Notice that $\mathbf{K}_i$ and $\mathbf{K}_f$ are the K points corresponding to the centers of the circles in Fig. 4.6(a). The spinor product in eq. (4.1) involving the parallel wave

functions thus becomes

$$\varphi_i^{\parallel\dagger}(\mathbf{R})\cdot\varphi_f^{\parallel}(\mathbf{R})\varphi_f^{\parallel\dagger}(\mathbf{R}')\cdot\varphi_i^{\parallel}(\mathbf{R}') = \frac{1}{2A^2}\,\mathrm{e}^{\mathrm{i}(\mathbf{K}_f-\mathbf{K}_i+\mathbf{Q}_f-\mathbf{Q}_i)\cdot(\mathbf{R}-\mathbf{R}')} \times\ [1+\cos(\phi_i-\phi_f+\theta)],$$

with $\mathbf{K}_f-\mathbf{K}_i=(2\pi/3a)\,(\cos\theta-\sin\theta/\sqrt{3}-1,\,\sin\theta+\cos\theta/\sqrt{3}-1/\sqrt{3})$. Introducing this expression together with the parallel-wave-vector decomposition of W [eq. (4.15)] into eq. (4.1) and performing the $\mathbf{R}$ and $\mathbf{R}'$ integrals, we find the condition $\mathbf{k}_\parallel+\mathbf{K}_f-\mathbf{K}_i+\mathbf{Q}_f-\mathbf{Q}_i=0$, which guarantees momentum conservation. We find it convenient to separate the contribution of the perpendicular wave functions as

$$I_1(k_\parallel,\omega)=-\int dz\int dz'\;\varphi_i^{\perp\dagger}(z)\varphi_f^{\perp}(z)\varphi_f^{\perp\dagger}(z')\varphi_i^{\perp}(z')\;\mathrm{Im}\{W(k_\parallel,z,z',\omega)\},$$

where $\varphi_{i|f}^{\perp}$ are solutions corresponding to the two quantum wells that we use to model the graphene layers (Appendix 4.A). Putting these elements together, and considering the initial electron to tunnel from the conduction band of layer 1, we can write from eq. (4.1) the spectrally resolved tunneling current density

$$\begin{aligned}J(\omega)=\frac{\Gamma(\omega)}{A}=&\frac{e^2}{4\pi^4}\int d^2\mathbf{Q}_i\int d^2\mathbf{k}_\parallel\;I_1(k_\parallel,\omega)[1+\cos(\phi_i-\phi_f'-\theta)]\\&\times\delta(\hbar v_\mathrm{F}Q_f-\hbar v_\mathrm{F}Q_i+E_{\mathrm{F}1}-E_{\mathrm{F}2}-eV_\mathrm{b}+\hbar\omega)\\&\times\Theta(E_{\mathrm{F}1}-\hbar v_\mathrm{F}Q_i)\;\Theta(\hbar v_\mathrm{F}Q_f-E_{\mathrm{F}2}),\end{aligned}\tag{4.6}$$

where $\mathbf{G}_\parallel=\mathbf{K}_f-\mathbf{K}_i+\mathbf{k}_\parallel$, $\phi_f'=\tan^{-1}[(Q_{yi}-G_{\parallel_y})/(Q_{xi}-G_{\parallel_x})]$, and $Q_f=|\mathbf{Q}_i-\mathbf{G}_\parallel|$. We note that the Dirac δ-function ensures energy conservation in eq. (4.6), limiting the spectral range to $-v_\mathrm{F}G_\parallel+(eV_\mathrm{b}+E_{\mathrm{F}2}-E_{\mathrm{F}1})/\hbar<\omega<v_\mathrm{F}G_\parallel+(eV_\mathrm{b}+E_{\mathrm{F}2}-E_{\mathrm{F}1})/\hbar$. For $\theta=0$ (no twist), this expression reduces to eq. (4.4).

We represent in Fig. 4.6(b) the tunneling current obtained from eq. (4.6) for different rotation angles when fixing the bias voltage to $V_{\rm b} = 1.2$ eV and the Fermi energies to $E_{\rm F1} = 1$ eV and $E_{\rm F2} = 0.5$ eV. When plotting the maximum of $J(\omega)$ associated with the optical plasmon ($\hbar\omega_p^{\rm opt} \simeq 0.61$ eV), we find a sharp decay with increasing twist angle [Fig. 4.6(c)], although we still maintain $\sim 20\%$ of the maximum value for $\theta = 4^\circ$, further indicating a reasonable tolerance of this type of device against unintended misalignments below the 1° level.

So far, we have considered electron doping in both of the graphene layers. We can straightforwardly repeat the above analysis to find expressions that apply to situations in which one or both of the graphene layers is doped with holes. Furthermore, for sufficiently high $V_{\rm b}$, electrons can tunnel from the valence band of layer 1 even when both layers have electron doping, which leads to an additional term in the integrand of eq. (4.6); although we give the resulting expression below these lines, we do not consider such high voltages in this study. We find

$$J(\omega) = \frac{e^2}{4\pi^4} \int d^2\mathbf{Q}_i \int d^2\mathbf{k}_\parallel I_1(k_\parallel, \omega)\ \Delta(\mathbf{Q}_i, \mathbf{k}_\parallel, \omega),$$

where

$\Delta(\mathbf{Q}_i, \mathbf{k}_\parallel, \omega) =$

e-e doping:

$$
\begin{aligned}
&= \delta(\hbar v_{\mathrm{F}} Q_f - \hbar v_{\mathrm{F}} Q_i + E_{\mathrm{F}1} - E_{\mathrm{F}2} - eV_{\mathrm{b}} + \hbar\omega) C_+ \\
&\qquad\qquad \times \Theta(E_{\mathrm{F}1} - \hbar v_{\mathrm{F}} Q_i)\, \Theta(\hbar v_{\mathrm{F}} Q_f - E_{\mathrm{F}2}) \\
&+ \delta(\hbar v_{\mathrm{F}} Q_f + \hbar v_{\mathrm{F}} Q_i + E_{\mathrm{F}1} - E_{\mathrm{F}2} - eV_{\mathrm{b}} + \hbar\omega) C_-\, \Theta(\hbar v_{\mathrm{F}} Q_f - E_{\mathrm{F}2}),
\end{aligned}
$$

e-h doping:

$$
\begin{aligned}
&= \delta(-\hbar v_{\mathrm{F}} Q_f - \hbar v_{\mathrm{F}} Q_i + E_{\mathrm{F}1} + E_{\mathrm{F}2} - eV_{\mathrm{b}} + \hbar\omega) C_- \\
&\qquad\qquad \times \Theta(E_{\mathrm{F}1} - \hbar v_{\mathrm{F}} Q_i)\, \Theta(E_{\mathrm{F}2} - \hbar v_{\mathrm{F}} Q_f) \\
&+ \delta(\hbar v_{\mathrm{F}} Q_f - \hbar v_{\mathrm{F}} Q_i + E_{\mathrm{F}1} + E_{\mathrm{F}2} - eV_{\mathrm{b}} + \hbar\omega) C_+\, \Theta(E_{\mathrm{F}1} - \hbar v_{\mathrm{F}} Q_i) \\
&+ \delta(-\hbar v_{\mathrm{F}} Q_f + \hbar v_{\mathrm{F}} Q_i + E_{\mathrm{F}1} + E_{\mathrm{F}2} - eV_{\mathrm{b}} + \hbar\omega) C_+\, \Theta(E_{\mathrm{F}2} - \hbar v_{\mathrm{F}} Q_f) \\
&+ \delta(\hbar v_{\mathrm{F}} Q_f + \hbar v_{\mathrm{F}} Q_i + E_{\mathrm{F}1} + E_{\mathrm{F}2} - eV_{\mathrm{b}} + \hbar\omega) C_-,
\end{aligned}
$$

h-e doping:

$$
\begin{aligned}
&= \delta(\hbar v_{\mathrm{F}} Q_f + \hbar v_{\mathrm{F}} Q_i - E_{\mathrm{F}1} - E_{\mathrm{F}2} - eV_{\mathrm{b}} + \hbar\omega) C_- \\
&\qquad\qquad \times \Theta(\hbar v_{\mathrm{F}} Q_i - E_{\mathrm{F}1})\, \Theta(\hbar v_{\mathrm{F}} Q_f - E_{\mathrm{F}2}),
\end{aligned}
$$

h-h doping:

$$
\begin{aligned}
&= \delta(-\hbar v_{\mathrm{F}} Q_f + v_{\mathrm{F}} Q_i - E_{\mathrm{F}1} + E_{\mathrm{F}2} - eV_{\mathrm{b}} + \hbar\omega) C_+ \\
&\qquad\qquad \times \Theta(\hbar v_{\mathrm{F}} Q_i - E_{\mathrm{F}1})\, \Theta(E_{\mathrm{F}2} - \hbar v_{\mathrm{F}} Q_f) \\
&+ \delta(\hbar v_{\mathrm{F}} Q_f + \hbar v_{\mathrm{F}} Q_i - E_{\mathrm{F}1} + E_{\mathrm{F}2} - eV_{\mathrm{b}} + \hbar\omega) C_-\, \Theta(\hbar v_{\mathrm{F}} Q_i - E_{\mathrm{F}1}),
\end{aligned}
$$

with $C_\pm = 1 \pm \cos(\phi_i - \phi'_f - \theta)$. The sign in $C_\pm$ (*i.e.*, $+$ for valence-to-valence or conduction-to-conduction transitions, and $-$ otherwise) originates

in the change of the sign of one of the components of the spinor in eqs. (4.2) and (4.5) needed to describe Dirac fermions in the lower Dirac cone instead of the upper one.[58] The labels e (electron) and h (hole) indicate the type of doping in the first and second layers, respectively, and several δ-functions appear in each expression depending on whether the electron originates in the valence or conduction bands (for electron doping in layer 1) or just in the valence band (for hole doping in layer 1), and whether the electron tunnels to the valence or conduction bands (for hole doping in layer 2) or just to the conduction band (for electron doping in layer 2). We define $E_{\mathrm{F}1}$ and $E_{\mathrm{F}2}$ as positive quantities, although it is understood that they represent a lowering of the Fermi energy relative to the Dirac point when doping with holes.

In Figs. 4.5(b) and 4.5(f)-4.5(h) we show results for two perfectly stacked graphene layers with different combinations of h or e doping. Arrows in the insets indicate the different tunneling channels. Additionally, we compare the results to a reference spectrally resolved tunneling probability associated with conduction-to-conduction transitions in two electron-doped graphene layers, which we conclude, in fact, to be the most effective configuration to generate plasmons under the conditions of the figure.

4.4 Plasmon generation in metal/insulator/graphene tunneling structures

We now compare the performance of DLG and MIG structures. In the latter, one of the graphene layers is substituted by a semi-inifinite metal medium. When the tunneling electrons go from the metal to the graphene sheet, not all metals can comply with momentum conservation. In Fig. 4.7(a) we represent the surface projection of the Fermi spheres (assuming for simplicity an independent-electron description of the metal Fermi sea) of different plas-

monic metals (Au, Cu, and Al) compared with the first Brillouin zone of graphene, where we further show the graphene Fermi surface for a doping level $E_{\mathrm{F}}^{\mathrm{gr}} = 1$ eV. When comparing the Fermi wave vectors of these metals ($k_{\mathrm{F}}^{\mathrm{Au}} = 12.1\,\mathrm{nm}^{-1}$, $k_{\mathrm{F}}^{\mathrm{Ag}} = 12.0\,\mathrm{nm}^{-1}$, $k_{\mathrm{F}}^{\mathrm{Cu}} = 13.6\,\mathrm{nm}^{-1}$, $k_{\mathrm{F}}^{\mathrm{Al}} = 17.5\,\mathrm{nm}^{-1}$) with the wave vector at the graphene K point ($K = 17.0\,\mathrm{nm}^{-1}$), considering the small radius of the graphene Fermi circle ($k_{\mathrm{F}}^{\mathrm{gr}} = E_{\mathrm{F}}^{\mathrm{gr}}/\hbar v_{\mathrm{F}} = 1.52\,\mathrm{nm}^{-1}$), we find that only the Al Fermi sea overlaps the graphene Dirac cone, so this is the only one among the good plasmonic metals in which electrons can tunnel to graphene (without the mediation of phonons or defects). Then, it is reasonable to consider the structure represented in Fig. 4.7(b), consisting of a graphene layer on top of an aluminum surface coated with a 1 nm layer of oxide (Al/Al_2O_3/graphene). A gate voltage is then introduced to make metal electrons tunnel into the doped graphene sheet and excite plasmons in the MIG structure.

In contrast, when electrons tunnel from graphene to the metal, the situation is reversed, so it is favorable to have the occupied Dirac-cone region outside the projected metal Fermi sea. This situation is encountered with different choices of metal, in particular with gold, separated from graphene by three atomic layers of hBN, as depicted in Fig. 4.7(c) (Au/hBN/graphene).

For simplicity, we calculate the screened interaction (see Appendix 4.C) assimilating the metal to a perfect electric conductor ($|\epsilon| \to \infty$ is a good approximation for Au and Al within plasmonic energy range under consideration). We further approximate the response of aluminum oxide by using a constant isotropic permittivity $\epsilon_{Al_2O_3} = 3$ (the measured permittivity[32] only changes by $\sim 4\%$ within the energy range under consideration). Finally, we use the RPA conductivity for graphene[61,230] and the anisotropic permittivity described in Appendix 4.C for hBN.[231]

We calculate the spectrally-resolved tunneling probability using eq. (4.1) and the formalism described in the methods, with the metal wave functions

(either as initial or final states, depending on the configuration) described as

$$\psi_{i|f}(\mathbf{r}) = \varphi^{\perp}_{i|f}(z, k_{i|f\,z}) \frac{1}{\sqrt{A}} \, \mathrm{e}^{\mathrm{i}\mathbf{k}^{\parallel}_{i|f}\cdot\mathbf{R}}.$$

The perpendicular component of these wave functions depend on the incident wave vector along z (*i.e.*, $k_{i|f\,z}$) according to the explicit expressions derived in Appendix 4.B under the assumption of a step potential to represent the metal/insulator interface.

As graphene has two sublattices, a small phase difference $\mathrm{e}^{\mathrm{i}\mathbf{k}^{\parallel}_{i}\cdot\mathbf{a}}$ has to be introduced to account in the coupling to the metal wave functions, where $\boldsymbol{a} = a\hat{\mathbf{x}}$ is the C-C bond vector. Additionally, depending on the applied bias, the graphene doping level, and the type of doping (*i.e.*, electrons or holes), only one or the two graphene Dirac cones can be engaged in the tunneling process. Taking these elements into account, the expression for the inelastic tunneling current calculated from eq. (4.1) needs to be specified for each of the following MIG configurations:

- Al $\rightarrow$ Al_2O_3 $\rightarrow$ electron-doped-graphene [see Fig. 4.8(a)]

$$\begin{aligned} J(\omega) = \frac{e^2}{2\pi^4} \int d^2\mathbf{Q}_f \int d^3\mathbf{k}_i \; I_2(k_{\parallel}, k_{iz}, \omega) \; \Theta\left(E_{\mathrm{F}}^{\mathrm{Al}} - \hbar^2 k_i^2/2m_{\mathrm{e}}\right) \\ \times \left[1 + \cos\left(\phi_f + \mathbf{k}_i^{\parallel}\cdot\boldsymbol{a}\right)\right] \Theta(\hbar v_{\mathrm{F}} Q_f - E_{\mathrm{F}}^{\mathrm{gr}}) \\ \times \delta\left(\hbar v_{\mathrm{F}} Q_f - eV_{\mathrm{b}} - E_{\mathrm{F}}^{\mathrm{gr}} - \hbar^2 k_i^2/2m_{\mathrm{e}} + E_{\mathrm{F}}^{\mathrm{Al}} + \hbar\omega\right) \;, \end{aligned} \tag{4.7}$$

- Al $\rightarrow$ Al_2O_3 $\rightarrow$ hole-doped-graphene [see Fig. 4.8(e)]

$$
\begin{aligned}
J(\omega) = \frac{e^2}{2\pi^4} \int d^2\mathbf{Q}_f \int d^3\mathbf{k}_i \; I_2(k_{\parallel}, k_{iz}, \omega) \; \Theta\left(E_{\mathrm{F}}^{\mathrm{Al}} - \hbar^2 k_i^2/2m_{\mathrm{e}}\right) \\
\times \Big\{ \delta\left(-\hbar v_{\mathrm{F}} Q_f - eV_{\mathrm{b}} + E_{\mathrm{F}}^{\mathrm{gr}} - \hbar^2 k_i^2/2m_{\mathrm{e}} + E_{\mathrm{F}}^{\mathrm{Al}} + \hbar\omega\right) \\
\times \left[1 - \cos\left(\phi_f + \mathbf{k}_i^{\parallel} \cdot \boldsymbol{a}\right)\right] \; \Theta(E_{\mathrm{F}}^{\mathrm{gr}} - \hbar v_{\mathrm{F}} Q_f) \\
+ \delta\left(\hbar v_{\mathrm{F}} Q_f - eV_{\mathrm{b}} + E_{\mathrm{F}}^{\mathrm{gr}} - \hbar^2 k_i^2/2m_{\mathrm{e}} + E_{\mathrm{F}}^{\mathrm{Al}} + \hbar\omega\right) \\
\times \left[1 + \cos\left(\phi_f + \mathbf{k}_i^{\parallel} \cdot \boldsymbol{a}\right)\right] \Big\},
\end{aligned}
\tag{4.8}
$$

- electron-doped-graphene $\rightarrow$ hBN $\rightarrow$ Au [see Fig. 4.8(f)]

$$
\begin{aligned}
J(\omega) = \frac{e^2}{2\pi^4} \int d^2\mathbf{Q}_i \int d^3\mathbf{k}_f \; I_3(k_{\parallel}, k_{fz}, \omega) \; \Theta\left(\hbar^2 k_f^2/2m_{\mathrm{e}} - E_{\mathrm{F}}^{\mathrm{Au}}\right) \\
\times \Big\{ \delta\left(-\hbar v_{\mathrm{F}} Q_i - eV_{\mathrm{b}} + E_{\mathrm{F}}^{\mathrm{gr}} + \hbar^2 k_f^2/2m_{\mathrm{e}} - E_{\mathrm{F}}^{\mathrm{Au}} + \hbar\omega\right) \\
\times \left[1 + \cos\left(\phi_i + \mathbf{k}_f^{\parallel} \cdot \boldsymbol{a}\right)\right] \; \Theta(E_{\mathrm{F}}^{\mathrm{gr}} - \hbar v_{\mathrm{F}} Q_i) \\
+ \delta\left(\hbar v_{\mathrm{F}} Q_i - eV_{\mathrm{b}} + E_{\mathrm{F}}^{\mathrm{gr}} + \hbar^2 k_f^2/2m_{\mathrm{e}} - E_{\mathrm{F}}^{\mathrm{Au}} + \hbar\omega\right) \\
\times \left[1 - \cos\left(\phi_i + \mathbf{k}_f^{\parallel} \cdot \boldsymbol{a}\right)\right] \Big\},
\end{aligned}
\tag{4.9}
$$

- hole-doped-graphene $\rightarrow$ hBN $\rightarrow$ Au [see Fig. 4.8(g)]

$$J(\omega) = \frac{e^2}{2\pi^4} \int d^2\mathbf{Q}_i \int d^3\mathbf{k}_f \; I_3(k_\parallel, k_{fz}, \omega) \; \Theta\left(\hbar^2 k_f^2/2m_\mathrm{e} - E_\mathrm{F}^\mathrm{Au}\right) \\ \times \left[1 - \cos\left(\phi_i + \mathbf{k}_f^\parallel \cdot \boldsymbol{a}\right)\right] \; \Theta(\hbar v_\mathrm{F} Q_i - E_\mathrm{F}^\mathrm{gr}) \\ \times \delta\left(\hbar v_\mathrm{F} Q_i - eV_\mathrm{b} - E_\mathrm{F}^\mathrm{gr} + \hbar^2 k_f^2/2m_\mathrm{e} - E_\mathrm{F}^\mathrm{Au} + \hbar\omega\right), \tag{4.10}$$

where the arrows indicate the direction of electron tunneling, the parallel wave vector transfer is $\mathbf{k}_\parallel = \mathbf{K} + \mathbf{Q}_{i|f} - \mathbf{k}_{f|i}^\parallel$, and we have defined

$$I_2(k_\parallel, k_{iz}, \omega) = -\int dz \int dz' \; {\varphi_i^\perp}^\dagger(z, k_{iz}) \varphi_f^\perp(z) {\varphi_f^\perp}^\dagger(z') \varphi_i^\perp(z', k_{iz}) \\ \times \mathrm{Im}\left\{W(k_\parallel, z, z', \omega)\right\} \tag{4.11}$$

for metal $\rightarrow$ graphene tunneling and

$$I_3(k_\parallel, k_{fz}, \omega) = -\int dz \int dz' \; {\varphi_i^\perp}^\dagger(z) \varphi_f^\perp(z, k_{fz}) {\varphi_f^\perp}^\dagger(z', k_{fz}) \varphi_i^\perp(z') \\ \times \mathrm{Im}\left\{W(k_\parallel, z, z', \omega)\right\} \tag{4.12}$$

for graphene $\rightarrow$ metal. We note that energy conservation can only be fulfilled for energies $\hbar\omega < eV_\mathrm{b}$ in all of the these structures.

The contour plots in Fig. 4.7(d) and 4.7(e) portray eqs. (4.11) and (4.12) for fixed values of k_{iz} and k_{fz} in the Al/Al_2O_3/graphene and Au/hBN/graphene structures, respectively, with a graphene Fermi energy fixed to $E_\mathrm{F}^\mathrm{gr} = 1$ eV. They clearly reveal a plasmon mode arising from the poles of the screened potential W. Additionally, Fig. 4.7(e) shows low-energy features associated with hBN phonons in the Au/hBN/graphene structure.

In order to quantify the amount of inelastic current associated with plasmon generation, we separate the screened interaction $W = W^\mathrm{dir} + W^\mathrm{ref}$

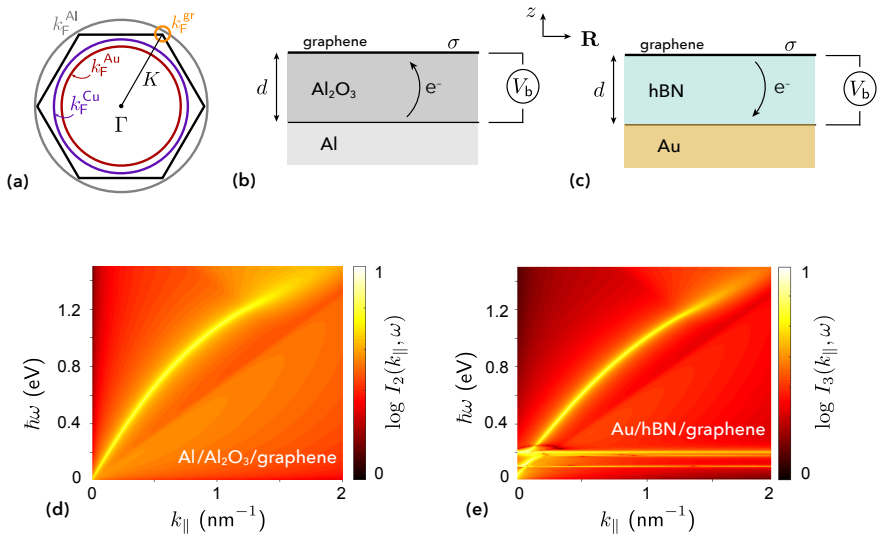

Figure 4.7: **Plasmon generation in metal/insulator/graphene tunneling structures**. **(a)** *Projection of the Fermi surface on the space of wave vectors parallel to the graphene plane for Al (grey), Au (red), and Cu (violet), along with the first Brillouin zone of graphene and its Fermi surface for* $E_{\mathrm{F}}^{\mathrm{gr}} = 1\,\mathrm{eV}$ *doping (orange circle).* **(b)** *Scheme of the Al/*Al_2O_3*/graphene structure gated to a bias voltage* V_{b}*. The thickness of the oxide layer is* $d = 1\,\mathrm{nm}$*. The tunneling current goes from Al to graphene.* **(c)** *Scheme of the Au/hBN/graphene structure gated to a bias voltage* V_{b}*. The thickness of the hBN layers is also* $d = 1\,\mathrm{nm}$ *(about three atomic layers). The tunneling current goes from graphene to Au.* **(d)** *Plasmon dispersion relation given by the poles of the screened potential for the Al/*Al_2O_3*/graphene structure (1 eV doping, tunneling from aluminum to graphene) when the metal is assumed to respond as a perfect conductor [see eq. (4.11)].* **(e)** *Same as (d) with Au instead of Al, hBN instead of* Al_2O_3*, and electrons tunneling from graphene to the metal [see eq. (4.12)].*

into the sum of the external (W^{dir}) and reflected (W^{ref}) components (see Appendix 4.C). Plasmons arise from the poles of W^{ref}, originating in a denominator of the form $\eta(k_\parallel) = 1 + 4\pi \mathrm{i}\sigma k_\parallel/\omega + \tilde{\epsilon}_2 + \mathrm{e}^{2qd}\left(\tilde{\epsilon}_2 - 1 - 4\pi \mathrm{i}\,\sigma k_\parallel/\omega\right)$, where $\tilde{\epsilon}_2 = \sqrt{\epsilon_{2x}\epsilon_{2z}}$, $q = k_\parallel\sqrt{\epsilon_{2x}/\epsilon_{2z}}$, ϵ_{2x} and ϵ_{2z} are the permittivities of the insulator (Al_2O_3 or hBN) along in-plane (x) and out-of-plane (z) directions, and σ is the graphene conductivity. We now isolate this pole and write $W^{\text{ref}} = \eta^{-1}\tilde{W}^{\text{ref}}$. In the vicinity of the plasmon pole $k_\parallel = k_{\text{p}}$, we can Taylor expand $\eta(k_\parallel) = \eta'(k_p)(k_\parallel - k_{\text{p}})$ to first order and approximate the plasmon contribution to eqs. (4.11) and (4.12) as

$$I_2^{\text{pl}}(k_\parallel, k_{iz}, \omega) = -\int dz \int dz'\; {\varphi_i^{\perp}}^{\dagger}(z, k_{iz})\varphi_f^{\perp}(z){\varphi_f^{\perp}}^{\dagger}(z')\varphi_i^{\perp}(z', k_{iz}) \times \text{Im}\left\{\frac{\tilde{W}(k_\parallel, z, z', \omega)}{\eta'(k_p)(k_\parallel - k_p)}\right\}, \tag{4.13}$$

$$I_3^{\text{pl}}(k_\parallel, k_{fz}, \omega) = -\int dz \int dz'\; {\varphi_i^{\perp}}^{\dagger}(z)\varphi_f^{\perp}(z, k_{fz}){\varphi_f^{\perp}}^{\dagger}(z', k_{fz})\varphi_i^{\perp}(z') \times \text{Im}\left\{\frac{\tilde{W}(k_\parallel, z, z', \omega)}{\eta'(k_p)(k_\parallel - k_p)}\right\}. \tag{4.14}$$

By using either eqs. (4.11)-(4.12) or eqs. (4.13)-(4.14) into eqs. (4.7)-(4.10), we obtain the total spectrally-resolved inelastic tunneling current $J(\omega)$ or the contribution arising from plasmon generation $J^{\text{pl}}(\omega)$, respectively.

We show the calculated spectrally-resolved currents $J(\omega)$ and $J^{\text{pl}}(\omega)$ in Figs. 4.8(b) and 4.8(c) for Al $\rightarrow$ Al_2O_3 $\rightarrow$ electron-doped-graphene inelastic tunneling with a bias voltage in the $0.1\,\text{eV} < eV_{\text{b}} < 1.2\,\text{eV}$ range and $E_{\text{F}}^{\text{gr}} = 1\,\text{eV}$. A significant spectral broadening in the total current [Fig. 4.8(b)] originates in the availability of multiple inelastic channels associated for example with electron-hole pair generation in the metal. Indeed, plasmons make a relatively moderate contribution [see Fig. 4.8(c)], as we conclude by compar-

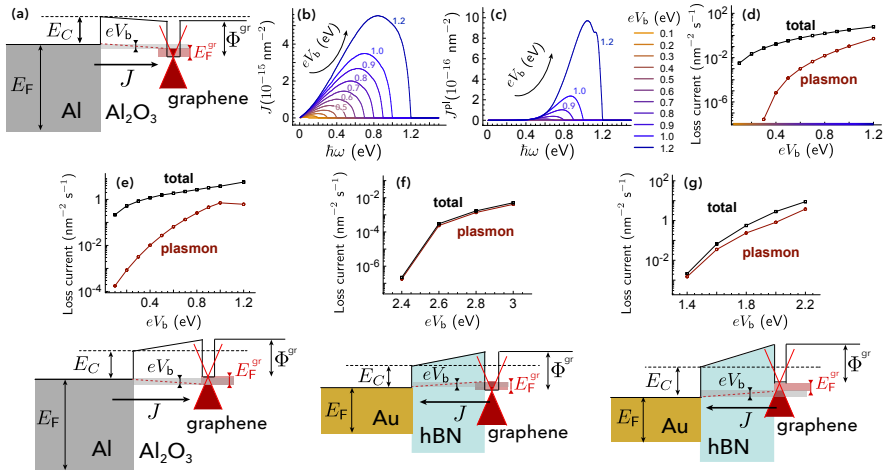

Figure 4.8: **Overview of plasmon generation via electron tunneling in MIG structures. (a)** *Energy bands to scale for the Al/Al_2O_3/graphene sandwich when graphene is electron-doped to $E_F^{gr} = 1$ eV. This Fermi energy is shared by the other configurations shown in this figure.* **(b),(c)** *Spectrally resolved inelastic tunneling current for different bias voltages for the system of (a): (b) total current and (c) plasmon-excitation contribution [using eq. (4.13)]. The value of eV_b for each curve coincides with its spectral cutoff energy $\hbar\omega$.* **(d)** *Dependence of the total inelastic tunneling current (black) and partial plasmon contribution (red) on bias voltage after frequency integration of eq. (4.7) for the system of (a).* **(e)-(g)** *Inelastic tunneling currents equivalent to those in (d) for the configurations shown in the lower insets: (e) Al-Al_2O_3-hole-doped graphene, (f) Au-hBN-electron-doped graphene, and (g) Au-hBN-hole-doped graphene, as obtained from the frequency integral of eqs. (4.8), (4.9) and (4.10), respectively. The graphene work function is $\Phi^{gr} = 4.7$ eV and we choose a bias $eV_b = 0.7$ eV in the sketches.*

ing the total to the plasmon-based ω-integrated inelastic currents [Fig. 4.8(d)]. The plasmon generation efficiency (number of plasmons per tunneling electron, obtained from the ratio J^{pl}/J) varies from $< 10^{-6}$ for $V_{\mathrm{b}} < 0.3$ eV to 0.1 for voltages close to 1.2 eV, where the plasmon generation rate is $\sim 10^{-2}$ nm^{-2}s^{-1}. Fig. 4.8(e)-4.8(g) represents the total and plasmon-based inelastic currents for the configurations depicted below the graphs, from which we conslude that Al $\rightarrow$ Al_2O_3 $\rightarrow$ hole-doped-graphene exhibits better performance, with plasmon generation rates approaching ~ 1 nm^{-2}s^{-1}, while for Au/hBN/graphene structures the currents are 7 orders of magnitude smaller. Overall, comparing the performance of these MIG systems to DLG, we find the latter to be much more efficient, with inelastic currents reaching 10^8 nm^{-2}s^{-1}.

4.5 Outlook

Electrical detection of graphene plasmons can also be accomplished within the sandwich structures under consideration. A plasmon propagating through the structure or laterally confined in a finite-size island can decay by transferring its energy to a tunneling electron under the appropriate bias conditions. Indeed, using high-quality graphene and considering plasmons of frequency and momentum in the gap region of both graphene layers, inelastic electron tunneling should be the dominant channel of plasmon decay, leaving an electron in the low-potential layer and a hole in the high-potential one. In this way, charge separation is naturally accomplished, thus facilitating the electrical detection of the plasmon. There are two favorable factors that support this possibility in graphene: the noted momentum mismatch that prevents direct elastic tunneling (obviously, graphene quality is an important factor to prevent defect-assisted elastic tunneling); and the high spatial concentration of the plasmons, which result in large coupling to inelastic transitions compared

with coupling to photons in tunneling-based inelastic light emission measurements.[205] As an alternative approach, electrical detection could be performed by a separate graphene-based structure *via* thermoelectric measurements[190] or through thermo-optically activated nanoscale junctions.[189]

These concepts are equally applicable to other van der Waals crystals supporting 2D polaritons (*e.g.*, plasmons in black phosphorous,[234,235] or even optical phonons in hBN). Then, our formalism can be easily adapted to materials other than graphene by correcting the electron energies and matrix elements of eq. (4.4) (*e.g.*, using tight-binding electron wave functions[236]), as well as the conductivities of eq. (4.16).

4.6 Conclusions

Our simulations reveal the suitability of DLG heterostructures as plasmon sources since yields can go as high as 1 plasmon per tunneled electron for perfectly stacked heterostructures. Nevertheless, even under moderately unfavorable conditions produced by a finite twist angle between the two graphene sheets, the efficiency is $> 70\%$ for a twist angle as large as 4°. Additionally, we find the relation $E_{\mathrm{F1}} = 2E_{\mathrm{F2}}$ between the Fermi energies of the two layers to be an optimum choice to maximize the plasmon emission rate of both acoustic and optical plasmons, although the efficiency is still in the $> 10\%$ range for order-unity variations in the Fermi energies. Furthermore, our study of MIG structures leads to efficiencies that are orders of magnitude lower than DLG.

From an intuitive viewpoint, these conclusions can be understood using the following argument. We are trying to project electrons from one electrode into the other, which requires conservation of parallel momentum, differing by just the plasmon momentum, which is small compared with the size of the Brillouin zone. For DLG, the matching is most efficient with perfect alignment,

involving large overlaps of their respective Dirac cones, while the tolerance against twisting mentioned above can be roughly quantified by the angle required to produce total mismatch between the Dirac cones, of the order of a few degrees for doping levels of 0.5-1 eV. Unfortunately, when one of the electrodes is a metal, although the conduction electron density at the surface is two to three orders of magnitude larger than that of charge carriers in graphene, they are distributed over a larger momentum-space region, rendering the overlap with the Dirac cone smaller; this effect, together with a weaker plasmon strength in MIG compared with DLG, results in much poorer plasmon generation rates.

In conclusion, the DLG structure under consideration is convenient for the design of integrated plasmonic circuitry. We envision plasmon generation and detection in patches with a lateral size of the order of the plasmon wavelength ($\sim 10-100$ nm for the plasmon energies under consideration). The proposed source generates plasmons peaked at bias-dependent frequencies, but further frequency selection could be performed upon transmission of the plasmons through engineered waveguides. These elements should grant us access into optics-free devices, in which plasmons can perform different operations, for example by interacting with quantum dots and localized molecular excitations, truly relying on their very nature as collective electron excitations, without the mediation of photons whatsoever. Plasmon-based sensors could then consist of a plasmon generation stage, a transmission ribbon exposed to the analyte, and a plasmon detection stage, with some degree of spectral resolution possibly achieved by playing with the graphene Fermi levels and the applied bias voltages. The versatility and excellent performance predicted for the double-graphene sandwich structure opens exciting prospects for the design of modular integrated devices with multiple functionalities.

Appendices

4.A Effective quantum-well description of the out-of-plane graphene electron wave function

We describe the out-of-plane electron wave function of conduction electrons in graphene as a quantum well state. For simplicity, we assume a square well potential of depth V_0 and width a. We focus on the first excited state, which is antisymmetric along the normal direction z, just like the p_z orbital in graphene, as shown in the scheme shown in Fig. 4.A.1.

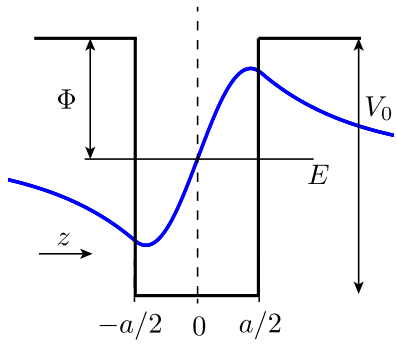

Figure 4.A.1: Quantum well of width a and depth V_0 with the first antisymmetric excited state superimposed at an energy $-\Phi$.

We are therefore interested in the red wave function, which we denote $\varphi^{\perp}(z)$. In this model, the parameters V_0 and a are used to fit *(i)* the state binding energy to the graphene work function[237] $\Phi = 4.7$ eV; and *(ii)* the centroid of the electron density outside the $z = 0$ plane to the value obtained for the carbon $2p$ orbital.

We find the quantum well state $\varphi^{\perp}(z)$ by solving the Schrödinger equation $(-\hbar^2/2m)d^2\varphi^{\perp}(z)/dz^2 + [V(z) - E]\varphi^{\perp}(z) = 0$, where $V(z)$ is the potential shown in the scheme above. The wave function of the first excited state can be written $A\sin(k_{\rm in}z)$ inside the well, with $k_{\rm in} = \sqrt{2m(E+V_0)}/\hbar$, while it decays evanescently in the outer region as $\mathrm{sign}(z)B\mathrm{e}^{-k_{\rm out}|z|}$, with $k_{\rm out} = \sqrt{-2mE}/\hbar$. The electron energy $E < 0$ is referred to the potential outside the well. The continuity of the wave function and its derivate at the well boundaries $z = \pm a/2$ lead to the condition $-k_{\rm in}/k_{\rm out} = \tan(k_{\rm in}a/2)$, which determines the discrete energies E of asymmetric states. Combining these conditions with normalization ($\int dz|\varphi^{\perp}(z)|^2 = 1$), we find $|A|^2 = (a/2 + 1/k_{\rm out})^{-1}$ and $|B|^2 = |A|^2\,\mathrm{e}^{k_{\rm out}a}\sin^2(k_{\rm in}a/2)$.

The centroid of the wave function away from the $z = 0$ plane is calculated as $\int dz\,|z|\,|\varphi^{\perp}(z)|^2$ and compared with the centroid of the p_z orbital of graphene $\int d^3\mathbf{r}\,|z|\,|\varphi_{p_z}(\mathbf{r})|^2$. We approximate the latter by using a tabulated $2p$ atomic carbon wave function,[238] $\varphi_{2p}(\mathbf{r}) = z\sum_j \beta_j e^{-\alpha_j r}$, where the parameters α_j and β_j are expressed in the following table in atomic units:

j	α_j	β_j
1	1.10539	0.4610
2	0.61830	0.0134
3	2.26857	1.5905
4	5.23303	0.7291

In the following plot we show the $2p$ electron probability density integrated over parallel (x, y) directions ($\int dx \int dy\ |\varphi_{2p}(\mathbf{r})|^2$, solid curve), compared with the fitted well state ($|\varphi^{\perp}(z)|^2$, dashed curve). The agreement between the two probability densities is excellent using fitted values $V_0 = 45$ eV and $a = 0.12$ nm (see Fig. 4.A.2).

This value of a is close to (but smaller than) the interlayer spacing in graphite (0.335 nm), which is reasonable due to the spill out of $\varphi^{\perp}$ outside the well. Incidentally, the graphene-electron spill-out toward the gap must depend on

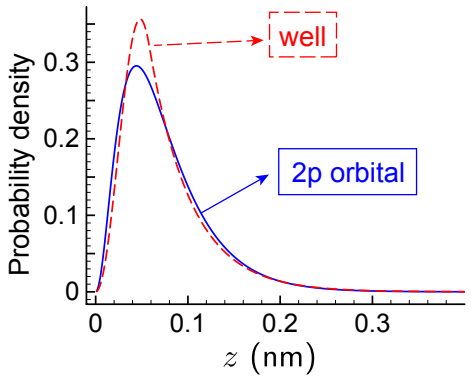

Figure 4.A.2: Probability density of a quantum well (dashed red line) fitted to that of a 2p orbital (solid blue line).

the details of the electron band structure, which should also vary with the filling material. In particular, hBN presents a band gap of ~ 6 eV,[239] so the jump between its conduction-band bottom and the chemical potential is similar to the work function of graphene, and therefore, for simplicity we ignore band-structure effects in hBN and calculate the tunneling electron states by assuming a gap potential at the level of the surrounding vacuum.

4.B Electron wave functions in metal/insulator interfaces

We approximate the electron wave functions in the metal along the z-direction as those of a quantum step-potential, assuming the configuration shown in the scheme in Fig. 4.B.1 (metal for $z < 0$ and insulator for $z > 0$):

The Fermi energies of the metals here considered are $E_{\rm F}^{\rm Al} = 11.7$ eV and $E_{\rm F}^{\rm Au} = 5.53$ eV, referred to the bottom of the conduction band. The parameter E_C accounts for the energy jump of the insulators, for which we take

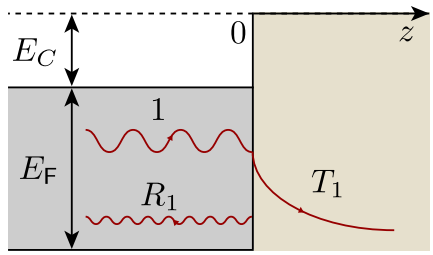

Figure 4.B.1: Configuration with a metal for $z < 0$ and an insulator for $z > 0$.

$E_C^{Al_2O_3} = 3.5\,\text{eV}$[240] and $E_C^{hBN} = 2.6\,\text{eV}$ (*i.e.*, half of their gap energies, under the assumption that their Fermi levels are in the center of the gap, aligned with that of the metal). Moreover, T_1 and R_1 are the transmission and reflection coefficients at the interface, respectively. By solving the time independent Schrödinger equation $(-\hbar^2/2m_e)d^2\varphi^\perp(z)/dz^2 + V(z)\varphi^\perp(z) = E\varphi^\perp(z)$ with $V(z) = -V_0\theta(-z)$ and $V_0 = E_C + E_F$, an electron incident on the interface from the metal side with energy in the insulator gap has the wave function

$$\varphi_i^\perp(z, k_{iz}) = \begin{cases} \frac{1}{\sqrt{2\pi}}\left(e^{ik_{iz}z} + R_1 e^{-ik_{iz}z}\right), & z < 0 \\ \frac{1}{\sqrt{2\pi}} T_1 e^{-k_2 z}, & z > 0 \end{cases}$$

where k_{iz} is the electron wave vector along the interface normal in the metal side, $k_2 = \sqrt{2mV_0/\hbar^2 - k_{iz}^2}$, $R_1 = (k_{iz} - ik_2)/(k_{iz} + ik_2)$ and $T_1 = 2k_{iz}/(k_{iz} + ik_2)$. These wave functions satisfy the orthonormality condition $\int dz \varphi_i^\perp(z, k_{iz})\varphi_i^{\perp\dagger}(z, k'_{iz}) = \delta(k_{iz}, k'_{iz})$. For simplicity, we assume the electron effective mass to be the same as the free electron mass.

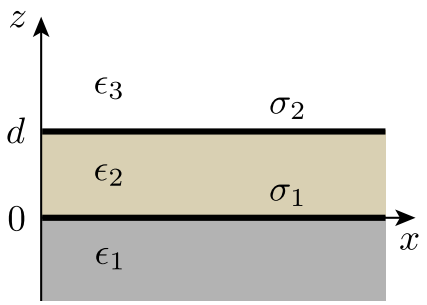

Figure 4.C.1: Multilayer structure with the permittivities $\epsilon_{1|2|3}$ and surface conductivities $\sigma_{1|2}$.

4.C Screened interaction potential

The screened interaction $W(\mathbf{r},\mathbf{r}',\omega)$ is defined as the scalar potential produced at $\mathbf{r}$ by a charge placed at $\mathbf{r}'$ and oscillating with frequency ω. Because of the 2D translational invariance of the system, we can write the screened interaction as

$$W(\mathbf{r},\mathbf{r}',\omega) = \int \frac{d^2\mathbf{k}_\parallel}{(2\pi)^2}\, \mathrm{e}^{\mathrm{i}\mathbf{k}_\parallel\cdot(\mathbf{R}-\mathbf{R}')}\, W(k_\parallel, z, z', \omega) \tag{4.15}$$

in terms of its parallel wave-vector components. We consider a multilayer structure with the permittivities $\epsilon_{1|2|3}$ and surface conductivities $\sigma_{1|2}$ as defined by the scheme in Fig. 4.C.1 which can describe the two configurations considered in this work: MIG (with on of the σ_j conductivities set to zero) and DLG.

So it is natural to work in $\mathbf{k}_\parallel$ space (*i.e.*, we assume an overall $\mathrm{e}^{\mathrm{i}\mathbf{k}_\parallel\cdot(\mathbf{R}-\mathbf{R}')}$ dependence). A point charge placed at z' produces a direct scalar potential $(2\pi/k_\parallel)\mathrm{e}^{-k_\parallel|z-z'|}$ in vacuum (*i.e.*, this is the direct Coulomb interaction term in eq. (3)). Additionally, inside the bulk of an anisotropic dielectric (permit-

tivity ϵ_z along z, and ϵ_x along x and y), the Poisson equation $\nabla \cdot \epsilon \nabla \phi = 0$ has solutions $\phi = \mathrm{e}^{\pm \mathrm{i} q z}$, where $q = k_\parallel \sqrt{\epsilon_x/\epsilon_z}$ and we take the square root to yield $\mathrm{Im}\{q\} > 0$; this allows us to write the point-charge potential as $[2\pi/(\epsilon_z q)]\mathrm{e}^{-q|z-z'|}$ inside that medium. Now, the induced potential has the form $A\mathrm{e}^{k_\parallel z}$ below the sandwich ($z < 0$), $D\mathrm{e}^{k_\parallel (d-z)}$ above it ($z > d$), and $B\mathrm{e}^{-qz} + C\mathrm{e}^{-q(d-z)}$ inside the dielectric ($0 < z < d$). Here, the coefficients A, B, C, and D are used to satisfy the boundary conditions, namely: (1) the continuity of the potential at each graphene layer $j = 1, 2$; and (2) the jump of normal displacement is equal to 4π times the induced charge. From the continuity equation, the induced charge can be expressed as the divergence of the current, and this in turn as the product of the conductivity σ_j times the in-plane electric field. The jump of normal displacement at layer j is then given by $-4\pi \mathrm{i} k_\parallel^2 \sigma_j/\omega$ times the potential. Solving the resulting system of four equations for each position of the external charge z', we obtain, after some tedious but straightforward algebra, the expression for the screened interaction $W(k_\parallel, z, z', \omega)$. Alternatively, a more direct Fabry-Perot-like derivation can be made in terms of the transmission and reflection coefficients of the dielectric/graphene/vacuum interface defined before.

Now, we generalize here for the asymmetric configuration sketched in Fig. 4.C.1. First, we separate

$$W(k_\parallel, z, z', \omega) = W^{\mathrm{dir}}(k_\parallel, z, z', \omega) + W^{\mathrm{ref}}(k_\parallel, z, z', \omega), \tag{4.16}$$

into direct and surface-reflection contributions, where

$$W^{\mathrm{dir}}(k_\parallel, z, z', \omega) = \frac{2\pi}{k_\parallel} \times \begin{cases} (1/\epsilon_1)\mathrm{e}^{-k_\parallel |z-z'|}, & z, z' < 0 \\ (1/\epsilon_3)\mathrm{e}^{-k_\parallel |z-z'|}, & z, z' > d \\ (1/\tilde{\epsilon}_2)\mathrm{e}^{-q|z-z'|}, & 0 < z, z' < d \\ 0, & \text{otherwise} \end{cases}$$

and

$$W^{\mathrm{ref}}(k_\parallel, z, z', \omega) = \frac{(2\pi/k_\parallel)}{1 - A_1' A_2' \mathrm{e}^{-2qd}} \times$$

$$\begin{cases}
(1/\epsilon_3)\mathrm{e}^{k_\parallel(2d-z-z')}\left[A_2 + A_1'(A_2 + B_2')\,\mathrm{e}^{-2qd}\right], & d<z, \quad d<z' \\
(1/\epsilon_3)B_2\,\mathrm{e}^{k_\parallel(d-z)}\left[\mathrm{e}^{-q(d-z')} + A_1'\,\mathrm{e}^{-q(d+z')}\right], & d<z, \quad 0<z'<d \\
(\tilde{\epsilon}_2/\epsilon_3\epsilon_1)B_1B_2\,\mathrm{e}^{k_\parallel(d-z+z')}\mathrm{e}^{-qd}, & d<z, \quad z'<0 \\
(1/\epsilon_3)B_2\,\mathrm{e}^{k_\parallel(d-z')}\left[\mathrm{e}^{-q(d-z)} + A_1'\,\mathrm{e}^{-q(d+z)}\right], & 0<z<d, \quad d<z' \\
(1/\tilde{\epsilon}_2)\big\{A_1'\,\mathrm{e}^{-q(z+z')} + A_2'\,\mathrm{e}^{-q(2d-z-z')} & \\
\quad + A_1'A_2'\left[\mathrm{e}^{-q(2d+z-z')} + \mathrm{e}^{-q(2d-z+z')}\right]\big\}, & 0<z<d, \quad 0<z'<d \\
(1/\epsilon_1)B_1\,\mathrm{e}^{k_\parallel z'}\left[\mathrm{e}^{-qz} + A_2'\,\mathrm{e}^{-q(2d-z)}\right], & 0<z<d, \quad z'<0 \\
(\tilde{\epsilon}_2/\epsilon_1\epsilon_3)B_1B_2\,\mathrm{e}^{k_\parallel(d+z-z')}\mathrm{e}^{-qd}, & z<0, \quad d<z' \\
(1/\epsilon_1)B_1\,\mathrm{e}^{k_\parallel z}\left[\mathrm{e}^{-qz'} + A_2'\,\mathrm{e}^{-q(2d-z')}\right], & z<0, \quad 0<z'<d \\
(1/\epsilon_1)\mathrm{e}^{k_\parallel(z+z')}\left[A_1 + A_2'(A_1 + B_1')\,\mathrm{e}^{-2qd}\right], & z<0, \quad z'<0
\end{cases}$$

If the material 2 is isotropic, we have $q = k_\parallel$ and and $\tilde{\epsilon}_2 = \epsilon_2$. This expression is also applicable when the material in medium 2 is anisotropic (*e.g.*, hBN) by defining $\tilde{\epsilon}_2 = \sqrt{\epsilon_{2x}\epsilon_{2z}}$ as the geometrical average of the in-plane (x) and out-of-plane (z) permittivities, with the square root chosen to yield a positive imaginary part. Also, $q = k_\parallel\sqrt{\epsilon_{2x}/\epsilon_{2z}}$ (with $\mathrm{Re}\{q\} > 0$) is the effective out-of-plane wave vector in that medium, and we have defined the

coefficients

$$
\begin{aligned}
B_1 &= 2\epsilon_1/(\epsilon_1 + \tilde{\epsilon}_2 + \beta_1), \\
B_1' &= (\tilde{\epsilon}_2/\epsilon_1)B_1, \\
B_2 &= 2\epsilon_3/(\epsilon_3 + \tilde{\epsilon}_2 + \beta_2), \\
B_2' &= (\tilde{\epsilon}_2/\epsilon_3)B_2, \\
A_j &= B_j - 1, \\
A_j' &= B_j' - 1, \\
\beta_j &= 4\pi \mathrm{i} k_{\parallel} \sigma_j/\omega,
\end{aligned}
$$

for $j = 1, 2$. In this work, we approximate the permittivity of alumina as a constant value $\tilde{\epsilon}_2 = \epsilon_{Al_2O_3} = 3$, we use the perfect-conductor limit for metals ($|\epsilon_1| \to \infty$), we describe the graphene conductivity in the RPA,[61,230] and we use the expression[231]

$$
\epsilon_{2\ell}(\omega) \approx \epsilon_{\infty,\ell} + \sum_{i=1,2} s_{\ell i}^2/[\omega_{\ell i}^2 - \omega(\omega + \mathrm{i}\gamma_{\ell i})],
$$

for the conductivity of hBN, where $\epsilon_{\infty,z} = 4.10$, $s_{z1} = 70.8$ meV, $\omega_{z1} = 97.1$ meV, $\gamma_{z1} = 0.99$ meV, $s_{z2} = 126$ meV, $\omega_{z2} = 187$ meV, and $\gamma_{z2} = 9.92$ meV for the z component ($\ell = z$); and $\epsilon_{\infty,x} = 4.95$, $s_{x1} = 232$ meV, $\omega_{x1} = 170$ meV, and $\gamma_{x1} = 3.6$ meV, $s_{x2} = 43.5$ meV, $\omega_{x2} = 95.1$ meV, and $\gamma_{x2} = 4.3$ meV for the x component ($\ell = x$). The latter incorporates hBN phonons as Lorentzians terms.

4.D Fresnel's reflection coefficient

Within the quasistatic approximation, the Fresnel reflection coefficient of the graphene-hBN-graphene sandwich vanishes for s-polarization, whereas it can

be readily extracted from eq. (4.16) for p-polarization. Indeed, considering a distant point source in the $z < 0$ region, the external and reflected scalar potentials below the sandwich are $\propto (2\pi/k_\parallel)\mathrm{e}^{-k_\parallel z}$ and $\propto -r_\mathrm{p}\ (2\pi/k_\parallel)\mathrm{e}^{k_\parallel z}$, which allow us to identify

$$r_\mathrm{p} = -\frac{A_1 + A_2'(A_1 + B_1')\mathrm{e}^{-2qd}}{1 - A_1'A_2'\mathrm{e}^{-2qd}} \tag{4.17}$$

by comparison to eq. (4.16) for light incident on layer 1.

4.E Additional plots. Dependence on insulating material

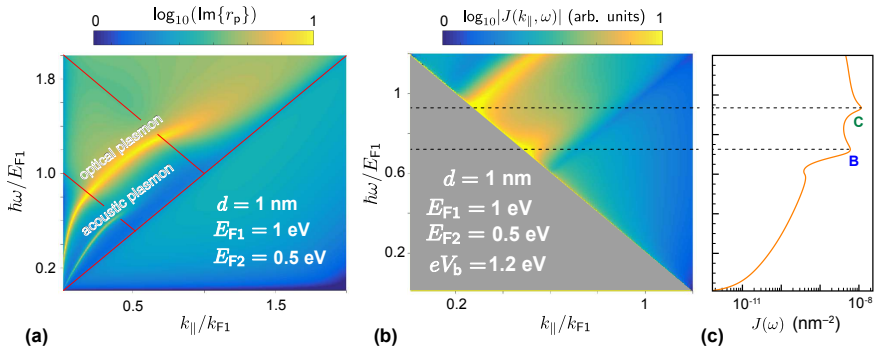

Figure 4.E.1: **Energy- and momentum-resolved electron tunneling with a vacuum gap.** *Same as Fig. 4.2 with the hBN film replaced by vacuum at $T = 300\,\mathrm{K}$ and with eV_b embedding the Fermi energies of the two layers: $eV_\mathrm{b} + E_{\mathrm{F}2} - E_{\mathrm{F}1} \to eV_\mathrm{b}$.*

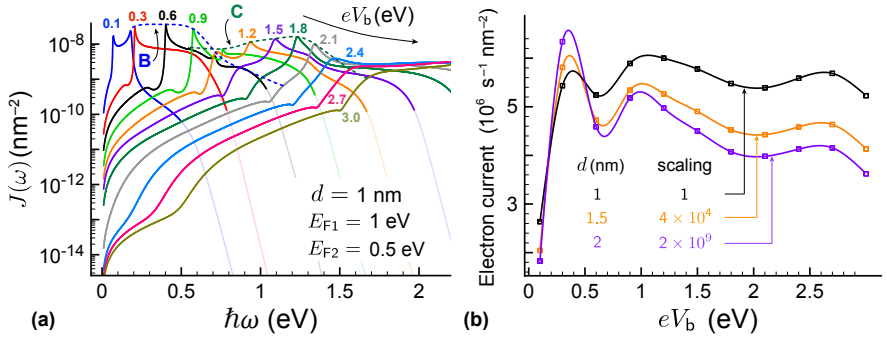

Figure 4.E.2: **Probability of plasmon-generation by electron tunneling with a vacuum gap.** *Same as Figs. 4.4(a,b) with the hBN film replaced by vacuum at* $T = 300\,K$ *and with* eV_b *embedding the Fermi energies of the two layers:* $eV_b + E_{F2} - E_{F1} \to eV_b$.

5

Conclusions and Outlook

Y al cabo, nada os debo; debéisme cuanto he escrito.
– Antonio Machado

We devote the following lines to recapitulate the major findings in this thesis, to give an outlook of possible follow-up works and to show their potential impact.

In chapter 2 we demonstrated that highly-doped finite CNTs exhibit intense plasmon resonances that can mediate the interaction between quantum emitters placed in their proximity. In particular, CNT plasmons are found to produce optical extinction cross-sections exceeding the CNT projected areas, with Purcell factors for proximal quantum emitters reaching $\sim 10^8$, enabling strong interaction between emitters located at opposite ends of a CNT. These plasmons lie in the near-infrared part of the spectrum for realistic tube dimensions, thus holding potential for their use in technological applications within that frequency range. We introduce a classical electromagnetic description of the CNT optical response that predicts plasmon energies and coupling strengths in good agreement with those obtained from an atomistic model (tight-binding description of the electronic states combined with RPA linear re-

sponse) both in the case of capped and uncapped CNTs. Our results indicate a strong potential for highly-doped CNTs as robust, actively tunable plasmonic elements that are well-suited for nanophotonic and quantum-optics applications.

In chapter 3 we found out that optical resonances supported by various materials constitute an under-explored possibility to enhance the electric fields driving HHG, which we have demonstrated there through the use of an intuitive model that contains much of the relevant physics; our conclusions based on the SSH 1D chain are corroborated in their carbon-based analogs. Our findings have shown that in the case of metals or doped semiconductors, where free electrons are present, their interactions become extremely important in both the linear and nonlinear response, and not only when dealing with optical resonances. While HHG appears to be most efficient in semiconductors for harmonics generated below the band gap, the addition of a small amount of doping charge can produce an intraband plasmon excitation that falls in this regime, concentrating the impinging electromagnetic fields and boosting the HHG efficiency; this finding suggests the exploration of highly-doped semiconducting materials as a promising platform for solid-state HHG.

In chapter 4 we showed that the double layer graphene structure under consideration is suitable as plasmon source since the plasmon yield can reach 1 (per tunneled electron) for perfectly stacked heterostructures. But even under moderately unfavorable conditions produced by a finite twist angle between the two graphene sheets, the efficiency is $> 70\%$ for a twist angle as large as 4°. Additionally, we find the relation $E_{\mathrm{F}1} = 2E_{\mathrm{F}2}$ between the Fermi energies of the two layers to be an optimum choice to maximize the plasmon emission rate of both acoustic and optical plasmons, although the efficiency is still in the $> 10\%$ range for order-unity variations in the Fermi energies. Furthermore, our study of metal-insulator-graphene structures leads to efficiencies that are orders of magnitude lower than double layer graphene.

These findings make DLG convenient for the design of integrated plasmonic circuits, as it is moderately robust against twisting of the layers, and plasmon generation takes place for broad ranges of doping (*i.e.*, it is also tolerant concerning variations in doping). The proposed source generates plasmons peaked at bias-dependent frequencies, but further frequency selection could be performed upon transmission of the plasmons through engineered waveguides. These elements should grant us access into optics-free devices, in which plasmons can perform different operations, for example by interacting with quantum dots and localized molecular excitations, truly relying on their very nature as collective electron excitations, without the mediation of photons whatsoever. Plasmon-based sensors could then consist of a plasmon generation stage, a transmission ribbon exposed to the analyte, and a plasmon detection stage, with some degree of spectral resolution possibly achieved by playing with the graphene Fermi levels and the applied bias voltages. The versatility and excellent performance predicted for the double-graphene sandwich structure opens exciting prospects for the design of modular integrated devices with multiple functionalities.

Abbreviations

AFM	atomic force microscope
a.u.	arbitrary or atomic unit
BEM	boundary element method
CNT	carbon nanotube
CW	continuous wave
DFT	density functional theory
DLG	double-layer graphene
EELS	electron energy loss spectroscopy
EM	electromagnetic
EOM	equation of motion
eV	electronvolt
FP	Fabry-Perot
fs	femtosecond
FWHM	full-width-at-half-maximum
hBN	hexagonal boron nitride
HF	Hartree-Fock
LP	localized plasmon
MIG	metal-insulator-graphene
NIR	near infrared
nm	nanometer
PAH	polycyclic aromatic hydrocarbon
QE	quantum emitter
QM	quantum mechanics/al
RPA	random phase approximation
SP	surface plasmon
SSH	Su-Schrieffer-Heeger
TB	tight-binding
TDDFT	time-dependent density functional theory

TE	transverse electric
THz	Teraherzt
TI	topological insulator
TM	transverse magnetic
XUV	extreme ultraviolet

List of Figures

Page

List of Tables

Conference presentations and other activities

Oral contributions to conferences:

- S. de Vega and F. J. García de Abajo. *Plasmon generation through electron tunneling in graphene and metal-insulator-graphene systems*, PIERS, 17–20 Jun 2019, Rome, Italy.
- S. de Vega, J. Cox, F. Sols and F. J. García de Abajo. *Strong-field-driven dynamics and high-harmonic generation in interacting 1D systems*, PIERS, 17–20 Jun 2019, Rome, Italy.
- S. de Vega and F. J. García de Abajo. *Plasmon generation through electron tunneling in graphene and metal-insulator-graphene systems*, NFO-15, 26–31 Aug 2018, Troyes, France.
- S. de Vega and F. J. García de Abajo. *Plasmon generation through electron tunneling in graphene and metal-insulator-graphene systems*, SPIE Photonics Europe, 22–26 Apr 2018, Strasbourg, France.
- S. de Vega, J. D. Cox and F. J. García de Abajo. *Quantum plasmonics with finite carbon nanotubes*, EBSN-2017, 25–27 Oct 2017, Sitges, Spain.
- S. de Vega, J. D. Cox and F. J. García de Abajo. *Quantum plasmonics with finite carbon nanotubes*, META 2016, 25–28 Jul 2016, Málaga, Spain.
- S. de Vega and F. J. García de Abajo. *Plasmonics in atomically flat gold structures*, SPP7, 31 May – 05 Jun 2015, Jerusalem, Israel.
- S. de Vega and F. J. García de Abajo. *Plasmonics in atomically flat gold structures*, ImagineNano, 10–13 Mar 2015, Bilbao, Spain.

Poster contributions to conferences:

- S. de Vega and F. J. García da Abajo. *Plasmon generation through electron tunneling in graphene and metal-insulator-graphene systems*, SPP9, 26–31 May 2019 , Copenhagen, Denmark.
- S. de Vega, J. Cox, F. Sols and F. J. García de Abajo. *Strong-field-driven dynamics and high-harmonic generation in interacting 1D systems*, SPP9, 26–31 May 2019 , Copenhagen, Denmark.
- S. de Vega and F. J. García da Abajo. *Plasmon generation through electron tunneling in graphene*, Nanometa, 03–06 Jan 2019, Seefeld, Austria.
- S. de Vega and F. J. García da Abajo. *Plasmon generation through electron tunneling in graphene*, SPIE Optics + Photonics, 19–23 Aug 2018, San Diego, CA, USA.
- S. de Vega and F. J. García da Abajo. *Plasmon generation through electron tunneling in graphene*, Nanolight 2018, 11–16 Mar 2018, Benasque, Spain.
- S. de Vega and F. J. García de Abajo. *Plasmon generation through electron tunneling in graphene*, EBSN-2017, 25–27 Oct 2017, Sitges, Spain.
- S. de Vega, J. D. Cox and F. J. García de Abajo. *Quantum plasmonics with finite carbon nanotubes*, NFO-14, 04–09 Sep 2016, Hamamatsu, Japan.
- S. de Vega, J. D. Cox and F. J. García de Abajo. *Quantum plasmonics with finite carbon nanotubes*, Nanolight 2016, 06–11 Mar 2016, Benasque, Spain.

Outreach presentations:

- S. de Vega. *Triggering plasmons in graphene heterostructures without light* ICFO's Graphene Coffee Flash-talk Series, 05 May 2019, Castelldefels, Spain.

- S. Keary, J. M. Pérez-Rosas, S. de Vega and P. M. Winkler (alphabetic order). *ICONS activities. Career development, lectures, talks and social events*, SPIE Optics + Photonics, 19–23 Aug 2018, San Diego, CA, USA.

- S. de Vega. *Photonics in Flatland*, Diversity in the Cultures of Physics Summer School Barcelona - Uppsala, 18 Jul 2018, Castelldefels, Spain.

- S. de Vega. *Optics-free manipulation at the nanoscale*, ICFO's Flash-talks, 04 May 2018, Castelldefels, Spain.

- K. K. Gopalan, L. Laparra Cuervo, J. M. Pérez-Rosas and S. de Vega (alphabetic order). *ICONS activities. Career development, lectures, talks and social events*, Diversity in the Cultures of Physics Summer School Barcelona - Berlin, 27 Jul 2017, Castelldefels, Spain.

- K. K. Gopalan, L. Laparra Cuervo, J. M. Pérez-Rosas and S. de Vega (alphabetic order). *ICONS activities. Career development, lectures, talks and social events*, IONS Paris 2017, 14–17 Jun 2017, Orsay, France.

- K. K. Gopalan, J. R. M. Saavedra and S. de Vega (alphabetic order). *On a Lighter Note*, ICFO Day, 02 Dec 2016, Castelldefels, Spain.

- S. de Vega. *Ramas de investigación en Fotónica*, UCM Seminar Series, 02 Nov 2016, Madrid, Spain.

- S. de Vega. *Plasmons in doped finite carbon nanotubes*, ICFO's PhD Seminar Series, 21 Oct 2016, Castelldefels, Spain.

Organized conferences:

- IONS BCN'19, 26–29 Jun 2019, Castelldefels and Barcelona, Spain.

Teaching:

- 90h - Lab experience: *Unveiling properties of matter: microscopy, optical trapping, and diffraction*. Course *Physical Engineering Projects II* for 3rd-year students of UPC's B.Sc. in Physical Engineering.

List of Publications

- S. de Vega, J. Cox, F. Sols and F. J. García de Abajo. *Strong-field-driven dynamics and high-harmonic generation in interacting 1D systems*, submitted.
- S. de Vega and F. J. García de Abajo. *Plasmon generation through electron tunneling in twisted double-layer graphene and metal-insulator-graphene systems*, Phys. Rev. B, 99, 115438 (2019).
- S. de Vega and F. J. García de Abajo. *Plasmon generation through electron tunneling in graphene*, ACS Photon., 4, 2367–2375 (2017).
- S. de Vega, J. D. Cox and F. J. García de Abajo. *Plasmons in doped finite carbon nanotubes and their interactions with fast electrons and quantum emitters*, Phys. Rev. B, 94, 075447 (2016).

Bibliography

[1] G. E. Moore, "Cramming more components onto integrated circuits," *Electronics*, vol. 38, pp. 1–4, 1965. For updated data: https://ourworldindata.org/.

[2] W. Lu, Y. Lee, J. Murdzek, J. Gertsch, A. Vardi, L. Kong, S. M. George, and J. A. del Álamo, "First transistor demonstration of thermal atomic layer etching: InGaAs FinFETs with sub-5 nm fin-width featuring in situ ALE-ALD," *2018 IEEE International Electron Devices Meeting (IEDM)*, pp. 39.1.1–39.1.4, 2018.

[3] "Samsung successfully completes 5 nm EUV development to allow greater area scaling and ultra-low power benefits," 16 Apr 2019. https://bit.ly/2PaCS17.

[4] "TSMC and OIP ecosystem partners deliver industry's first complete design infrastructure for 5 nm process technology," 3 Apr 2019. https://bit.ly/2lTjefx.

[5] R. P. Feynman, "There's plenty of room at the bottom," *Eng. Sci.*, vol. 23, pp. 22–36, 1960. http://calteches.library.caltech.edu/1976/1/1960Bottom.pdf.

[6] N. Taniguchi, "On the basic concept of 'Nano-Technology'," *Proc. Intl. Conf. Prod. Eng. Tokyo, Part II, Japan Society of Precision Engineering*, 1974.

[7] G. Binnig and H. Rohrer, "Scanning tunneling microscopy," *IBM Journal of Research and Development*, vol. 30, pp. 355–369, 1981.

[8] H. W. Kroto, J. R. Heath, S. C. O'Brien, R. F. Curl, and R. E. Smalley, "C_{60}: Buckminsterfullerene," *Nature*, vol. 318, pp. 162–163, 1985.

[9] R. G. Gould, "The LASER, Light Amplification by Stimulated Emission of Radiation," in *The Ann Arbor conference on optical pumping : the University of Michigan, 15 June through 18 June 1959* (P. A. Franken and R. H. Sands, eds.), Academic Press, 1959.

[10] A. L. Schawlow and C. H. Townes, "Infrared and optical masers," *Phys. Rev.*, vol. 112, pp. 1940–1949, 1959.

[11] T. H. Maiman, "Stimulated optical radiation in ruby," *Nature*, vol. 187, pp. 493–494, 1960.

[12] A. Javan, W. R. B. Jr., and D. R. Herriott, "Population inversion and continuous optical maser oscillation in a gas discharge containing a He-Ne mixture," *Phys. Rev. Lett.*, vol. 6, pp. 106–110, 1961.

[13] R. N. Hall, G. E. Fenner, J. D. Kingsley, T. J. Soltys, and R. O. Carlson, "Coherent light emission from GaAs junctions," *Phys. Rev. Lett.*, vol. 9, pp. 366–368, 1962.

[14] H. H. Hopkins and N. S. Kapany, "A flexible fibrescope, using static scanning," *Nature*, vol. 173, pp. 39–41, 1954.

[15] J. Bardeen and W. H. Brattain, "The transistor, a semi-conductor triode," *Phys. Rev.*, vol. 74, pp. 230–231, 1948.

[16] W. Shockley, "Circuit element utilizing semiconductive material," Filed June 26, 1948, issued September 25, 1951. US Patent 2,569,347.

[17] K. Dawon, "Circuit element utilizing semiconductive material," Filed May 31, 1960, issued August 27, 1963. US Patent 3,102,230.

[18] M. M. Atalla, E. Tannenbaum, and E. J. Scheibner, "Stabilization of silicon surfaces by thermally grown oxides," *The Bell System Technical Journal*, vol. 38, pp. 749–783, 1959.

[19] B. E. A. Saleh and M. C. Teich, *Fundamentals of Photonics*. Wiley Series in Pure and Applied Optics, 2009.

[20] A. Trügler, *Optical Properties of Metallic Nanoparticles*. Switzerland: Springer Series in Materials Science, 2016.

[21] H. A. Atwater, "The promise of plasmonics," *Scientific American*, vol. 296, pp. 56–63, 2007.

[22] A. I. Fernández-Domínguez, F. J. García-Vidal, and L. Martín-Moreno, "Unrelenting plasmons," *Nat. Photon.*, vol. 11, pp. 8–10, 2017.

[23] M. I. Stockman, K. Kneipp, S. I. Bozhevolnyi, and et al., "Roadmap on plasmonics," *J. Opt.*, vol. 20, p. 043001, 2018.

[24] N. W. Ashcroft and N. D. Mermin, *Solid State Physics*. Philadelphia: Harcourt College Publishers, 1976.

[25] M. P. Marder, *Condensed Matter Physics*. New Jersey: Wiley, 2010.

[26] F. Bloch, “Heisenberg and the early days of quantum mechanics,” *Phys. Today*, vol. 29, pp. 23–27, 1976.

[27] M. Scheffler, A. Tkatchenko, and P. Rinke, *Theoretical Material Science*. 2012.

[28] J. D. Jackson, *Classical Electrodynamics*. New York: Wiley, 1975.

[29] L. Novotny and B. Hecht, *Principles of Nano-Optics*. New York: Cambridge University Press, 2012.

[30] M. Born and E. Wolf, *Principles of Optics: Electromagnetic Theory of Propagation, Interference and Diffraction of Light*. Cambridge: Cambridge University Press, 1999.

[31] S. A. Maier, *Plasmonics: Fundamentals and Applications*. New York: Springer, 2007.

[32] E. D. Palik, *Handbook of Optical Constants of Solids*. San Diego: Academic Press, 1985.

[33] H. Yan, T. Low, W. Zhu, and et al., “Damping pathways of mid-infrared plasmons in graphene nanostructures,” *Nat. Photon.*, vol. 7, pp. 394–399, 2013.

[34] L. Ju, B. Geng, J. Horng, and et al., “Graphene plasmonics for tunable terahertz metamaterials,” *Nat. Nanotech.*, vol. 6, pp. 630–634, 2011.

[35] J. Chen, M. Badioli, P. Alonso-González, and et al., “Optical nano-imaging of gate-tunable graphene plasmons,” *Nature*, vol. 487, pp. 77–81, 2012.

[36] Z. Fei, A. S. Rodin, G. O. Andreev, and et al., “Gate-tuning of graphene plasmons revealed by infrared nano-imaging,” *Nature*, vol. 487, pp. 82–85, 2012.

[37] S. Gong, M. Hu, R. Zhong, and et al., "Electron beam excitation of surface plasmon polaritons," *Opt. Express*, vol. 22, pp. 19252–19261, 2014.

[38] F. J. García de Abajo, "Multiple excitation of confined graphene plasmons by single free electrons," *ACS Nano*, vol. 7, pp. 11409–11419, 2013.

[39] F. H. L. Koppens, D. E. Chang, and F. J. García de Abajo, "Graphene plasmonics: A platform for strong light-matter interactions," *Nano Lett.*, vol. 11, pp. 3370–3377, 2011.

[40] A. Y. Nikitin, F. Guinea, F. J. García-Vidal, and L. Martín-Moreno, "Fields radiated by a nanoemitter in a graphene sheet," *Phys. Rev. B*, vol. 84, p. 195446, 2011.

[41] S. de Vega and F. J. García de Abajo, "Plasmon generation through electron tunneling in graphene," *ACS Photon.*, vol. 4, pp. 2367–2375, 2017.

[42] S. de Vega and F. J. García de Abajo, "Plasmon generation through electron tunneling in twisted double-layer graphene and metal-insulator-graphene systems," *Phys. Rev. B*, vol. 99, p. 115438, 2019.

[43] P. Bharadwaj, A. Bouhelier, and L. Novotny, "Electrical excitation of surface plasmons," *Phys. Rev. Lett.*, vol. 106, p. 226802, 2011.

[44] C. F. Bohren and D. R. Huffman, *Absorption and Scattering of Light by Small Particles*. Canada: John Wiley and Sons, Inc., 1998.

[45] L. Hedin and S. Lundqvist, "Effects of electron-electron and electron-phonon interactions on the one-electron states of solids," in *Solid state physics* (D. T. F. Seitz and H. Ehrenreich, eds.), vol. 23 of *Solid State Physics*, pp. 1–181, Academic Press, 1970.

[46] R. W. Boyd, *Nonlinear Optics*. Amsterdam: Academic Press, 3 ed., 2008.

[47] A. Messiah, *Quantum Mechanics*. New York: North-Holland, 1966.

[48] J. D. Cox and F. J. García de Abajo, "Electrically tunable nonlinear plasmonics in graphene nanoislands," *Nat. Commun.*, vol. 5, p. 5725, 2014.

[49] F. J. García de Abajo, "Optical excitations in electron microscopy," *Rev. Mod. Phys.*, vol. 82, pp. 209–275, 2010.

[50] D. Pines and P. Nozières, *The Theory of Quantum Liquids*. New York: W. A. Benjamin, Inc., 1966.

[51] A. K. Geim and K. S. Novoselov, "The rise of graphene," *Nat. Mater.*, vol. 6, pp. 183–191, 2007.

[52] A. C. Ferrari, F. Bonaccorso, V. Fal'ko, and et al., "Science and technology roadmap for graphene, related two-dimensional crystals, and hybrid systems," *Nanoscale*, vol. 7, p. 4598, 2015.

[53] P. A. D. Gonçalves and N. M. R. Peres, *An introduction to graphene plasmonics*. Singapore: World Scientific, 2016.

[54] T. Christensen, *From Classical to Quantum Plasmonics in Three and Two Dimensions*. Switzerland: Springer Theses, 2017.

[55] F. J. García de Abajo, "Graphene plasmonics: Challenges and opportunities," *ACS Photon.*, vol. 1, pp. 135–152, 2014.

[56] K. S. Novoselov, A. K. Geim, S. V. Morozov, and et al., "Electric field effect in atomically thin carbon films," *Science*, vol. 306, pp. 666–669, 2004.

[57] K. S. Novoselov, A. K. Geim, S. V. Morozov, and et al., "Two-dimensional gas of massless Dirac fermions in graphene," *Nature*, vol. 438, pp. 197–200, 2005.

[58] A. H. Castro Neto, F. Guinea, N. M. R. Peres, K. S. Novoselov, and A. K. Geim, "The electronic properties of graphene," *Rev. Mod. Phys.*, vol. 81, pp. 109–162, 2009.

[59] P. R. Wallace, "The band theory of graphite," *Phys. Rev.*, vol. 71, pp. 622–634, 1947.

[60] N. M. R. Peres, F. Guinea, and A. H. C. Neto, "Electronic properties of disordered two-dimensional carbon," *Phys. Rev. B*, vol. 73, p. 125411, 2006.

[61] E. H. Hwang and S. Das Sarma, "Dielectric function, screening, and plasmons in two-dimensional graphene," *Phys. Rev. B*, vol. 75, p. 205418, 2007.

[62] J. Crowell and R. H. Ritchie, "Radiative decay of coulomb-stimulated plasmons in spheres," *Phys. Rev.*, vol. 172, pp. 436–440, 1968.

[63] W. L. Barnes, A. Dereux, and T. W. Ebbesen, "Surface plasmon subwavelength optics," *Nature*, vol. 424, pp. 824–830, 2003.

[64] B. Diaconescu, K. Pohl, L. Vattuone, and et al., "Low-energy acoustic plasmons at metal surfaces," *Nature*, vol. 448, pp. 57–59, 2007.

[65] M. Jablan, H. Buljan, and M. Soljačić, "Plasmonics in graphene at infrared frequencies," *Phys. Rev. B*, vol. 80, p. 245435, 2009.

[66] A. N. Grigorenko, M. Polini, and K. S. Novoselov, "Graphene plasmonics," *Nat. Photon.*, vol. 6, pp. 749–758, 2012.

[67] C. R. Dean, A. F. Young, I. Meric, and et al., "Boron nitride substrates for high-quality graphene electronics," *Nat. Nanotech.*, vol. 5, pp. 722–726, 2010.

[68] A. Principi, M. Carrega, M. B. Lundeberg, and et al., "Plasmon losses due to electron-phonon scattering: The case of graphene encapsulated in hexagonal boron nitride," *Phys. Rev. B*, vol. 90, p. 165408, 2014.

[69] A. Manjavacas, F. Marchesin, S. Thongrattanasiri, and et al., "Tunable molecular plasmons in polycyclic aromatic hydrocarbons," *ACS Nano*, vol. 7, pp. 3635–3643, 2013.

[70] A. Lauchner, A. Schlather, A. Manjavacas, and et al., "Molecular plasmonics," *Nano Lett.*, vol. 15, pp. 6208–6214, 2015.

[71] S. Enoch, R. Quidant, and G. Badenes, "Optical sensing based on plasmon coupling in nanoparticle arrays," *Opt. Express*, vol. 12, pp. 3422–3427, 2004.

[72] S. A. Maier, M. D. Friedman, P. E. Barclay, and O. Painter, "Experimental demonstration of fiber-accessible metal nanoparticle plasmon waveguides for planar energy guiding and sensing," *Appl. Phys. Lett.*, vol. 86, p. 071103, 2005.

[73] J. N. Anker, W. P. Hall, O. Lyandres, and et al., "Biosensing with plasmonic nanosensors," *Nat. Mater.*, vol. 7, pp. 442–453, 2008.

[74] A. Marini, I. Silveiro, and F. J. García de Abajo, "Molecular sensing with tunable graphene plasmons," *ACS Photon.*, vol. 2, pp. 876–882, 2015.

[75] F. D. Angelis, M. Patrini, G. Das, and et al., "A hybrid plasmonic-photonic nanodevice for label-free detection of a few molecules," *Nano Lett.*, vol. 8, pp. 2321–2327, 2008.

[76] F. Neubrech, A. Pucci, T. W. Cornelius, and et al., "Resonant plasmonic and vibrational coupling in a tailored nanoantenna for infrared detection," *Phys. Rev. Lett.*, vol. 101, p. 157403, 2008.

[77] Y. Liu, R. Cheng, L. Liao, and et al., "Plasmon resonance enhanced multicolour photodetection by graphene," *Nat. Commun.*, vol. 2, p. 579, 2011.

[78] H. Chalabi, D. Schoen, and M. L. Brongersma, "Hot-electron photodetection with a plasmonic nanostripe antenna," *Nano Lett.*, vol. 14, pp. 1374–1380, 2014.

[79] G. W. Hanson, "Dyadic green's functions and guided surface waves for a surface conductivity model of graphene," *J. Appl. Phys.*, vol. 103, p. 064302, 2009.

[80] A. Manjavacas and F. J. García de Abajo, "Robust plasmon waveguides in strongly interacting nanowire arrays," *Nano Lett.*, vol. 9, pp. 1285–1289, 2009.

[81] H. A. Atwater and A. Polman, "Plasmonics for improved photovoltaic devices," *Nat. Mater.*, vol. 9, pp. 205–213, 2010.

[82] X. Qian, X.-H. Peng, D. O. Ansari, and et al., "In vivo tumor targeting and spectroscopic detection with surface-enhanced Raman nanoparticle tags," *Nat. Biotech.*, vol. 26, pp. 83–90, 2008.

[83] D. E. Chang, A. S. Sørensen, P. R. Hemmer, and M. D. Lukin, "Quantum optics with surface plasmons," *Phys. Rev. Lett.*, vol. 97, p. 053002, 2006.

[84] D. E. Chang, A. S. Sørensen, P. R. Hemmer, and M. D. Lukin, "Strong coupling of single emitters to surface plasmons," *Phys. Rev. B*, vol. 76, p. 035420, 2007.

[85] D. Dzsotjan, A. S. Sørensen, and M. Fleischhauer, "Quantum emitters coupled to surface plasmons of a nanowire: A Green's function approach," *Phys. Rev. B*, vol. 82, p. 075427, 2010.

[86] A. Gonzalez-Tudela, D. Martin-Cano, E. Moreno, and et al., "Entanglement of two qubits mediated by one-dimensional plasmonic waveguides," *Phys. Rev. Lett.*, vol. 106, p. 020501, 2011.

[87] P. A. Huidobro, A. Y. Nikitin, C. González-Ballestero, and et al., "Superradiance mediated by graphene surface plasmons," *Phys. Rev. B*, vol. 85, p. 155438, 2012.

[88] I. Soto Lamata, P. Alonso-González, R. Hillenbrand, and A. Y. Nikitin, "Plasmons in cylindrical 2D materials as a platform for nanophotonic circuits," *ACS Photon.*, vol. 90, p. 125417, 2015.

[89] I. V. Bondarev, G. Y. Slepyan, and S. A. Maksimenko, "Spontaneous decay of excited atomic states near a carbon nanotube," *Phys. Rev. Lett.*, vol. 89, p. 115504, 2002.

[90] I. V. Bondarev and B. Vlahovic, "Optical absorption by atomically doped carbon nanotubes," *Phys. Rev. B*, vol. 75, p. 073401, 2006.

[91] I. V. Bondarev and B. Vlahovic, "Entanglement of a pair of atomic qubits near a carbon nanotube," *Phys. Rev. B*, vol. 75, p. 033402, 2007.

[92] I. V. Bondarev, "Surface electromagnetic phenomena in pristine and atomically doped carbon nanotubes," *J. Comput. Theor. Nanosci.*, vol. 7, pp. 1673–1687, 2010.

[93] L. Martín-Moreno, F. J. García de Abajo, and F. J. García-Vidal, "Ultraefficient coupling of a quantum emitter to the tunable guided plasmons of a carbon nanotube," *Phys. Rev. Lett.*, vol. 115, p. 173601, 2015.

[94] P. Avouris, M. Freitag, and V. Perebeinos, "Carbon-nanotube photonics and optoelectronics," *Nat. Phot.*, vol. 2, p. 341, 2008.

[95] Z. Shi, X. Hong, H. A. Bechtel, and et al., "Observation of a Luttinger-liquid plasmon in metallic single-walled carbon nanotubes," *Nat. Photon.*, vol. 9, pp. 515–519, 2015.

[96] T. Morimoto, S.-K. Joung, T. Saito, and et al., "Length-dependent plasmon resonance in single-walled carbon nanotubes," *ACS Nano*, vol. 8, pp. 9897–9904, 2014.

[97] F. J. García de Abajo and A. Howie, "Retarded field calculation of electron energy loss in inhomogeneous dielectrics," *Phys. Rev. B*, vol. 65, p. 115418, 2002.

[98] S. Thongrattanasiri, A. Manjavacas, and F. J. García de Abajo, "Quantum finite-size effects in graphene plasmons," *ACS Nano*, vol. 6, pp. 1766–1775, 2012.

[99] J. J. Sakurai, *Modern Quantum Mechanics*. Addison-Wesley, 1994.

[100] Z. Ficek and R. Tanas, "Entangled states and collective nonclassical effects in two-atom systems," *Phys. Rep.*, vol. 372, pp. 369–443, 2002.

[101] A. Manjavacas, S. Thongrattanasiri, D. E. Chang, and F. J. García de Abajo, "Temporal quantum control with graphene," *New J. Phys.*, vol. 14, p. 123020, 2012.

[102] E. T. Jaynes and F. W. Cummings, "Comparison of quantum and semiclassical radiation theories with application to the beam maser," *Proc. IEEE*, vol. 51, pp. 89–109, 1963.

[103] P. Meystre and M. Sargent, *Elements of Quantum Optics*. Berlin: Springer-Verlag, 2007.

[104] L. M. Duan and C. Monroe, "Robust probabilistic quantum information processing with atoms, photons, and atomic ensembles," vol. 55 of *Ad-*

vances In Atomic, Molecular, and Optical Physics, pp. 419–463, Academic Press, 2008.

[105] T. Brabec and F. Krausz, "Intense few-cycle laser fields: Frontiers of nonlinear optics," *Rev. Mod. Phys.*, vol. 72, pp. 545–591, 2000.

[106] P. B. Corkum and F. Krausz, "Attosecond science," *Nat. Phys.*, vol. 3, pp. 381–387, 2007.

[107] N. H. Burnett, H. A. Baldis, M. C. Richardson, and G. D. Enright, "Harmonic generation in CO_2 laser target interaction," *Appl. Phys. Lett.*, vol. 31, p. 172, 1977.

[108] A. McPherson, G. Gibson, H. Jara, U. Johann, T. S. Luk, I. A. McIntyre, K. Boyer, and C. K. Rhodes, "Studies of multiphoton production of vacuum-ultraviolet radiation in the rare gases," *J. Opt. Soc. Am. B*, vol. 4, pp. 595–601, 1987.

[109] M. Ferray, A. L'Huillier, X. F. Li, L. A. Lompre, G. Mainfray, and C. Manus, "Multiple harmonic conversion of 1064 nm radiation in rare gasses," *J. Phys. B*, vol. 419, pp. 803–807, 1988.

[110] M. Lewenstein, P. Balcou, M. Y. Ivanov, A. L'Huillier, and P. B. Corkum, "Theory of high-harmonic generation by low-frequency laser fields," *Phys. Rev. A*, vol. 49, pp. 2117–2132, 1994.

[111] I. McKinnie and H. Kapteyn, "Ultrafast lasers yield X-rays," *Nat. Photon.*, vol. 4, pp. 149–151, 2010.

[112] M. Hohenleutner, F. Langer, O. Schubert, M. Knorr, U. Huttner, S. W. Koch, M. Kira, and R. Huber, "Theoretical analysis of high-harmonic generation in solids," *Nature*, vol. 523, pp. 572–575, 2015.

[113] G. Vampa, T. J. Hammond, N. Thiré, B. E. Schmidt, F. Légaré, C. R. McDonald, T. Brabec, and P. B. Corkum, "Linking high harmonics from gases and solids," *Nature*, vol. 522, pp. 462–464, 2015.

[114] C.-M. Wang, T.-S. Ho, and S.-I. Chu, "Determination of band structure from the intra-band power spectrum of high harmonic generation in crystal," *J. Phys. B*, vol. 49, p. 225401, 2016.

[115] B. Zaks, R. B. Liu, and M. S. Sherwin, "Experimental observation of electron-hole recollisions," *Nature*, vol. 483, pp. 580–583, 2012.

[116] B. Wolter, M. G. Pullen, A.-T. Le, M. Baudisch, K. Doblhoff-Dier, A. Senftleben, M. Hemmer, C. D. Schröter, J. Ullrich, T. Pfeifer, R. Moshammer, S. Gräfe, O. Vendrell, C. D. Lin, and J. Biegert, "Ultrafast electron diffraction imaging of bond breaking in di-ionized acetylene," *Science*, vol. 354, pp. 308–312, 2016.

[117] A. H. Zewail, "Femtochemistry: Atomic-scale dynamics of the chemical bond," *JPCA*, vol. 104, pp. 5660–5694, 2000.

[118] L. Feng, J. Hu, L. W. Clark, and C. Chin, "Correlations in high-harmonic generation of matter-wave jets revealed by pattern recognition," *Science*, vol. 363, pp. 521–524, 2019.

[119] S. Ghimire, A. D. DiChiara, E. Sistrunk, P. Agostini, L. F. DiMauro, and D. A. Reis, "Observation of high-order harmonic generation in a bulk crystal," *Nat. Phys.*, vol. 7, pp. 138–141, 2011.

[120] O. Schubert, M. Hohenleutner, F. Langer, B. Urbanek, C. Lange, U. Huttner, D. Golde, T. Meier, M. Kira, S. W. Koch, and R. Huber, "Sub-cycle control of terahertz high-harmonic generation by dynamical bloch oscillations," *Nat. Photon.*, vol. 8, pp. 119–123, 2014.

[121] T. T. Luu, M. Garg, S. Y. Kruchinin, A. Moulet, M. T. Hassan, and E. Goulielmakis, "Extreme ultraviolet high-harmonic spectroscopy of solids," *Nature*, vol. 521, pp. 498–502, 2015.

[122] P. B. Corkum, "Plasma perspective on strong-field multiphoton ionization," *Phys. Rev. Lett.*, vol. 71, pp. 1994–1997, 1993.

[123] U. Huttner, M. Kira, and S. W. Koch, "Ultrahigh off-resonant field effects in semiconductors," *Laser Photon. Rev.*, vol. 11, p. 1700049, 2017.

[124] S. Ghimire and D. Reis, "High-harmonic generation from solids," *Nat. Phys.*, vol. 15, pp. 10–16, 2019.

[125] E. N. Osika, A. Chacón, L. Ortmann, N. Suárez, J. A. Pérez-Hernández, B. Szafran, M. F. Ciappina, F. Sols, A. S. Landsman, and M. Lewenstein, "Wannier-Bloch approach to localization in high-harmonics generation in solids," *Phys. Rev. X*, vol. 7, p. 021017, 2017.

[126] A. F. Kemper, B. Moritz, J. K. Freericks, and T. P. Devereaux, "Theoretical description of high-order harmonic generation in solids," *New J. Phys.*, vol. 15, p. 023003, 2013.

[127] G. Vampa, C. R. McDonald, G. Orlando, D. D. Klug, P. B. Corkum, and T. Brabec, "Theoretical analysis of high-harmonic generation in solids," *Phys. Rev. Lett.*, vol. 113, p. 073901, 2014.

[128] T. T. Luu and H. J. Wörner, "High-order harmonic generation in solids: A unifying approach," *Phys. Rev. B*, vol. 94, p. 115164, 2016.

[129] C. R. McDonald, G. Vampa, G. Orlando, P. B. Corkum, and T. Brabec, "Theory of high-harmonic generation in solids," *J. Phys. Conf. Ser.*, vol. 594, p. 012021, 2015.

[130] W. P. Su, J. R. Schrieffer, and A. J. Heeger, "Solitons in polyacetylene," *Phys. Rev. Lett.*, vol. 42, pp. 1689–1701, 1979.

[131] H. W. Streitwolf, "Physical properties of polyacetylene," *Phys. Stat. Sol. (b)*, vol. 127, pp. 11–54, 1985.

[132] F. Gebhard, K. Bott, M. Scheidler, P. Thomas, and S. W. Koch, "Optical absorption of non-interacting tightbinding electrons in a Peierls-distorted chain at half band-filling," *Philos. Mag. B*, vol. 75, pp. 1–12, 1997.

[133] D. Bauer and K. K. Hansen, "High-harmonic generation in solids with and without topological edge states," *Phys. Rev. Lett.*, vol. 120, p. 177401, 2018.

[134] C. Jürss and D. Bauer, "High-harmonic generation in su-schrieffer-heeger chains," *Phys. Rev. B*, vol. 99, p. 195428, 2019.

[135] H. Drüeke and D. Bauer, "Robustness of topologically sensitive harmonic generation in laser-driven linear chains," *Phys. Rev. A*, vol. 99, p. 053402, 2019.

[136] K. K. Hansen, D. Bauer, and L. B. Madsen, "Finite-system effects on high-order harmonic generation: From atoms to solids," *Phys. Rev. A*, vol. 97, p. 043424, 2018.

[137] D. Pines and D. Bohm, "A collective description of electron interactions: II. Collective vs individual particle aspects of the interactions," *Phys. Rev.*, vol. 85, pp. 338–353, 1952.

[138] J. C. Baggesen and L. B. Madsen, "On the dipole, velocity and acceleration forms in high-order harmonic generation from a single atom or molecule," *J. Phys. B*, vol. 44, p. 115601, 2011.

[139] J. K. Asbóth, L. Oroszlány, and A. Pályi, *A Short Course on Topological Insulators: Band Structure and Edge States in One and Two Dimensions*. Switzerland: Springer, 2016.

[140] M. Kauranen and A. V. Zayats, "Nonlinear plasmonics," *Nat. Photon.*, vol. 6, pp. 737–748, 2012.

[141] J. D. Cox, A. Marini, and F. J. García de Abajo, "Plasmon-assisted high-harmonic generation in graphene," *Nat. Commun.*, vol. 8, p. 14380, 2017.

[142] K. A. Pronin, A. D. Bandrauk, and A. A. Ovchinnikov, "Harmonic generation by a one-dimensional conductor: Exact results," *Phys. Rev. B*, vol. 50, pp. 3473–3476, 1994.

[143] M. Baudisch, A. Marini, J. D. Cox, T. Zhu, F. Silva, S. Teichmann, M. Massicotte, F. Koppens, L. S. Levitov, F. J. García de Abajo, and J. Biegert, "Ultrafast nonlinear optical response of Dirac fermions in graphene," *Nat. Commun.*, vol. 9, p. 1018, 2018.

[144] M. F. L. D. Volder, S. H. Tawfick, R. H. Baughman, and A. J. Hart, "Carbon nanotubes: Present and future commercial applications," *Science*, vol. 339, pp. 535–539, 2015.

[145] G. Hills, C. Lau, A. Wright, S. Fuller, M. D. Bishop, P. K. Tathagata Srimani, R. Ho, A. Amer, Y. Stein, D. Murphy, Arvind, A. Chandrakasan, and M. M. Shulaker, "Modern microprocessor built from complementary carbon nanotube transistors," *Nature*, vol. 572, pp. 595–602, 2019.

[146] P.-H. Ho, D. B. Farmer, G. S. Tulevski, S.-J. Han, D. M. Bishop, L. M. Gignac, J. Bucchignano, and A. L. F. P. Avouris, "Intrinsically ultrastrong plasmon-exciton interactions in crystallized films of carbon nanotubes," *Proc. Natl. Academ. Sci.*, vol. 115, pp. 12662–12667, 2018.

[147] A. L. Falk, K.-C. Chiu, D. B. Farmer, Q. Cao, J. Tersoff, Y.-H. Lee, P. Avouris, and S.-J. Han, "Coherent plasmon and phonon-plasmon resonances in carbon nanotubes," *Phys. Rev. Lett.*, vol. 118, p. 257401, 2017.

[148] Z. Fei, G. O. Andreev, W. Bao, L. M. Zhang, A. S. McLeod, C. Wang, M. K. Stewart, Z. Zhao, G. Dominguez, M. Thiemens, M. M. Fogler, M. J. Tauber, A. H. Castro-Neto, C. N. Lau, F. Keilmann, and D. N. Basov, "Infrared nanoscopy of Dirac plasmons at the graphene–SiO_2 interface," *Nano Lett.*, vol. 11, pp. 4701–4705, 2011.

[149] D. Sánchez-Portal, E. Artacho, J. M. Soler, A. Rubio, and P. Ordejón, "*Ab initio* structural, elastic, and vibrational properties of carbon nanotubes," *Phys. Rev. B*, vol. 59, pp. 12678–12688, 1999.

[150] M. Machón, S. Reich, C. Thomsen, D. Sánchez-Portal, and P. Ordejón, "*Ab initio* calculations of the optical properties of 4-Å-diameter single-walled nanotubes," *Phys. Rev. B*, vol. 66, p. 155410, 2000.

[151] R. Demichelis, Y. Noël, P. D'Arco, M. Rérat, C. M. Zicovich-Wilson, and R. Dovesi, "Properties of carbon nanotubes: An *ab Initio* study using large gaussian basis sets and various DFT functionals," *J. Phys. Chem. C*, vol. 115, pp. 8876–8885, 2011.

[152] S. de Vega, J. D. Cox, , and F. J. García de Abajo, "Plasmons in doped finite carbon nanotubes and their interactions with fast electrons and quantum emitters," *Phys. Rev. B*, vol. 94, p. 075447, 2016.

[153] M. Bockrath, D. H. Cobden, J. Lu, A. G. Rinzler, R. E. Smalley, L. Balents, and P. L. McEuen, "Luttinger-liquid behaviour in carbon nanotubes," *Nature*, vol. 397, pp. 598–601, 1999.

[154] H. Ishii, H. Kataura, H. Shiozawa, H. Yoshioka, H. Otsubo, Y. Takayama, T. Miyahara, S. Suzuki, Y. Achiba, M. Nakatake, T. Narimura, M. Hi-

gashiguchi, K. Shimada, H. Namatame, and M. Taniguchi, "Direct observation of Tomonaga–Luttinger-liquid state in carbon nanotubes at low temperatures," *Nature*, vol. 426, pp. 540–544, 2003.

[155] T. W. Odom, J.-L. Huang, P. Kim, and C. M. Lieber, "Structure and electronic properties of carbon nanotubes," *J. Phys. Chem. C*, vol. 104, pp. 2794–2809, 2000.

[156] R. Okuyama, W. Izumida, and M. Eto, "Topological classification of the single-wall carbon nanotube," *Phys. Rev. B*, vol. 99, p. 115409, 2019.

[157] E. A. Laird, F. Kuemmeth, G. A. Steele, K. Grove-Rasmussen, J. Nygård, K. Flensberg, and L. P. Kouwenhoven, "Quantum transport in carbon nanotubes," *Rev. Mod. Phys.*, vol. 87, p. 703, 2015.

[158] A. C. Torres-Diasab, T. F. T. Cerqueira, W. Cui, M. A. L. Marques, S. Botti, D. Machona, M. A. Hartmann, Y. Sun, D. J. Dunstan, and A. San-Miguel, "From mesoscale to nanoscale mechanics in single-wall carbon nanotubes," *Carbon*, vol. 123, pp. 145–150, 2017.

[159] T. Hayashi, Y. A. Kim, T. Matoba, M. Esaka, K. Nishimura, T. T. M. Endo, and M. S. Dresselhaus, "Smallest freestanding single-walled carbon nanotube," *Nano Lett.*, vol. 3, pp. 887–889, 2003.

[160] L. Guan, K. Suenaga, and S. Iijima, "Smallest carbon nanotube assigned with atomic resolution accuracy," *Nano Lett.*, vol. 8, pp. 459–462, 2008.

[161] K. R. Li, M. I. Stockman, and D. J. Bergman, "Self-similar chain of metal nanospheres as an efficient nanolens," *Phys. Rev. Lett.*, vol. 91, p. 227402, 2003.

[162] R. A. Álvarez-Puebla, L. M. Liz-Marzán, and F. J. García de Abajo, "Light concentration at the nanometer scale," *J. Phys. Chem. Lett.*, vol. 1, pp. 2428–2434, 2010.

[163] B. Liedberg, C. Nylander, and I. Lunström, "Surface plasmon resonance for gas detection and biosensing," *Sens. Actuators*, vol. 4, pp. 299–304, 1983.

[164] S. Zeng, D. Baillargeat, H.-P. Hod, and K.-T. Yong, "Nanomaterials enhanced surface plasmon resonance for biological and chemical sensing applications," *Chem. Soc. Rev.*, vol. 43, pp. 3426–3452, 2014.

[165] J. Reguera, D. Jimenez de Aberasturi, J. Langer, and L. M. Liz-Marzán, "Anisotropic metal nanoparticles for surface enhanced raman scattering," *Chem. Soc. Rev.*, vol. 46, pp. 3866–3885, 2017.

[166] D. P. O'Neal, L. R. Hirsch, N. J. Halas, J. D. Payne, and J. L. West, "Photothermal tumor ablation in mice using near infrared-absorbing nanoparticles," *Cancer Lett.*, vol. 209, pp. 171–176, 2004.

[167] P. K. Jain, I. H. El-Sayed, and M. A. El-Sayed, "Au nanoparticles target cancer," *Nano Today*, vol. 2, pp. 18–29, 2007.

[168] Y. L. Luo, Y. S. Shiao, and Y. F. Huang, "Release of photoactivatable drugs from plasmonic nanoparticles for targeted cancer therapy," *ACS Nano*, vol. 5, pp. 7796–7804, 2011.

[169] S. Palomba and L. Novotny, "Nonlinear excitation of surface plasmon polaritons by four-wave mixing," *Phys. Rev. Lett.*, vol. 101, p. 056802, 2008.

[170] S. Palomba, M. Danckwerts, and L. Novotny, "Nonlinear plasmonics with gold nanoparticle antennas," *J. Opt. A: Pure Appl. Opt.*, vol. 11, p. 114030, 2009.

[171] J. Shen, Y. Zhu, X. Yang, and C. Li, "Graphene quantum dots: Emergent nanolights for bioimaging, sensors, catalysis and photovoltaic devices," *Chem. Commun.*, vol. 48, pp. 3686–3699, 2012.

[172] C. Wang, O. Ranasingha, S. Natesakhawat, P. R. Ohodnicki, M. Andio, J. P. Lewis, and C. Matranga, "Visible light plasmonic heating of Au–ZnO for the catalytic reduction of CO_2," *Nanoscale*, vol. 5, pp. 6968–6974, 2013.

[173] C. Clavero, "Plasmon-induced hot-electron generation at nanoparticle/metal-oxide interfaces for photovoltaic and photocatalytic devices," *Nat. Photon.*, vol. 8, pp. 95–103, 2014.

[174] J. Y. Park, L. R. Baker, and G. A. Somorjai, "Role of hot electrons and metal–oxide interfaces in surface chemistry and catalytic reactions," *Chem. Rev.*, vol. 115, pp. 2781–2817, 2015.

[175] K. R. Catchpole and A. Polman, "Plasmonic solar cells," *Opt. Express*, vol. 16, pp. 21793–21800, 2008.

[176] Z. Fang, S. Thongrattanasiri, A. Schlather, Z. Liu, L. Ma, Y. Wang, P. M. Ajayan, P. Nordlander, N. J. Halas, and F. J. García de Abajo, "Gated tunability and hybridization of localized plasmons in nanostructured graphene," *ACS Nano*, vol. 7, pp. 2388–2395, 2013.

[177] V. W. Brar, M. S. Jang, M. Sherrott, J. J. Lopez, and H. A. Atwater, "Highly confined tunable mid-infrared plasmonics in graphene nanoresonators," *Nano Lett.*, vol. 13, pp. 2541–2547, 2013.

[178] V. W. Brar, M. Seok Jang, M. C. Sherrott, S. Kim, J. J. Lopez, L. B. Kim, M. Choi, and H. A. Atwater, "Hybrid surface-phonon-plasmon polariton modes in graphene/monolayer h-BN heterostructures," *Nano Lett.*, vol. 14, pp. 3876–3880, 2014.

[179] H. Yan, Z. Li, X. Li, W. Zhu, P. Avouris, and F. Xia, "Infrared spectroscopy of tunable Dirac terahertz magneto-plasmons in graphene," *Nano Lett.*, vol. 12, pp. 3766–3771, 2012.

[180] N. Kumada, P. Roulleau, B. Roche, M. Hashisaka, H. Hibino, I. Petković, and D. C. Glattli, "Resonant edge magnetoplasmons and their decay in graphene," *Phys. Rev. Lett.*, vol. 103, p. 266601, 2014.

[181] G. X. Ni, L. Wang, M. D. Goldflam, M. Wagner, Z. Fei, A. S. McLeod, M. K. Liu, F. Keilmann, B. Özyilmaz, A. H. C. Neto, J. Hone, M. M. Fogler, and D. N. Basov, "Ultrafast optical switching of infrared plasmon polaritons in high-mobility graphene," *Nat. Photon.*, vol. 10, pp. 244–248, 2016.

[182] A. Woessner, M. B. Lundeberg, Y. Gao, A. Principi, P. Alonso-González, M. Carrega, K. Watanabe, T. Taniguchi, G. Vignale, M. Polini, J. Hone, R. Hillenbrand, and F. H. Koppens, "Highly confined low-loss plasmons in graphene-boron nitride heterostructures," *Nat. Mater.*, vol. 14, pp. 421–425, 2015.

[183] D. N. Basov, M. M. Fogler, and F. J. García de Abajo, "Polaritons in van der Waals materials," *Science*, vol. 354, p. aag1992, 2016.

[184] H. Yan, T. Low, W. Zhu, Y. Wu, M. Freitag, X. Li, F. Guinea, P. Avouris, and F. Xia, "Damping pathways of mid-infrared plasmons in graphene nanostructures," *Nat. Photon.*, vol. 7, pp. 394–399, 2013.

[185] M. Freitag, H.-Y. Chiu, M. Steiner, V. Perebeinos, and P. Avouris, "Thermal infrared emission from biased graphene," *Nat. Nanotech.*, vol. 5, pp. 497–501, 2010.

[186] O. Ilic, M. Jablan, J. D. Joannopoulos, I. Celanovic, H. Buljan, and M. Soljačić, "Near-field thermal radiation transfer controlled by plasmons in graphene," *Phys. Rev. B*, vol. 85, p. 155422, 2012.

[187] A. Manjavacas, S. Thongrattanasiri, J.-J. Greffet, and F. J. García de Abajo, "Graphene optical-to-thermal converter," *Appl. Phys. Lett.*, vol. 105, p. 211102, 2014.

[188] V. W. Brar, M. C. Sherrott, M. Seok Jang, S. Kim, L. Kim, M. Choi, L. A. Sweatlock, and H. A. Atwater, "Electronic modulation of infrared radiation in graphene plasmonic resonators," *Nat. Commun.*, vol. 6, p. 7032, 2015.

[189] R. Yu and F. J. García de Abajo, "Electrical detection of single graphene plasmons," *ACS Nano*, vol. 10, pp. 8045–8053, 2016.

[190] M. B. Lundeberg, Y. Gao, A. Woessner, C. Tan, P. Alonso-González, K. Watanabe, T. Taniguchi, J. Hone, R. Hillenbrand, and F. H. L. Koppens, "Thermoelectric detection and imaging of propagating graphene plasmons," *Nat. Mater.*, vol. 16, pp. 204–207, 2017.

[191] Y. Li, H. Yan, D. B. Farmer, X. Meng, W. Zhu, R. M. Osgood, T. F. Heinz, and P. Avouris, "Graphene plasmon enhanced vibrational sensing of surface-adsorbed layers," *Nano Lett.*, vol. 14, pp. 1573–1577, 2014.

[192] D. Rodrigo, O. Limaj, D. Janner, D. Etezadi, F. J. García de Abajo, V. Pruneri, and H. Altug, "Mid-infrared plasmonic biosensing with graphene," *Science*, vol. 349, pp. 165–168, 2015.

[193] D. B. Farmer, P. Avouris, Y. Li, T. F. Heinz, and S.-J. Han, "Ultrasensitive plasmonic detection of molecules with graphene," *ACS Photon.*, vol. 3, pp. 553–557, 2016.

[194] C. F. Chen, C. H. Park, B. W. Boudouris, J. Horng, B. Geng, C. Girit, A. Zettl, M. F. Crommie, R. A. Segalman, S. G. Louie, and F. Wang, "Controlling inelastic light scattering quantum pathways in graphene," *Nature*, vol. 471, pp. 617–620, 2011.

[195] R. Ye, C. Xiang, J. Lin, Z. Peng, K. Huang, Z. Yan, N. P. Cook, E. L. Samuel, C.-C. Hwang, G. Ruan, G. Ceriotti, A.-R. O. Raji, A. A. Martí, and J. M.

Tour, “Coal as an abundant source of graphene quantum dots,” *Nat. Commun.*, vol. 4, p. 2943, 2013.

[196] K. Müllen, “Evolution of graphene molecules: Structural and functional complexity as driving forces behind nanoscience,” *ACS Nano*, vol. 8, pp. 6531–6541, 2014.

[197] Z. Wang, T. Li, K. Almdal, N. A. Mortensen, S. Xiao, and S. Ndoni, “Experimental demonstration of graphene plasmons working close to the near-infrared window,” *Opt. Lett.*, vol. 41, pp. 5345–5348, 2016.

[198] Z. Fei, G.-X. Ni, B.-Y. Jiang, M. M. Fogler, and D. N. Basov, “Nanoplasmonic phenomena at electronic boundaries in graphene,” *ACS Photon.*, p. DOI: 10.1021/acsphotonics.7b00477, 2017.

[199] D. C. Tsui, “Observations of surface plasmon excitation by tunneling electrons in GaAs-Pb tunnel junctions,” *Phys. Rev. Lett.*, vol. 22, pp. 293–295, 1969.

[200] D. C. Tsui and A. S. Barker Jr, “Surface-plasmon excitation by tunneling electrons in GaAs-Pb tunnel junctions,” *Phys. Rev.*, vol. 186, pp. 590–591, 1969.

[201] C. B. Duke, “Plasmon excitation by electron tunneling,” *Phys. Rev.*, vol. 186, pp. 588–590, 1969.

[202] C. B. Duke, M. J. Rice, and F. Steinrisser, “Tunneling measurement of electron-plasmon interaction in degenerate semiconductors,” *Phys. Rev.*, vol. 181, pp. 733–742, 1969.

[203] E. N. Economou and K. L. Ngai, “Surface-plasmon excitation by electron tunneling,” *Phys. Rev. B*, vol. 4, pp. 4105–4108, 1971.

[204] P. Johansson, R. Monreal, and P. Apell, "Theory for light emission from a scanning tunneling microscope," *Phys. Rev. Lett.*, vol. 42, pp. 9210–9213, 1990.

[205] R. Berndt, J. K. Gimzewski, and P. Johansson, "Inelastic tunneling excitation of tip-induced plasmon modes on noble-metal surfaces," *Phys. Rev. Lett.*, vol. 67, pp. 3796–3799, 1991.

[206] P. Rai, N. Hartmann, J. Berthelot, J. Arocas, G. Colas des Francs, A. Hartschuh, and A. Bouhelier, "Electrical excitation of surface plasmons by an individual carbon nanotube transistor," *Phys. Rev. Lett.*, vol. 111, p. 026804, 2013.

[207] K. J. A. Ooi, H. S. Chu, C. Y. Hsieh, D. T. H. Tan, and L. K. Ang, "Highly efficient midinfrared on-chip electrical generation of graphene plasmons by inelastic electron tunneling excitation," *Phys. Rev. Applied*, vol. 3, p. 054001, 2015.

[208] N. L. Schneider, G. Schull, and R. Berndt, "Optical probe of quantum shot-noise reduction at a single-atom contact," *Phys. Rev. Lett.*, vol. 105, p. 026601, 2010.

[209] C. Groβe, A. Kabakchiev, T. Lutz, R. Froidevaux, F. Schramm, M. Ruben, M. Etzkorn, U. Schlickum, K. Kuhnke, , and K. Kern, "Dynamic control of plasmon generation by an individual quantum system," *Nano Lett.*, vol. 14, pp. 5693–5697, 2014.

[210] J. Kern, R. Kullock, J. Prangsma, M. Emmerling, M. Kamp, and B. Hecht, "Electrically driven optical antennas," *Nat. Photon.*, vol. 9, pp. 582–587, 2015.

[211] A. V. Uskov, J. B. Khurgin, M. Buret, A. Bouhelier, I. V. Smetanin, and I. E. Protsenko, "Biased nanoscale contact as active element for elec-

trically driven plasmonic nanoantenna," *ACS Photon.*, vol. 4, pp. 1501–1505, 2017.

[212] D. M. Koller, A. Hohenau, H. Ditlbacher, N. Galler, F. Reil, F. R. Aussenegg, A. Leitner, E. J. W. List, and J. R. Krenn, "Organic plasmon-emitting diode," *Nat. Photon.*, vol. 2, pp. 684–687, 2008.

[213] R. J. Walters, R. V. A. van Loon, I. Brunets, J. Schmitz, and A. Polman, "A silicon-based electrical source of surface plasmon polaritons," *Nat. Mater.*, vol. 9, pp. 21–25, 2010.

[214] V. Enaldiev, A. Bylinkin, and D. Svintsov, "Plasmon-assisted resonant tunneling in graphene-based heterostructures," *Phys. Rev. B*, vol. 96, p. 125437, 2017.

[215] D. Svintsov, Z. Devizorova, T. Otsuji, and V. Ryzhii, "Plasmons in tunnel-coupled graphene layers: Backward waves with quantum cascade gain," *Phys. Rev. B*, vol. 94, p. 115301, 2016.

[216] D. Yadav, S. B. Tombet, T. Watanabe, S. Arnold, V. Ryzhii, and T. Otsuji, "Terahertz wave generation and detection in double-graphene layered van der Waals heterostructures," *2D Mater.*, vol. 3, p. 045009, 2016.

[217] X. Wang, K. Braun, D. Zhang, H. Peisert, H. Adler, T. Chassé, and A. J. Meixner, "Enhancement of radiative plasmon decay by hot electron tunneling," *ACS Nano*, vol. 9, pp. 8176–8183, 2015.

[218] H. D. F. R. Aussenegg, J. R. Krenn, L. G. Jakopic, and G. Leising, "Organic diodes as monolithically integrated surface plasmon polariton detectors," *Appl. Phys. Lett.*, vol. 89, p. 161101, 2006.

[219] R. W. Heeres, S. N. Dorenbos, B. Koene, G. S. Solomon, L. P. Kouwenhoven, and V. Zwiller, "On-chip single plasmon detection," *Nano Lett.*, vol. 10, pp. 661–664, 2009.

[220] P. Neutens, P. Van Dorpe, I. De Vlaminck, L. Lagae, and G. Borghs, "Electrical detection of confined gap plasmons in metal-insulator-metal waveguides," *Nat. Photon.*, vol. 3, pp. 283–286, 2009.

[221] A. L. Falk, F. H. Koppens, L. Y. Chun, K. Kang, N. de Leon Snapp, A. V. Akimov, M.-H. Jo, M. D. Lukin, and H. Park, "Near-field electrical detection of optical plasmons and single-plasmon sources," *Nat. Phys.*, vol. 5, pp. 475–479, 2009.

[222] T. Dufaux, J. Dorfmüller, R. Vogelgesang, M. Burghard, and K. Kern, "Surface plasmon coupling to nanoscale Schottky-type electrical detectors," *Appl. Phys. Lett.*, vol. 97, p. 161110, 2010.

[223] I. Goykhman, B. Desiatov, J. Khurgin, J. Shappir, and U. Levy, "Locally oxidized silicon surface-plasmon schottky detector for telecom regime," *Nano Lett.*, vol. 11, pp. 2219–2224, 2011.

[224] M. W. Knight, H. Sobhani, P. Nordlander, and N. J. Halas, "Photodetection with active optical antennas," *Science*, vol. 332, pp. 702–704, 2011.

[225] K. M. Goodfellow, C. Chakraborty, R. Beams, L. Novotny, and A. N. Vamivakas, "Direct on-chip optical plasmon detection with an atomically thin semiconductor," *Nano Lett.*, vol. 15, pp. 5477–5481, 2015.

[226] L. Britnell, R. V. Gorbachev, A. K. Geim, L. A. Ponomarenko, A. Mishchenko, M. T. Greenaway, T. M. Fromhold, K. S. Novoselov, and L. Eaves, "Resonant tunnelling and negative differential conductance in graphene transistors," *Nat. Commun.*, vol. 4, p. 1794, 2013.

[227] H. Jeong, H. M. Oh, S. Bang, H. J. Jeong, S.-J. An, G. H. Han, H. Kim, S. J. Yun, K. K. Kim, J. C. Park, Y. H. Lee, G. Lerondel, and M. S. Jeong, "Metal-insulator-semiconductor diode consisting of two-dimensional nanomaterials," *Nano Lett.*, vol. 16, pp. 1858–1862, 2016.

[228] V. L. Katkov and V. A. Osipov, "Review article: Tunneling-based graphene electronics: Methods and examples," *J. Vac. Sci. Technol. B*, vol. 35, p. 050801, 2017.

[229] S. de Vega and F. J. García de Abajo, "Plasmon generation through electron tunneling in graphene," *ACS Photon.*, vol. 4, pp. 2367–2375, 2017.

[230] B. Wunsch, T. Stauber, F. Sols, and F. Guinea, "Dynamical polarization of graphene at finite doping," *New J. Phys.*, vol. 8, p. 318, 2006.

[231] R. Geick, C. H. Perry, and G. Rupprecht, "Normal modes in hexagonal boron nitride," *Phys. Rev.*, vol. 146, pp. 543–547, 1966.

[232] R. B. Pettit, J. Silcox, and R. Vincent, "Measurement of surface-plasmon dispersion in oxidized aluminum films," *Phys. Rev. B*, vol. 11, pp. 3116–3123, 1975.

[233] T. Ihn, J. Güttinger, F. Molitor, S. Schnez, E. Schurtenberger, A. Jacobsen, S. Hellmüller, T. Frey, S. Dröscher, C. Stampfer, and K. Ensslin, "Graphene single-electron transistors," *Mater. Today*, vol. 13, pp. 44–50, 2010.

[234] T. Low, R. Roldán, H. Wang, F. Xia, P. Avouris, L. Martín Moreno, and F. Guinea, "Plasmons and screening in monolayer and multilayer black phosphorus," *Phys. Rev. Lett.*, vol. 113, p. 106802, 2014.

[235] M. A. Huber, F. Mooshammer, M. Plankl, L. Viti, F. Sandner, L. Z. Kastner, T. Frank, J. Fabian, M. S. Vitiello, T. L. Cocker, and R. Huber, "Femtosecond photo-switching of interface polaritons in black phosphorus heterostructures," *Nat. Nanotech.*, vol. 12, pp. 207–212, 2017.

[236] G.-B. Liu, W.-Y. Shan, Y. Yao, W. Yao, and D. Xiao, "Three-band tight-binding model for monolayers of group-VIB transition metal dichalcogenides," *Phys. Rev. B*, vol. 88, p. 085433, 2013.

[237] Y.-J. Yu, Y. Zhao, S. Ryu, L. E. Brus, K. S. Kim, and P. Kim, "Tuning the graphene work function by electric field effect," *Nano Lett.*, vol. 9, pp. 3430–3434, 2009.

[238] E. Clementi and C. Roetti, "Roothaan-Hartree-Fock atomic wavefunctions," *At. Data Nucl. Data Tables*, vol. 14, pp. 177–478, 1974.

[239] K. Watanabe, T. Taniguchi, and H. Kanda, "Direct-bandgap properties and evidence for ultraviolet lasing of hexagonal boron nitride single crystal," *Nat. Mater.*, vol. 3, pp. 404–409, 2004.

[240] E. O. Filatova and A. S. Konashuk, "Interpretation of the changing the band gap of Al_2O_3 depending on its crystalline form: connection with different local symmetries," *J. Phys. Chem. C*, vol. 119, pp. 20755–20761, 2015.